Hydrodynamics of Breaking Waves on Offshore Wind Turbine Structures

Von der Fakultät für Bauingenieurwesen und Geodäsie
der
Gottfried Wilhelm Leibniz Universität Hannover

zur Erlangung des Grades
DOKTOR-INGENIEUR
Dr.-Ing.

genehmigte Dissertation
von
Dipl.-Ing. Arndt Hildebrandt
aus Mettmann

Hannover, 2013

Eigenständigkeitserklärung

Hiermit erkläre ich, dass ich diese Arbeit eigenständig und ohne unerlaubte Hilfe angefertigt habe. Die Dissertation wurde in der vorgelegten oder in ähnlicher Form noch bei keiner anderen Institution eingereicht. Ich habe bisher keine erfolglosen Promotionsversuche unternommen.

Hannover, den 30.10.2012

Danksagung

Abstract

Coastal and near shore areas offer a large potential for offshore wind energy production due to strong and steady wind conditions. Thousands of offshore wind energy converters are projected for mass production within the next years. Detailed understanding of the extreme, dynamic wave loads on offshore structures is essential for an efficient design.

An efficient design requires a load assessment with detailed knowledge about wave impacts and modeling, which is why breaking wave loads were investigated by the research project "GIGAWIND alpha ventus - Work-package 1" within the network "Research at Alpha VEntus" (RAVE). Large scale tests (1:12) in the flume "Großer Wellenkanal" of the "Forschungszentrum Küste" (FZK, Hannover) and numerical simulations were performed to reveal further insights on kinematics, pressures and forces due to different types of wave breaking. The physical model tests are described as well as the validation of the numerical model by comparison of CFD wave gauge data and pressures with measurements in the large wave flume inside and outside the impact area.

The impact areas due to a broken wave, a curled wave front as well as for wave breaking directly at the structure with a partly vertical wave front are compared to each other. Line forces in terms of slamming coefficients with variation in time and space are derived from CFD results and the velocity distribution is presented at the onset of wave breaking. In addition, local pressures calculated by three-dimensional numerical impact simulations are compared to the large wave flume experiments. The good agreement of the experimental and numerical results is presented and subsequently derived slamming coefficients are compared to load calculations based on guidelines. The main results about the characteristics of the different breaking types, i.e. in terms of range, impact duration, peak values and peak locations, as well as local and total impact forces are given in Chapter 6 and are summarized at the end.

Keywords: Wave breaking; Wave impact; Pressure distribution; Line force; Slamming-Coefficient; CFD;

Kurzfassung

Meeres- und Küstengebiete bieten auf Grund der starken und verhältnismäßig stetigen Winde ein großes Potential für Offshore Windkraftanlagen. Innerhalb der nächsten 10 bis 20 Jahre ist die Installation mehrerer tausend Windkraftanlagen in der Nordsee geplant. Für ein effizientes serienreifes Design werden unter anderem möglichst detaillierte Informationen über die zu erwartenden Extremlasten benötigt.

Vor diesem Hintergrund wurden im Rahmen des Forschungsprojektes "GIGAWIND alpha ventus - Teilprojekt 1" im Forschungsverbund von "Research at Alpha VEntus" (RAVE) im "Großen Wellenkanal" am Forschungszentrum Küste (FZK) Modellversuche im Maßstab 1:12 durchgeführt, um die Intensität und Position von Extremlasten durch Wellenschlag zu untersuchen. Mit Hilfe der Versuchsdaten wird ein CFD Modell für die Simulation der Druckschlaglasten validiert, das weitere Details über die auftretenden Drücke und Kräfte liefert, die durch unterschiedliche Abstände des Wellenbrechens vor der Struktur verursacht werden.

Untersucht und miteinander verglichen werden eine bereits vor der Struktur gebrochene Welle, eine Welle mit übergeschlagener Brecherzunge und eine unmittelbar an der Struktur brechende Welle mit teilweise senkrechter Wellenfront. Die CFD Simulationen zeigen gute Übereinstimmungen im Vergleich zu den Messdaten aus dem Großen Wellenkanal und bieten fortführend sehr wertvolle Möglichkeiten für zusätzliche Analysen, insbesondere für nur schwer messbare Größen der brechenden Wellen. Mit den Simulationen wird die vertikale Verteilung der Liniekräfte entlang der Struktur untersucht, deren Ergebnisse schließlich in Form von zeit- und ortsaufgelösten Slamming Koeffizienten dargestellt werden. Ergebnisse über die lokalen Druckentwicklungen durch die verschiedenen Formen des Wellenbrechens, bspw. die Bereiche mit Druckschlagcharakteristik, Wirkungsdauer, Belastungsspitzen und deren Positionen sowie die zeitabhängige Gesamtbelastung mit quasi-statischem Anteil, werden in Kapitel 6 beschrieben und am Ende zusammengefasst.

Schlüsselwörter: Wellenbrechen; Druckschlag; Druckverteilung; Linienlast; Slamming-Koeffizient; CFD;

1

Contents

List of Figures

List of Tables

List of Variables

Symbol	Description	Dimension
c	Wave celerity	m/s
C_D	Drag coefficient	–
C_M	Inertia/Added mass coefficient	–
C_S	Slamming coefficient	–
d	Water depth	m
D	Cylinder diameter	m
f_{ref}	Reference force $= D\,\rho\,c^2$	N
$F_{x,max}$	Total horizontal force	kN
g	Gravitaion	m/s^2
H	Wave height	m
H_B	Breaking wave height	m
H_{sig}	Significant wave height	m
L	Wave length	m
L_B	Breaking wave length	m
P_{ref}	Reference pressure $= \rho\,c^2$	Pa, N/m^2
R	Cylinder radius	m
s	Bottom slope	–
t	Time	s
T	Wave period	s
T_B	Breaking wave period	s
T_i	Time until front cylinder half is submerged $=$ R/c	s

Symbol	Description	Dimension
v	Water velocity	m/s
W_{kin}	Kinetic energy	Nm
x_B	Wave breaking distance to cylinder	m
z	Vertical coordinate in fluid domain and flume	m
η_{max}	Maximum water elevation	m
ρ	Water density	kg/m^3

1 Introduction

1.1 Motivation

Efficient technical solutions are needed for the several thousand projected Offshore Wind Energy Converters (OWEC) in the North Sea. Thus designs are being optimized constantly for batch production, which drives the motivation for this work from the engineering point of view. This study on the interaction of breaking waves and foundation structures intends to further increase knowledge about the pressure characteristics in the slamming area, resulting forces as well as the hydrodynamics around the structure, which will be specified in more detail in section 1.2. More detailed information about the processes involved, allows more economical OWEC designs, since extreme waves are generally a major design concern and the implied underlying uncertainties result in overestimated designs.

In addition to the engineering aspects the motivation based on the political framework is given by the governmental aim to reduce the annual CO_2 emission until 2050 down to 20% of the annual emission from 1990. Therefore, 45GW of installed wind energy production including 10GW from offshore wind farms in the North and Baltic Sea are projected among other measures until 2020 (BMU (2010)). Furthermore, 85GW of installed wind energy production are targeted for 2050 with a major increase in offshore wind energy production, while the onshore contribution to the 85GW is supposed to be nearly constant after 2020 (Nitsch (2008)). In 2010, wind energy has increased most in the field of renewable energy, followed by hydropower and photovoltaic (REN21 (2011)). This underlines the global request for wind energy and the currently growing demand for efficient offshore wind solutions.

Therefore, the combination of the three summarized aspects provides the motivation for this work:

- Political environment in regard to the targeted energy production by offshore wind farms.

- Demanded and efficient engineering solutions for the mass production of offshore wind converters.

- Progressively cumulating reports of rogue wave impacts around the world.
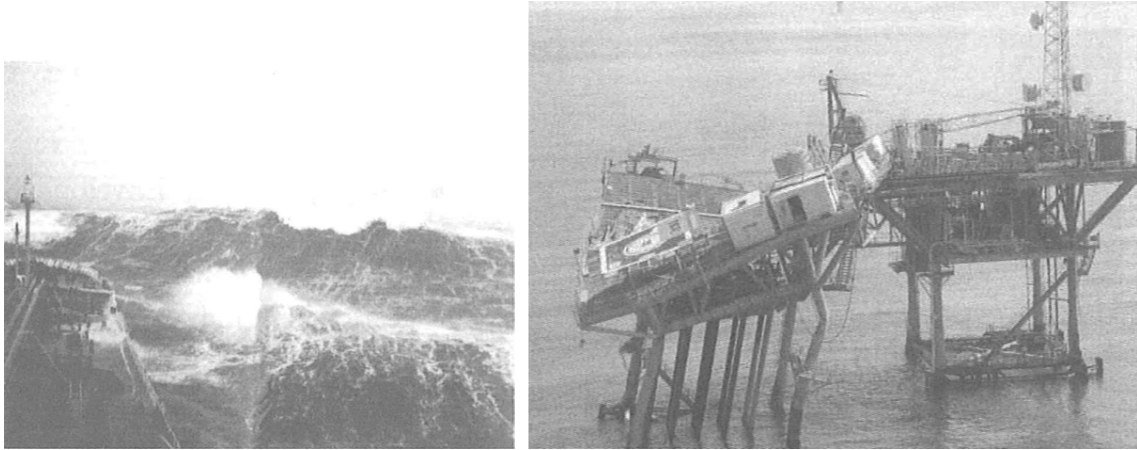
Figure 1.1: Freak wave observation from a cargo ship (Faulkner (2000)) and damaged oil platform EUGENE ISLAND 322 in the Gulf of Mexico in 2002 (Nickerson (1993)).

Before the demand for extreme wave load calculations was generally accepted, reports of rogue waves have been considered as legends told by surviving seamen. However, with the developing of heavy oil industry more and more reliable evidence, as seen in Fig. 1.1, was collected due to the increasing number and sizes of oil rigs as well as from observations by tankers (Clauss (2010)). In addition, sea state measurements at various locations around the world also prove the unfrequent events of freak waves (Schlurmann (1999)). Nikolkina and Didenkulova (Nikolkina and Didenkulova (2012)) have collected evidence of rogue wave phenomena with damage or human loss all over the world from 2006 until 2010. Fig. 1.2 shows the numbers and proportions of 78 rogue wave events (out of 131 in total) with heights two times larger than the significant wave height. As can be seen in the pie chart, 50% of the rogue waves occur in deep (open sea) and shallow (depth $d<$50m and $d/L<$0.5) water, while the other 50% of the collected events incident at the coastline (Fig 1.2, left). However, 38.5% of the rogue waves with damages or human losses occur in shallow waters up to 50m water depth, which matches the installation conditions for the above mentioned offshore wind farms. Most freak wave reports are about wave slamming on vessels (Fig. 1.1) with damage at high levels above the still water line (i.e. lost containers, smashed windows of cabins and ship bridge), which indicates high pressures and forces rather locally near the wave crest elevation. These local and intensive forces are required for the design of substructures in the slamming area. In addition, time depending total forces are of significant practical importance for fluid-structure-interactions, since the dynamic characteristics of the loaded system (stiffness, damping, etc.) must be considered for structural analysis of long and relatively flexible components, i.e. OWEC towers.

An impressive example of a high breaking wave with relevance to OWEC in the North Sea was captured by a webcam located under the helicopter deck of the FINO I platform ("Forschung In Nord- und Ostsee", Fig. 1.3). The location is 45km North of the island Borkum and is of particular interest for the offshore wind industry, since wind farms are
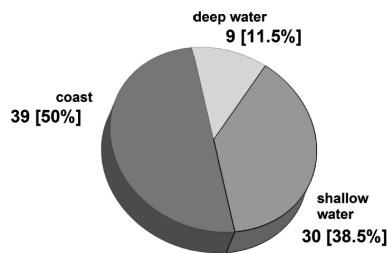
Figure 1.2: Statistic on observed rogue wave events (left) and snapshot of Mavericks surfing competition on 13th February 2010, where two unexpected 6m waves "wiped out" spectators from a wall (Nikolkina and Didenkulova (2012)).

projected and installed (i.e. the test-field alpha-ventus) near this location with a water depth of approximately 28m. Fig. 1.6 at the end of this chapter shows a sequence of snapshots shortly before wave breaking (Fig. 1.6 a), followed by the breaking wave crest, the subsequent wave trough e), and finally the subsequent wave crest f). The hand rail is roughly 15m above LAT (Outzen et al. (2008)). LAT is roughly on a level with the trough after the breaking crest (1.6 e), which indicates the LAT zero level. The images reveal a wave height of approximately 15m and a wave period of roughly 9s observed from crest to crest. In addition to this illustrated wave a wave with similar height was recorded again, eight hours later. Furthermore, the hand rail was damaged (again) by 17-18m high waves with a significant wave height of 10.5m (Outzen et al. (2008), Fig. 1.3) during storm "Tilo" on the 9th November 2007.

Documented wave incidents like these along with the observed damages at large ships, the occurrence of rogue waves and their impact on structures has become a major topic in the ocean engineering research community (Clauss et al. (2011)). Reports on freak waves increase due to the growing number of oil platforms and large ships (Clauss (2010), Nikolkina and Didenkulova (2012)), which increase the number of rogue wave impacts on structures and ships survived by seamen (not the frequency of occurrence of the rogue waves). This kind of proof and detection will probably further increase with the installation of several thousand monitored OWECs in shallow water areas. However, the prediction of rogue waves is still part of current research in combination with studies on wave evolution. Surface waves accumulate their energy from momentum input by turbulent wind and weak, resonant, nonlinear wave interaction over thousands of periods (Babanin (2011)). In contrast to the evolution, wave breaking and dissipation lasts only a fraction of the wave period (Rapp and Melville (1990)), whereupon the wave may loose more than half of its wave height (Liu and Babanin (2004)) corresponding to 75% of the energy.

There are three possible physical mechanisms to explain the formation of rogue waves, which are superposition of waves and/or modulation instability as well as wave current

interaction (Clauss et al. (2011)). All there processes basically lead to increased wave crests and subsequently to wave breaking, however, the mechanisms are different. The superposition of waves is the sum of (independently) progressing waves until the wave crest becomes unstable. The modulation phenomenon is associated with different group velocities of frequencies within a wave train, which leads to wave focusing and therefore to the formation of a single or a small number of exceptional high waves within the wave train. These two processes may occur almost everywhere in the water, while the interaction of waves and counter-currents is mostly observed in areas with strong currents over long distances, i.e. at the east coast of Africa where storm waves from Antarctica encounter the Agulhas current. Even if the physical mechanisms would be known to the full extend, the question for the probability of occurrence of extreme waves at a specific location remains. Gemmrich and Garrett (2011) underline that "even if an extreme wave with a scaled crest or wave height is predicted to occur only once every 30 years at a fixed location, a fleet of 100 ships would experience it every few months (though less frequently, of course, if attention is limited to high sea states)".

The illustration of the ship fleet similarly applies for the high number of projected OWECs, which underlines the motivation to gain advanced knowledge about the hydrodynamics, pressure characteristics, and forces due to impacting waves on offshore foundation structures. The following sections briefly describe the objectives and the scientific approach of this work.
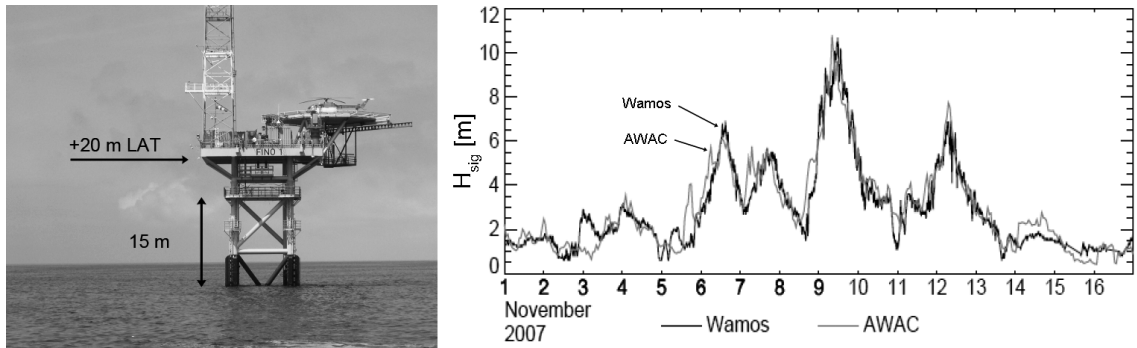
Figure 1.3: Positions above lowest astronomical tide (LAT) of FINO I (left, BSH) and H_{sig} measurements during storm "Tilo" (right, Outzen et al. (2008)).

1.2   Objectives

The objectives are motivated by the research project "Holistic design concept for OEWC support structures on the basis of measurements at the offshore test field alpha ventus ("Gigawind alpha ventus", FKZ0320532)". The overall task of the interdisciplinary research project is to reduce construction costs of OWEC support structures by the investigation

of the civil engineering topics loads, durability, foundation, structure models and holistic design. Within the framework of this project the work package "loads" (WP1) partly provides the motivation for the objectives listed below. Large scale experiments and numerical simulations are performed with different types of wave breaking on a tripod structure, which is illustrated in Fig. 1.4 (middle) and further described in Chap. 3, to investigate the objectives for slamming loads on a circular cylinder, which is a typical construction element for offshore structures.

1. **Insights about spatial pressure development for different wave impacts:** Local pressure characteristics due to impacting waves on a cylinder structure have already been investigated by former experimental studies. However, the results about maximum pressures and their positions vary in literature and all studies underline the significance and influence of entrapped air on the results. Therefore, large scale experiments were performed to minimize the scale effect of combined air- and hydrodynamics.

   - The peak pressures and their locations on the cylinder surface will be analyzed for different types of wave breaking to characterize and localize the impact zone.

   - Time dependent characteristics of the developing impact area as well as oscillation frequencies in the pressure sensors will be shown along the cylinder's span.

   The spatial pressure characteristics are useful for local design demands for primary and secondary steel constructions, coating systems, as well as for the estimation of total forces, specified by objective number three.

2. **Setup of a CFD model for impact simulations:** The detailed pressure information from the analysis above in conjunction with additional measurements from the experiments are used to set up a three-dimensional CFD model (Fig. 1.4). In this way more detailed information can be gathered around the tripod at locations hardly accessible for measurements. Furthermore, challenging measurable parameters like pressures and the complete wave-associated flow field around the tripod structure are accessible for investigations.

   - Numerical setup and validation of the CFD model to analyze pressures and forces on the complete tripod surface as well as breaking wave kinematics.

   - Integrated pressures are analyzed to obtain time dependent local line forces along the cylinder's span.

   Even though CFD simulations represent the physics expressed by numerical approximations, they are a promising tool for the above listed objectives, as pointed out at the end of Chapter 2.
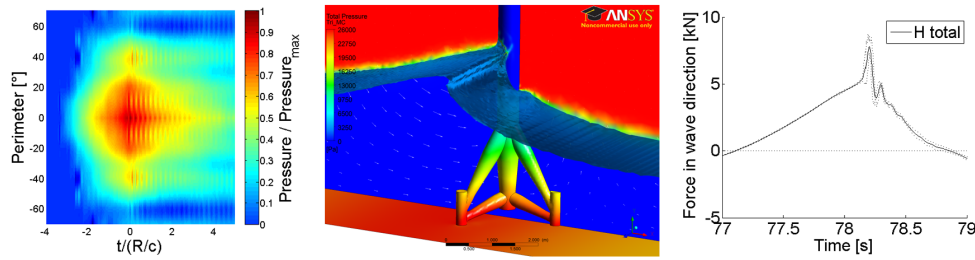
Figure 1.4: Examples for the pressure intensity of a slamming wave in the GWK model (left), wave breaking in the CFD model (middle), and time-dependent total horizontal forces (right).

3. **Estimation of time-dependent local and total forces:** Local line forces and their variation along the structure are of major interest for the designing process and assessed in this work. Another major design objective is the bending moment at the mud line composed of the local line forces multiplied by the corresponding lever arms.

   - The developing slamming loads in space and time are investigated and the influence of local impact pressures on line and total forces will be pointed out.

   - The ratio of slamming and quasi-static loads are investigated for different wave breaking positions.

   - Current approaches lack information about vertically distributed loads in the slamming area and the extent of the lever arm. With the information about the local line forces the time-dependent lever arms of the total horizontal force is calculated for the breaking wave types.

4. **Summarized results for practical purposes:** The primary reason for the above listed items is the need for load calculations due to breaking waves based on less conservative assumptions than currently used in practice for design purposes. Published studies provide more detailed information on slamming characteristics than accounted for by certified approaches. However, the studies were mostly performed in small scale experiments, which might be the reason for the scattering results and the details are not straight forward to use for engineering purposes.

   - Compact results for practical design purposes.

1.3   Outline

Fig. 1.5 shows an overview of the approach and the methods with indicated chapters of this work. Chapter 2 outlines the state-of-the-art with recommended practices for the estimation of slamming loads as well as included assumptions. In addition, further published studies and details about loads due to breaking waves are described followed by the remaining problems in conjunction to the above listed objectives. The large scale experiments, measuring sensors, and the wave test programm are documented in chapter 3 and several dimensionless numbers are introduced for illustration purposes and comparison to other studies. In chapter 4, the first part of data analysis from the physical model tests is carried out and summarized with preliminary conclusions. Afterwards, the configurations of the 2D and 3D numerical simulations are described in chapter 5 and direct comparisons to the large scale experiments are given in chapter 6 with further details about the breaking wave kinematics in the near- and far-field of the tripod structure.

Chapter 6.4 gives a brief discussion on the obtained results and methods with reference to published literature. Finally, this work is summarized in chapter 7 and further aspects for investigation are suggested in the outlook.
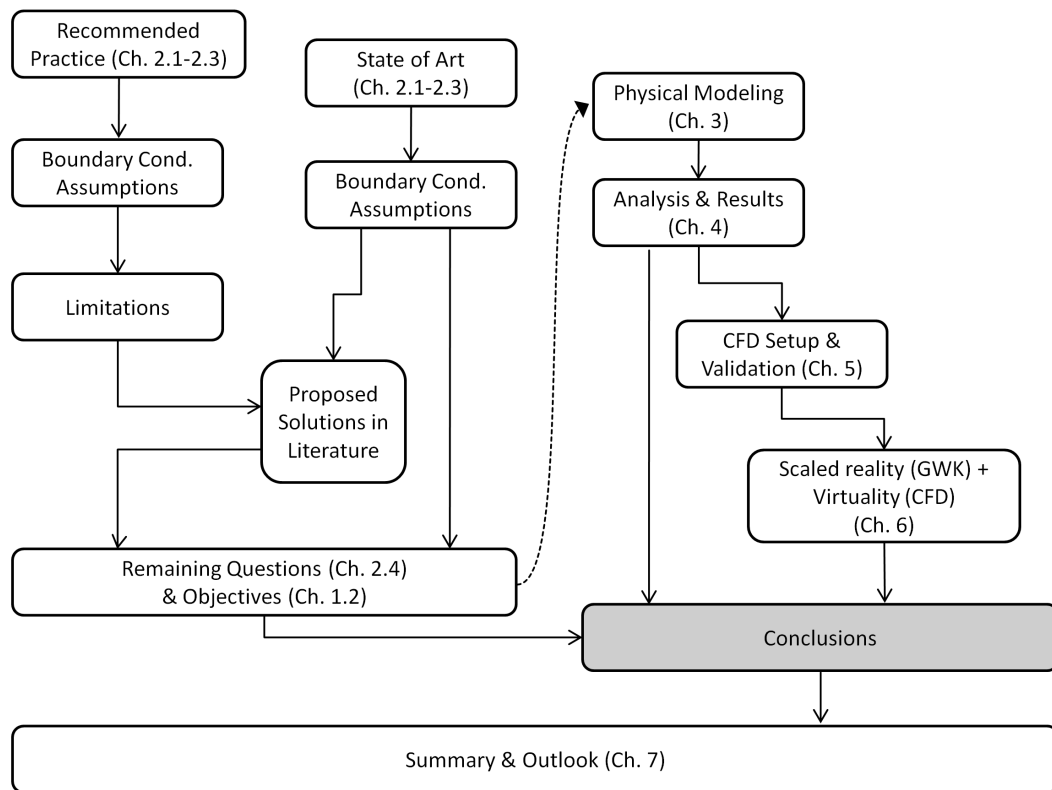
Figure 1.5: Work-flow-chart of this work with indicated chapters.

Figure 1.6: *Snapshots of an approximately 15m high breaking wave with a crest to crest period of 9s captured at FINO I on the 4th of October 2009. The time shifts of the frames in relation to snapshot a) are +1.402s (b), +1.682s (c), +2.383s (d), +6.2s (e, subsequent trough), +10.597s (f, subsequent crest). , For orientation, the center to center spacing of the main columns is 7.5m and the hand rail is 15m above LAT.*
(Source: Germanischer Lloyd)

2 State-of-the-art

Loads due to breaking waves on structures are generally called slamming or wave impact in literature. The phenomena of slamming loads and related pressures has been a challenging topic for several decades until now, since the studies of von Karman (1929). The early studies on slamming impacts are mostly analytical approaches due to the lack of appropriate measurement technics for this very localized and highly time-dependent slamming event. Furthermore, air bubble dynamics and other uncertainties keep this subject challenging in the presence of sophisticated measurement devices and numerical methods.
Nevertheless, a significant number of research activities have been carried out and the following sections aim to give an overview on slamming loads according to design standards and further publications on this matter. The governing parameters and the remaining problems about impact loads will be pointed out in the following.

Some basic information arises almost in every study on slamming loads and is therefore briefly described: Slamming loads are proportional to the squared fluid particles velocity hitting a structure's surface ($F_{Impact} \sim v^2$). The flow resistance is expressed by the kinetic energy required for the redirection of the flow around a structure. For laminar conditions the flow resistance is only induced by friction, due to the enclosed streamlines around the structure. Theoretically, the flow in front of and behind the cylinder has the same velocity and thus the kinetic energy remains the same. In contrast to the laminar flow, the streamlines of a turbulent flow are separated from the structure. The separated flow causes a pressure imbalance at the structure with high pressures on the front-side and a low pressure region on the backside, which causes a force in flow direction and vice versa for the trough of the wave. The magnitude of the force corresponds to the energy which redirects the initially straight flow aside the structure.
For example, a rectangular water volume with velocity v, cross-section A, and length l contains the kinetic energy:

$$\mathrm{W_{kin}} = \tfrac{1}{2}\, mass\ v^2 \;=\; \tfrac{1}{2}\, \rho A l\ v^2 \qquad\qquad (2.1)$$

The moment the volume encounters a structure, the fluid is deflected by a reactive force F along l exerted by the structure on the fluid, which is an essential term in literature and called flow force in this work:

$$W_{\mathrm{kin}} = \ F * l \ \Leftrightarrow \frac{W_{\mathrm{kin}}}{l} = F = \ \frac{\frac{1}{2}\,\rho A l\ v^2}{l} = \tfrac{1}{2}\,\rho A\ v^2 \qquad\qquad (2.2)$$

Obviously, the fluid velocity is a major parameter regarding the impact. Within the usual flow scenarios for offshore structure designs, breaking waves generate the highest water particle velocities near the crest. Due to the high velocities encountering the structure, they are continuously part of research activities and represent extreme load cases for designs.

Fig. 2.1 shows input quantities for the load assessment of breaking waves on structures and depicts the outline of the following sections. The first section deals with the estimation of the design wave height H and period T on the basis of long-term statistics and wave limits recommended by guidelines. Subsequently, an appropriate wave theory is required to calculate wave kinematics and the wave profile for the given wave height H, period T, and local water depth d.

In addition to the deterministic parameters, probabilistic aspects have major influence on the design procedure. Nearly all processes involved are affected by probabilistic means, especially the first part about the occurrence and dimensions of an extreme wave. Wave theories are deterministic, however, the onset of wave breaking and the developing wave front profile depends on naturally scattering boundary conditions, i.e. wave-wave interaction, current, wind, and bathymetry. Finally, the slamming loads at the structure are characterized by statistical properties as well, mainly due to air entrainment and their dynamics.

The overview in Fig. 2.1 illustrates the connections of the following three subchapters. All three subchapters are very interesting research topics with several unresolved questions. However, the subchapters 2.1 and 2.2 are included for completeness with regard to the slamming loads, since they provide essential background and boundary conditions for this study on slamming loads and the hydrodynamics involved, which are reviewed in section 2.3.

2.1   Design wave design

The concept of the design wave takes the influence of statistical parameters into account to achieve a requested level of safety for the construction of OWECs and the environment. The design values are adapted to scenarios and the structure's life time by design load cases (DLC), which regulate load combinations and periods of return.

In Germany, the installation of wind farms is administrated by the "German Maritime and Hydrographic Agency" (BSH) which is responsible for planing and developments in the exclusive economic sea area. In addition to wind energy, fishing, oil industry, military interests, pipeline alignment and sea lanes need to be managed and arranged. Among
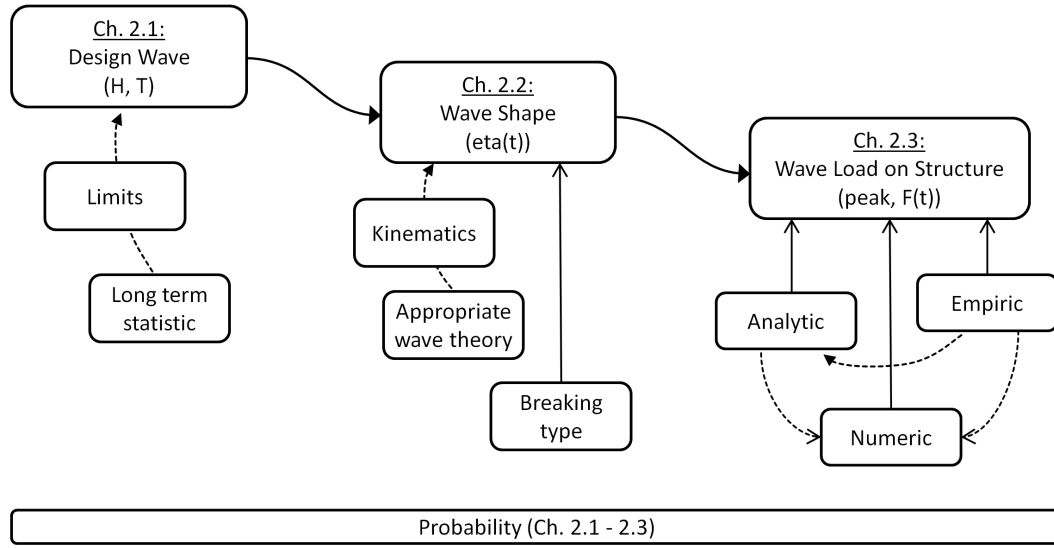
Figure 2.1: Design procedure with connected parameters for impact loads on structures.

other standards, the BSH provides a guideline on construction matters for the application of wind farm projects. This guideline refers to "German Institute for Standardization" (DIN), "Germanischer Lloyed" (GL) and "American Petroleum Institute" (API) standards. The responsibility of DIN, GL, API and BSH is to organize, steer, moderate and supervise the activities of standardization, i.e. for ship building and offshore structures. They safeguard the public interest and the quality of production by transparent procedures, advanced innovation and communication among research organizations and industry, i.e. the engineering demands and minimum requirements for offshore wind energy converters.

The recommended procedures and approaches for design parameter calculations are included in this chapter for subsequent comparison to further suggestions from the literature and to point out basic assumptions and remaining problems.

2.1.1   Wave limits and long term statistic

Extreme waves and breaking waves are distinguished without explicit classifications in standard DIN 61400 (DIN (2009)). It is stated that breaking waves in terms of spilling and plunging breaking have to be evaluated for local construction site conditions, however, it is not directly stated that the extreme wave has to be a breaking wave.
In general, the design life time for an OWEC is 20-25 years and extreme waves with a returning period of 50 years have to be accounted for structural safety by the design load cases (DLC) "shutdown/standstill" and "Transport and Maintenance". Estimated loads according to DLC "shutdown/standstill" are multiplied by a safety factor of 1.35 and multiplied by 1.1 for the latter DLC. According to DIN and GL the height of the extreme wave $H_{max,50}$ is estimated from a 3 hour sea condition with a return period once in 50

years. On the basis of $H_{sig,50}$ the maximum wave height is calculated by $1.86 H_{sig,50} = H_{max,50}$. The factor 1.86 is derived from

$$H_N = H_{sig} \cdot \sqrt{\ln(N)/2} \qquad (2.3)$$

with N equal to the number of waves and represents the statistically highest wave out of 1000 Rayleigh distributed waves. Additionally, waves in deep waters are limited by the maximum steepness H/L=0.142 according to the semi-theoretical wave breaking formula after Miche (1944) as well as by the shallow water wave breaking criteria $H < 0.78d$ (McCowan (1894)), which leads to the following minimum wave period for breaking waves for a given water depth according to DIN (2009):

$$T_B > \sqrt{\frac{0.78\text{d}}{0.14\frac{\text{g}}{2\pi}} \cdot \text{arctanh}\left(\frac{\text{H}}{0.78\text{d}}\right)} \qquad (2.4)$$

The properties of breaking waves are influenced by the interaction of wind and waves as well as by counter currents, as already pointed out in chapter 1.1. Wave crests are up to three times higher than troughs and may last only 33% of the wave period (see asymmetry in Chapter 2.2) in depth limited waters. Generally, wind farms are projected on plain or slightly sloping bottoms. In case of sloping sea floors, breaking wave heights can reach higher magnitudes (Barltrop and Adams (1991)) than estimated by the shallow water limit derived from constant sea floor conditions H=0.78d (McCowan (1894)). Rattanapitikon and Shibayama (2000) review 24 equations for wave breaking with comparison to collected data sets for verification. It was found that most equations allow a good prediction of breaking wave heights for gentle slopes s (0< s ≤0.07), which applies for the slope at the test-site alpha-ventus. However, the formula of Komar and Gaughan (1972) gives the best results over a wide range of experimental data and the Goda (1970) approach with modifications provides the best prediction for general cases including steep slopes s with 0.1< s ≤0.44, water depth at the breaking position d_B, and deep water wave length L_0:

$$H_B = 0.17\, L_0 \left(1 - \exp\left[\frac{\pi d_B}{L_0}(16.21\ s^2 -\ 7.07\ s -\ 1.55)\right]\right) \qquad (2.5)$$

The equation recommended by DIN and GL includes α =inclination of the slope and T_B =period of the breaking wave to estimate the breaking wave height:

$$H_B = \frac{1.6/[1+\exp(-19\cdot tan(\alpha))]}{1/depth + 44\cdot[1-\exp(-19\cdot tan(\alpha))]/g\cdot T_B^2} \qquad (2.6)$$

Since the design wave height is derived from the significant wave height, the estimation of $H_{sig,50}$ has major influence on the design wave height and period (Eq. 2.8), especially if
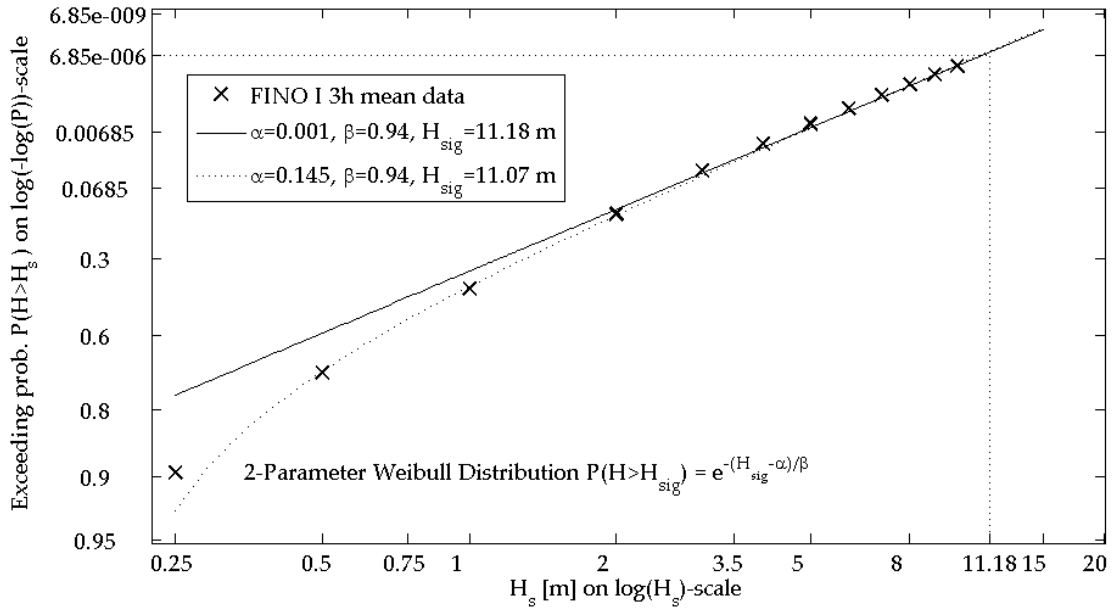
Figure 2.2: Weibull probability function extracted from FINO I based on 30min H_{sig} intervals measured between July 2003 until April 2011.

calculated by the statistical approach according to equation 2.3 due to the linear connection of H_{sig} and H_{max}. Furthermore, $H_{sig,50}$ sets the limits for T_B, which is subsequently used for the estimation of H_B according to equation 2.6. $H_{sig,50}$ is generally estimated from long term statistics due to the available field data limited in time and location. Therefore Goda (2010) and GL recommend the two parameter Weibull function for long term statistics to extract frequencies of occurrence for H_{sig} on the basis of relatively short measurements. Equation 2.7 shows the Weibull probability function with the shape parameters α and β:

$$P(H > H_{sig}) = e^{-\left(\frac{H_{sig}-\alpha}{\beta}\right)^{\gamma}} \tag{2.7}$$

With the parameter $\gamma=1$, the Weibull function becomes an exponential function with α and β as shape parameters for curvature or slope and the interception on the ordinate, respectively. Fig. 2.2 shows fittings of probability functions based on 3h mean H_{sig} and T_0 values of approximately 8 years from FINO I. The markers represent the probability of exceeding wave heights based on the scatter diagram shown in table 2.1. The solid line shows a constant least square fitting parameter $\alpha=0.001$ to get a straight line of best fit. The best fit of the data points and the fitting curve is estimated from the minimum differences between y-values. Similarly, the dotted line is a vertical least square fitting based on Weibull with α and β variable to get the best fit, whereas the x-axis is log scaled and the y axis is log(-log) scaled.

All H_{sig} values are taken from y=1/146000=6.8493-e6 (50 years x 365 days x (24h/3h)), which is the probability of exceedance of H_{sig} once in 50 years generated by a 3h storm.

Table 2.1: Relative frequency [‰] of H_{sig} and T_0 derived from 3h mean FINO I values - July 2003 until April 2011

H / T	3	4	5	6	7	8	9	10	11	12	13	Sum
9									0,1			0,1
8								0,1	0,1			0,2
7							0,5	0,3				0,8
6						0,7	3,2	0,4				4,4
5					0,7	10,8	2,7	0,1				14,3
4				1,9	27,9	14,7	0,7					45,3
3			3,9	86,5	61,9	5,5	0,5	0,4				158,7
2		23,3	193,9	144,2	31,0	4,1	0,8	0,2				397,5
1	2,0	119,8	107,9	35,9	5,8	2,2	0,5	0,1	0,2	0,3	0,1	274,8
0.5	8,0	52,9	25,6	7,4	2,5	1,1	0,2					97,7
0.25	0,5	3,6	1,6	0,4	0,1							6,2
Sum	10,5	199,6	332,9	276,3	130,1	39,1	9,2	1,6	0,3	0,3	0,1	1000

The fitting of the solid line takes all H_{sig} values $\geq$ 2m into account, which results in $H_{sig,50}$=11.18m for this threshold. In addition, the dotted line shows a two parameter fitting with less squared errors along the whole data set and increased curvature. The outcome is about $H_{sig} = 11.07$m for α=0.145 and β=0.94.

It should be emphasized here, that slight changes of the fitting parameters result in significant changes of several decimeters for $H_{sig,50}$. More details on uncertainties regarding extrapolation are described in Gemmrich and Garrett (2011). The least square fitting depends on the underlying data base, which differs i.e. by the amount of recorded years, and can be filtered with a lower wave height limit or by data selection of stormy winter months. In addition the extracted $H_{sig,50}$ wave height varies remarkably with small changes of the Weibull parameters. Considering these aspects shows that the prediction of the $H_{sig,50}$ value is not only based on statistical values but also influenced by the mathematical methodology. However, the 2-parameter Weibull distribution has been shown to fit wave data many times for long-term statistics in the North Sea (Dong et al. (2011) and Johannessen et al. (2002)). A linear fitted line by the least square method is generally used to predict long-term statistics for a specific parameter. In this case the available data base at FINO I with nearly eight years of significant wave height recording is used for a vertical linear least square fitting in the region $H_{sig} > 2$m (solid line, Fig. 2.2).

Under the above listed conditions a significant wave height of approximately 11.18m is likely to occur once in 50 years. As pointed out, the results are sensitive to the adaption procedure and primarily produced for illustration purposes here with regard to the "design of the design wave".

With $H_{sig,50}$ given, the zero-crossing period of the design wave T_D may be estimated from experience according to GL and DIN.

$$T_{max,50} = 11.1 \sqrt{H_{sig,50}/g} \leq T_D \leq 14.3 \sqrt{H_{sig,50}/g} \qquad (2.8)$$

Other predictions and observations of H_{sig} as well as maximum wave heights are found in literature for the North Sea. Lesny (2009) predicts values of $H_{sig,50}$=12m with a zero-crossing period of 11.8s. Average wave heights of 10m have been recorded at FINO I and single wave heights around 17m after storm "Britta" on 2nd November 2006. One year after, a H_{sig} value of 10.5m was recorded at FINO I with single waves heights around 17-18m during the low-pressure system "Tilo" on 8th and 9th of November 2007 (Outzen et al. (2008)). Especially the recorded waves illustrate the range of significant wave heights at locations for projected wind parks and literally impose the underlying risks. Even though the recordings at FINO I only last about one decade, observed values for H_{sig} are close to the estimated 11.18m and underline that high H_{sig} values should be taken into account for OWEC designs with an expected life-time of 20-25 year.

Table 2.2 gives an overview on the above listed parameters concerning the design wave derived from $H_{sig,50}$. The column in the middle shows results for the calculated $H_{sig,50}$=11.18m, while the adjoining columns differ by $\pm$1m to point out the sensitivity to the $H_{sig,50}$ value. As anticipated, the maximum wave height strongly depends on $H_{sig,50}$ due to the factor 1.86 in equation 2.3 and leads to a wave height of roughly 20.80m once in 50 years. The equations after Goda and GL mainly depend on the wave length and period and therefore indirectly on $H_{sig,50}$. They result in maximum wave heights around 17.5m and 23.9m, respectively. There is no distinct value for the corresponding wave period, however, equation 2.8 provides reasonable boundaries for $T_{max,50}$ and leads to a period between 12s and 14s in this case.
Nevertheless, the exemplarily estimated parameters ($T_{max,50}$=13s, $H_{max,50}$=20.80m) do not necessarily represent a breaking wave, since these parameters in connection with the water depth of nearly 30m at the FINO I location are close to but not beyond the breaking criteria of McCowan (1894). Thus, wave breaking is not guaranteed according to McCowan (1894), however, rather probable.

Two questions arise at the end of this section. The first one regarding the dependence of local and total impact loads in connection with varying maximum wave heights. If the contribution of the impulsive component would be similar for a 21m and a 18m high breaking wave, the sensitive estimation of $H_{sig,50}$ will be of minor importance.
The second question is about the probability of wave breaking at a specific location. While the first question will be discussed in chapter 6, the second aspect will be briefly described in the next paragraph, since it is not the focus of this work but an essential boundary condition for offshore designs.

Table 2.2: Design wave parameters and their sensitivity to changes of $H_{sig,50}$

Parameter	$H_{sig,50}$ - 1m	$H_{sig,50}$	$H_{sig,50}$ + 1m
$H_{sig,50}$ (Weibull)	10.18m	11.18m	12.18m
$H_{max,50}$ (Eq. 2.3)	18.93m	20.79m	22.65m
L=H/0.142 (Miche, 1944)	133m	146m	160m
$d_B = H/0.78$ (McCowan, 1991)	24.27m	26.65m	29.04m
Bathym. (d/distance to shore)	$6.7e - 4$	$30/45000$	$6.7e - 4$
$T_{B,min}$ (Eq. 2.4)	4.81s	5.05s	5.27s
T_B (Eq. 2.8)	11.31s - 14.57s	11.85s - 15.27s	12.37s - 15.93s
T_B selected for Eq. 2.5 & 2.6	12s	13s	14s
L_0 (Airy)	224.6m	263.6m	305.8m
H_B (Eq. 2.5)	16.8m	17.5m	18.0m
H_B (Eq. 2.6)	23.87m	23.91m	23.95m

2.1.2   Probability of wave breaking

The question about the probability of wave breaking at the structure is of major importance for offshore designs, especially for OWECs, since the probability of an occurring AND breaking design wave seems to be low. In addition, the impact load on a structure significantly depends on the breaking type (see Chapter 6), which have different probabilities of hitting the structure as well. The higher the pressure shock the lower becomes the likelihood of occurrence due to the connection to the vertical water front, which is an essential parameter for the intensity of the hitting water mass. Therefore the required magnitude of the considered impact event with a returning period once in 50 years might and could be questioned, since technical staff is generally not accessing the structures during heavy storm conditions and the OWECs itself do not endanger the ecological system in case of failure.

The wave breaking probability is commonly connected to the frequency of wave breaking expressed by the number of breaking crests per unit time. Findings from Battjes and Janssen (1979) according to a study on wave breaking in irregular waves are frequently referenced in literature. Their model predicts wave height variations across the surf zone by taking the depth-dependant breaking criteria from Miche (1944) with modifications into account as well as wave height dissipation. Furthermore, mean water level variations are calculated and finally the probability, if an arbitrary wave passing a given point is a breaking or broken wave. Thornton and Guza (1983) presented field measurements at the Californian coast and observed 10% wave breaking at the deepest location in contrast to 60% at the shallowest location in the test field. In addition to the observations of changing bathymetry, Banner et al. (2000) and Babanin et al. (2001) studied wave breaking for constant water depths, which applies to the bottom profile found in wind farm areas in the
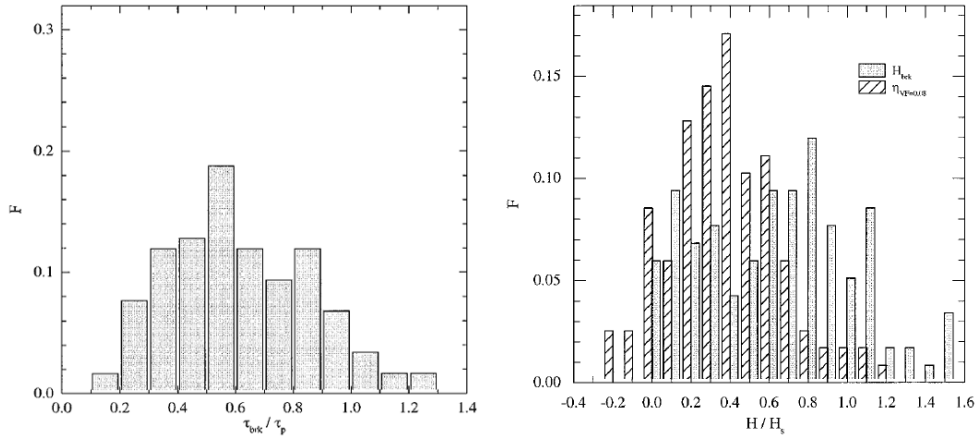
Figure 2.3: Distribution of normalized periods (left), heights (right, gray), and surface elevations at the onset of air entrainment (right, pattern) of breaking waves for H_{sig}=4.8m and T_P=10s. (Source: Gemmrich and Farmer (1999))

North Sea. Ochi (2003) as well gives an approach for the probability of wave breaking with known water depth. In this approach wave breaking is defined by spectral energy losses higher than 0.1 in combination with a breaking probability of at least 10%. Stansberg (2011) conducted a probabilistic analysis on sea state parameters wave energy and wave steepness in combination with slamming forces. Model tests with different sea states were analyzed and the maximum slamming forces correlate well with the sea state parameter as a function of wave steepness.

Gemmrich (2005) observed that the breaking frequency correlates with wind speed and less pronounced with the wave age, whereby a reduction in wave breaking was observed as the wave age increases. Field observations on breaking frequencies contain significant scatter and the inter-comparison of observations is not straight forward due to the lack of accepted criterions of breaking events, like elevation over depth, air entrainment, whitecaps or ambient noise. Measurements in the NE Pacific show that wave breaking occurs over a wide range of scales. Wave breaking was mainly detected for wave lengths considerably shorter than the waves containing most energy (dominant wave). 77% of the breaking waves have a period of 0.2 - 0.8T_P (dominant period) with H_{sig}=4-4.8m and T_P=9-10s (Gemmrich and Farmer (1999)). Similar results were obtained for various measurements with mostly unlimited fetch conditions. The measurements indicate that wave breaking predominantly occurs for wave periods smaller than T_P, and the highest probability is found for 0.5 - 0.6T_P, as illustrated in Fig. 2.3. Furthermore, the larger amount of breaking wave heights is below the height of the significant wave and the highest frequency of occurrence (12%) was observed for H_B/H_{sig}=0.8 (Fig. 2.3). Nearly 18% are higher than the significant wave height and 3.5% reach values 1.5H_{sig} in this case. The penetration depth of air entrainment was measured and used to indicate spilling or plunging breakers. An air/water fraction higher than 8% up to 0.2m below to surface indicates spilling breaking and a penetration

Figure 2.4: Illustration of kinematics and size of plunging breakers in the surf zone. (Source: Cazenave et al. (2006) & Pfeil (2004))

depth of 8% air up to 0.25m-0.75m below the surface indicates plunging breakers. In the open ocean less than 2% of the breaking events were detected as plunging breaking. At the Straight of Georgia with a mean water depth of roughly 150m 5-8% were identified as plunging breakers, and at the Gulf of Alaska with unlimited fetch length 9.5%, whereas the later is intensified by the combination of swell and opposing wind waves.

If these insights are related to the parameters from the previous section 2.1.1, the wave height with the highest probability of breaking during the storm occurring once in 50 years is $0.8H_{sig,50}$ and results in 8.94m height and represents 12% of all breaking waves. Only 3.5% have a wave height of $1.5H_{sig,50} = 16.77$m, while more than 90% of all breaking waves are spilling type breakers. Naturally, these numbers are only approximate values and the occurrences for the North Sea wind farm locations will be different (maybe slightly increased) due to less deep waters in comparison to the study above.

2.2   Wave shape

Subsequently to the estimated design wave height and period for a specific location, the shape as well as the particle velocities and accelerations need to be calculated by appropriate wave theories. Especially the shape of the breaker front is important for the slamming loads and the spatial and temporal development of the impact area at the structure. Both, the shape of the waves and appropriate wave theories for the calculation of the corresponding kinematics are outlined in this section.

2.2.1 Breaking wave types and asymmetry

Generally, breaking waves are classified into three types of spilling, plunging, and surging breaking.

Spilling breaker: Spilling normally occurs on beaches with flat slopes and steep or trochoidal waves. The onset of breaking usually starts some distance ashore and is seen by a foamy, turbulent water surface due to the unstable crest, which cascades down the front. They dissipate their energy over rather long distances due to an almost balanced system of turbulence along the wave front and contribution of momentum from the preceding trough.

Plunging breaker: The incoming waves are less steep and the sea floor is shallow to intermediate. They are typical surf waves and arched with a convex back and concave front (Fig. 2.4). The crest curls over until the wave plunges downwards and dissipates its energy over a short distance.

Surging breaker: The slope mostly remains unchanged while the front slides up a very steep beach with minor breaking and less energy dissipation.

The surf similarity parameter ξ is used to classify these breaker types, and therefore in some way the shape as well, by the ratio of the bottom slope $s = tan(\alpha)$, breaker height H_B, and deep water wave length λ_0:

$$\xi_B = \frac{s}{\sqrt{H_B/\lambda_0}} \tag{2.9}$$

Values between the limits of $0.4 < \xi_B < 2.0$ indicate plunging breaker, while smaller values are observed for spilling and higher ones for surging breakers (DIN (2009)).
The forces exerted by plunging breakers cause shock pressures and impulsive loads in most cases, while spilling and surging types may be regarded as quasi-static loads (CEM (2008)). The examination of various wave breaking positions in front of a cylinder by Wienke and Oumeraci (2005) underline this statement. The highest and most impulsive forces observed by large-scale tests were generated by plunging breaking right at the structure.

Waves are also characterized by their vertical and horizontal asymmetry. Wave crests are up to three times higher than troughs in depth limited waters and may last only 33% of the wave period (GL (2005)). For steep waves the profile becomes horizontally and vertically asymmetric and the front side of the wave crest is steeper than the backside of the crest. Based on experiments and high-speed films, Kjeldsen (1990) gives the following boundaries of crest front steepness ϵ, vertical asymmetry λ, and horizontal asymmetry μ for the inception of wave breaking in deep water (see definition sketch in Fig. 2.5.2):

$$0.32 < \epsilon = \eta'/L' < 0.78 \tag{2.10}$$

$$0.90 < \lambda = L''/L' < 2.18 \tag{2.11}$$

$$0.84 < \mu = \eta'/H < 0.95 \tag{2.12}$$

The asymmetry parameter can be applied to categorize various types of wave breaking (Kjeldsen (1990)), while the highest values given above correspond to plunging breakers in deep waters. Additionally experiments were undertaken at MARINTEK and the onset of breaking in time domain was found to occur for $\mu > 0.77$, which could be used to evaluate breaking or non-breaking as well.

2.2.2   Wave theories

There are no wave theories for the estimation of the kinematics under breaking waves. However, analytical and empirical models for impact loads require particle velocities in the region of the impacting wave, since particle velocities in breaking waves become considerably higher than in non-breaking waves, especially at the crest. Generally, it is assumed that fluid velocities are close to the phase velocity of the propagating wave right before the onset of breaking. Wave breaking begins when the crest velocities exceed wave celerity and this reasonable assumption offers the opportunity to calculate kinematics with available wave theories. Recommended theories for non-breaking waves may be chosen from Fig. 2.5.1 to approximate breaking wave kinematics for a given water depth d, wave height H, and deep water wave period T. The diagram shows the classification of various regular wave theories and was firstly presented by Le Mehaute (1969), based on $H/(gT^2)$ and $d/(gT^2)$. Subsequently, Dean and Dalrymple (1991) and Chakrabarti (1987) have developed the classification and the diagram is included in several standards, for example GL (2005) and API (1993).
The symmetric wave profile of all wave theories is a strong simplification for the calculation of breaking waves kinematics. The wave crest is symmetric to the crest point at the top and the wave shape remains the same during wave propagation. This is especially not true for plunging breakers, while spilling breakers are characterized by a steep wave profile and partly contain their shape over longer distances. In contrast, plunging waves break rather locally and implicate large wave deformation with energy losses up to the half of their wave height (Liu and Babanin (2004)).

Even though the wave theories do not completely represent the kinematics of breaking waves, the theories are often used to estimate design waves, since the calculation is several times faster than alternative calculations with FEM or CFD codes. Fenton (1985) presents a fifth-order analytical solution for periodic waves, which is not satisfactorily defining waves of large steepness and higher orders are needed. Several authors have presented numerical
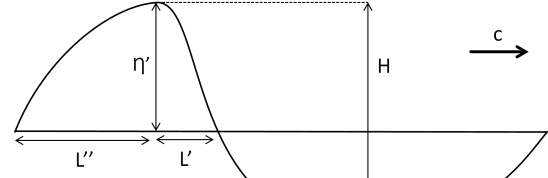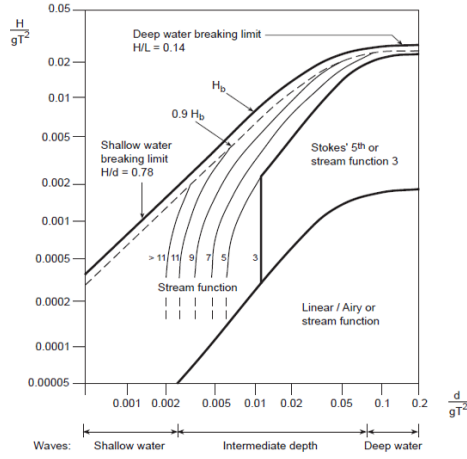
2.5.1: *Approximate boundaries for wave theories in regard to H, T, and d (GL (2005)).*

2.5.2: *Definition sketch for wave asymmetry parameters: crest front steepness ϵ, vertical-λ, and horizontal μ asymmetry factor.*

theories, however, the one established by Dean (1965) in conjunction with a tabulated set of results in Dean (1974) is mostly used in practice. According to the wave shape parameters relative depth and wave steepness in Fig. 2.5.1, the breaking waves investigated in this study (Chapter 3.2) fit to the profile described by a 9th or 11th stream function wave theory. Several assumptions like an impermeable and flat sea floor, the collinear propagation of disturbances and two-dimensional flow, incompressibility and homogeneous flow are necessary to solve for the analytical solution of a wave which propagates without change of form. The wave field is defined by stream functions rather than the velocity potential with the surface being the highest stream function with constant pressure to apply Bernoulli's equation. The equations are numerically solved, i.e. by trail and error, the secant method or besection, to calculate the coefficient X_n, the wave number $k = 2\pi/L$, and the stream line ψ_S at the surface (Eq. 2.13) to best satisfy the dynamic surface boundary condition.

$$\psi_S = c\eta + \sum_{n=1}^{N} X_n \sinh(nk\,(d + \eta))\,\cos(nkx) \qquad (2.13)$$

With the known stream function and surface profile, standard potential flow is used to calculate the other wave characteristics. Nowadays, higher order solutions can be calculated much easier in this way than by Stoke's analytical solutions due to the commonly available computational performance. Furthermore, the wave kinematics are solved up to the free surface and no stretching methods (i.e. Wheeler (1970)) are needed as required for the Stokes theory, especially for linear waves.

The fifth-order theory is generally acceptable for engineering accuracy and also recommended by DIN (2009) for steep waves in deep waters. Since spilling breakers predomi-

nately keep their shape, it is further suggested to estimate the kinematics by an appropriate
higher order stream function theory.

The numerical modeling of plunging breakers is hard to implement and the hydrodynam-
ics associated with wave slamming is complicated (DIN (2009)). Therefore, applied wave
theories for plunging breakers are only recommended for the area under the mean sea level.
Kjeldsen (1990) measured horizontal particle velocities in a transient wave nearly as twice
as large as predicted by Stokes 2nd order theory for waves with the same steepness. It is
emphasized that the higher velocities were obtained in the entire zone between mean sea
level and wave crest level. Furthermore, the horizontal particle velocities in the transient
wave exceed the phase velocity nearly in the entire zone above the mean sea level.

As described in the beginning of this chapter, the slamming problem mainly depends on the
involved fluid velocities before and during the impact. Thus, accurate velocity information
is needed to analyze the breaking wave loads in this work, which is not achieved by wave
theories. More accurate kinematics could be estimated from Fourier series due to the
capability of a very near approximation and the numerically solving of the fully nonlinear
equations. Another option is to solve the fully nonlinear equations by FEM or VOF/CFD
methods, which is used in this work and described in Chapter 5.

2.3   Prediction of breaking wave loads

Hydrodynamic forces are generally described by the superposition of the drag forces F_D,
inertia forces F_I, and in case of slamming by the additional component F_S:

$$F = F_D + F_I + F_S = C_D \, \frac{1}{2} \, \rho \, D \, u^2 \, + \, C_M \, \rho \, \frac{\pi D^2}{4} \, \frac{du}{dt} \, + \, F_S \qquad (2.14)$$

The three components describe a force per unit length along the center line of a cylinder and
are pointing perpendicular to the center axis of the member. The two first mentioned forces
vary rather slowly in time and are therefore usually handled as quasi-static forces without
taking the structure response into account. These wave loads are commonly calculated
by the equation of Morison et al. (1950) in combination with two coefficients C_D and
C_M for the drag and inertia load, respectively. According to equation (2.14) the inertia
force is assumed to be proportional to the horizontal water particle acceleration (du/dt)
relative to the cylinder, while the drag force is dominated by the squared horizontal velocity.
Both coefficients are empirical values and depend on several parameters like the structure's
shape, surface roughness as well as on wave characteristics. A significant amount of studies
were performed on this matter and published values for C_D and C_M considerably scatter in
literature. However, the Morison equation remains a useful approximation for engineering
applications and reference for recommended coefficients is made to GL (2005), DIN (2009),

Justesen (1989) and Sarpkaya (1986). Due to the increasing influence of diffraction effects, the approach of Morison et al. (1950) is limited to slender members with $D/L < 0.2$.

The third force accounts for the impulsive load due to a slamming wave front of a breaking wave. Among the various loads acting on marine structures, the slamming forces are the most intense, the most complex, and least known loads (Oumeraci et al. (1993)). There are analytical, empirical as well as numerical approaches and solutions to account for the slamming force, which is reviewed in the following three subsections.

2.3.1 Analytical approaches

The hydrodynamic problem of slamming is very complex due to the high number of physical processes involved. The complexity is generally reduced by several assumptions to solve the problem analytically. One of the first approaches to calculate the impact forces of a structure entering into water is given by von Karman (1929). His slamming model neglects viscosity effects as well as surface tension, which reduces the problem to irrotational flow conditions. Furthermore, air entrainment is not included and the water is assumed to be incompressible. Local flow acceleration is a key factor for slamming problems and dominant in relation to gravity, which is why gravitational acceleration is neglected as well. On the basis of these assumptions, the slamming force can then be written in terms of the changing hydrodynamic mass:

$$F_S = \frac{d(m_{add})}{dt}\, v \tag{2.15}$$

The added mass m_{add} is time dependent (dt) and changes with increasing submergence of the body, while the velocity v is assumed to be constant during slamming and denotes the relative velocity between water and the structure. The added mass calculation for the two dimensional case is simplified by von Karman (1929) as a flat plate with a submerged width w_s defined by the geometrical intersection of the still water level with the penetrating cylinder, while ρ represents the water density and R the cylinder radius.

$$m_{add} = \rho\frac{\pi}{2}\, w_S^2 \quad with \quad w_S^2(t) = 2\,R\,v\,t - v^2\,t^2 \tag{2.16}$$

Fig. 2.5 shows the progressing still water level or slamming wave front with $v*t$ as well as the wetted length w_s. Since the submerged section w_s is measured from the still water level, the raise of the free surface (pile-up effect) is not taken into account by the approach of von Karman (1929). This affects the theoretical duration of the impact as well as the local acceleration of the water and is therefore subject of preceding studies. The slamming force per unit length by von Karman (1929) is given by:

$$F_S = v\rho\frac{\pi}{2}\frac{d(w_S^2(t))}{dt} = \pi\rho R v^2\left(1 - \frac{v}{R}t\right) \qquad (2.17)$$

and restated in the following with regard to the slamming coefficient:

$$F_S = \rho C_S R v^2 \quad and \quad C_S = \pi\left(1 - \frac{v}{R}t\right) \qquad (2.18)$$

As can be seen in equation 2.18, the maximum slamming coefficient equals π at the instance in time the wave front hits the cylinder and linearly decreases to zero until the cylinder is half-submerged ($v * t = R$). Goda et al. (1966) adapted the approach by von Karman and extended the formula by a curling factor λ, which describes the part of the positive surface elevation η_b at the onset of breaking that contributes to the slamming:

$$F_S(t) = \lambda\eta_b \,\pi\rho R v^2\left(1 - \frac{v}{R}t\right) \qquad (2.19)$$

The part of the wave front which is connected to the curling factor is assumed to be vertical and moving with constant speed equal to the wave celerity. Thus, the term $\eta_b * \lambda$ describes the height of the slamming area with a constantly distributed load along the vertical cylinder's span.

The actual slamming duration becomes shorter in comparison to the duration estimated after von Karman (1929), if the pile-up effect is taken into account. The approach developed by Wagner (1932) takes the pile-up effect into account which results in a higher slamming coefficient. Fig. 2.5 illustrates the significant difference between the still water level or flat wave front and the deformed free surface around the immersed body. Based on the above named assumptions, potential theory can be used to solve the flow field and subsequently estimate the pressures by the Bernoulli equation. Wagner (1932) estimates the deformation
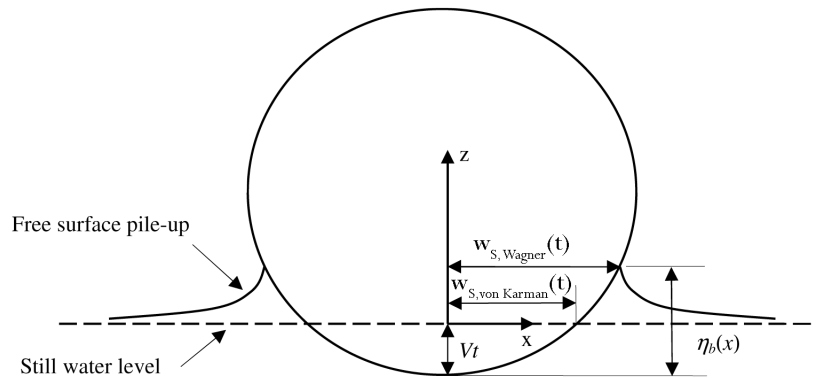
Figure 2.5: Definitions of parameters for an immersing cylinder from above into the still water (modified after ABS (2011)).

of the free surface from the integration over time of the potential flow around the cylinder. This leads to the penetration depth $\eta_b(x)$, which depends on the shape of the cylinder and gives the intersection points of the free water surface and the structure's boundary. The subsequent procedure is similar to the one given by von Karman (1929), since the obtained width of the time varying imaginary flat plate is then combined with equation 2.2. Finally, the resulting equation can be solved by a Taylor series, which approximates the contour of the wetted structure:

$$\eta_b = R - \sqrt{R^2 - x^2} \approx \frac{1}{2R}x^2 + \frac{1}{8R^3}x^4 \tag{2.20}$$

For small values of x, which denotes the onset of wave impact and progression of the wetted surface along the cylinder's circumference, only the first term with x^2 significantly contributes to the solution. The higher orders of x can be neglected, which leads to $w_S^2(t) = 4\,R\,vt$ (Faltinsen (1990)). The slamming force then becomes independent of time:

$$F_S = v\rho\frac{\pi}{2}\frac{d(w_S^2(t))}{dt} = 2\pi\,\rho R v^2 = C_S\,\rho R v^2 \tag{2.21}$$

This approach leads to a slamming coefficient of 2π and is therefore twice as high as the initial coefficient according to the method of von Karman (1929). The approximation of Wagner (1932) provides the peak pressure and was further developed by Wienke and Oumeraci (2005), since the first quadratic term only fits for small values of x at the initial moment of slamming. Wienke and Oumeraci (2005) indicate that further terms in the Taylor series do not significantly improve the accuracy of the wetted length, especially not when the value x is close to the radius R. Instead, they take the non-linear velocity terms of the Bernoulli equation into account to improve the temporal development of the impact. However, an analytical solution is impossible due to the non-linearity, which is why simplifications of the structure's shape in terms of the above mentioned approximations are required. They propose a stepwise function for the wetted surface, which extends the description of the impact to the total duration. The approach includes diverse load cases due to different states of wave breaking or inclined piles and the slamming force F_S is calculated by the following set of equations:

$$F_S = \lambda\,\eta_B\,\rho\,R\,u^2\,\cos^2(\gamma)\left(2\pi - 2\sqrt{\frac{u\,\cos\gamma}{R}t}\,\operatorname{arctanh}\sqrt{1 - \frac{u\,\cos\gamma}{4R}\,t}\right) \tag{2.22}$$

for slamming time t $0 \le t \le R\,/\,8\,u\,cos(\gamma)$ and
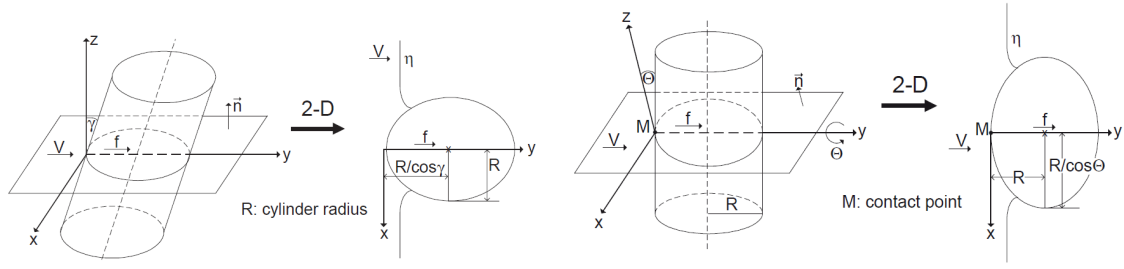
Figure 2.6: *Sketches of idealized wave impact for 2D wave fronts with arbitrary cylinder angles (left) and for the 3D spreading of the wave tongue (right) (Wienke and Oumeraci (2005))*

(a) Side view   **(b)** Front view   **(c)** Breaking wave on vertical cylinder ($\alpha=0°$)
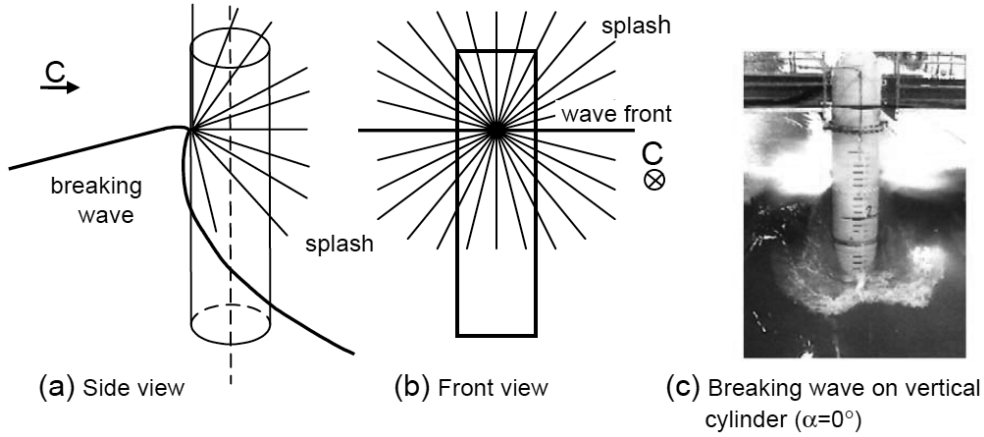
Figure 2.7: *Illustration of splashing and simplification of radial spreading planes (Wienke and Oumeraci (2005)).*

$$F_S = \lambda \, \eta_B \, \rho \, R \, u^2 \, *$$

$$\cos^2(\gamma) \, \left(\pi \sqrt{\frac{1}{6 \frac{u \, \cos\gamma}{R} \, t'}} - \sqrt[4]{\frac{8}{3} \frac{u \, \cos\gamma}{R} t'} \, \text{arctanh} \sqrt{1 - \frac{u \, \cos\gamma}{4R} \, t' \sqrt{6 \frac{u \, \cos\gamma}{R} \, t'}} \right)$$

(2.23)

$$\text{for} \quad \frac{3 \, R}{32 \, u \, \cos\gamma} \leq t' \leq \frac{12 \, R}{32 \, u \, \cos\gamma} \quad with \quad t' = t - \frac{R}{32 \, u \, \cos\gamma}$$

whereby the total duration of the impact is given by $T_S = 13 \, R \, / \, 32 \, u \, cos\gamma$. The variable γ represents the angle between the normal on the cylinder's span or surface and the flow direction of the hitting water mass. It equals zero for wave breaking with a vertical water front on an upright cylinder. The upper impact term includes the satisfying approximation based on the first term of the Taylor series. When x approaches R the wetted surface is better approximated by the second impact term.
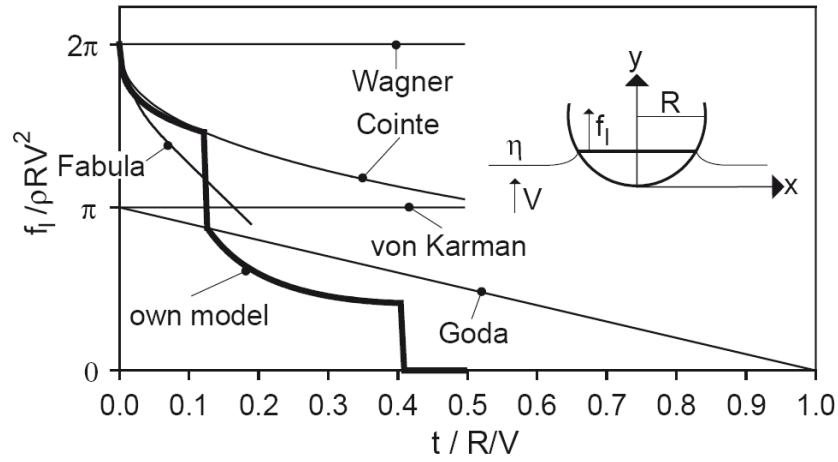
Figure 2.8: Slamming coefficient over time of immersion from various impact theories (Wienke and Oumeraci (2005)).

Fig. 2.6 shows the representations of the two-dimensional shapes of the cylinder for perpendicular and oblique wave impacts of the wave front. Oblique wave fronts due to curled wave crests are represented by elliptical shapes instead of circles. The same method as described above is used by Wienke (2001) to approximate the elliptic shape by an expanded mathematical series. Observations of slamming tests with various inclinations of the wave front have shown that the water spreads simultaneously along the surface of the cylinder on each horizontal section (Wienke (2001)). Fig. 2.7 illustrates the radial spreading of the splash in all directions, starting at the point of impact. Therefore, Wienke uses the previously described method to calculate the pressure tangentially along the elliptical cross-sectional planes. Subsequently, Wienke and Oumeraci (2005) integrate the force per unit length along the height of the slamming area by the application of the curling factor λ likewise to Goda et al. (1966). Wienke and Oumeraci (2005) estimated the curling factor by the ratio of the maximum measured total impact force and the theoretical force, which provides the height of the slamming area λ multiplied by the maximum water elevation η_B. In comparison to other theories (Fig. 2.8), the model by Wienke slightly overestimates forces in the first section and slightly underestimates the second segment. However, it is shown by Wienke (2001) that the theoretically estimated slamming forces correlate well with the measurements performed in the large wave flume. Wienke and Oumeraci (2005) note that the three-dimensional model is a rough simplification of the slamming processes, nevertheless, preferable for the estimation of the overturning moment at the cylinder's base.

2.3.2   Empirical approaches

Since the theoretical determination of impact loads is very complex and subject to several assumptions, laboratory experiments with steep and breaking waves are often used for the estimation of pressures and total loads. Due to the random nature of impact loads and its statistical scattering, the measurement of wave slamming is a challenging task. A significant amount of studies with measurements of local and total loads on cylinders as well as on similar structures can be found in literature. Experimental configurations deal with breaking and non-breaking waves and cover the full range of water conditions from deep to shallow waters. Most of the results are published in model scales or normalized. The following results will be scaled up to prototype conditions by using the Froude law, for comparison purposes. The offshore test site "alpha ventus" is chosen for reference purposes, since this work is connected to the research project "Gigawind alpha ventus" as described before. The tripod foundation structures are installed in 27-30m water depth and the diameter of the main column is 6m. As already pointed out in section 2.1.1, the breaking wave height is about 16-21m at this location.

Sarpkaya (1978) provides a simple method to calculate slamming loads by inserting an additional drag coefficient within the Morison equation. Rapidly changing slamming components were disregarded for the theoretical load description and total loads were fitted by the additional drag to measured data with the consideration of dynamic amplification effects. Furthermore, the coefficients are associated to specific structures and cannot be used for general application.

Campbell and Weynberg (1980) published an experimental fitting for a horizontal cylinder that penetrates trough a water surface. This study is commonly used for reference on this matter and recommended by DNV (2007). They observed a maximum slamming coefficient of 5.15 for the initial impact of the cylinder and the following temporal development with radius R and penetration depth $s=V{*}t$:

$$f_S = \rho C_S R V^2 \qquad with \qquad C_S = 5.15 \left(\frac{2R}{2R + 19s} + \frac{0.107s}{2R} \right) \qquad (2.24)$$

Sawaragi and Nochino (1984) investigated local slamming force coefficients as well as the distribution of the forces along the cylinder's span. Fig. 2.9 (left) shows the normalized vertical distribution for wave impact forces of three breaker types, classified by the given values for the surf-similarity parameter $Ir=slope/(H/L)^{1/2}$. Every breaker type is referenced by the maximum line force, which was measured for the type of breaking by semi circle wave force transducers. As illustrated by the solid line in figure 2.9, the vertical distribution can be approximated by a triangle with the peak near the relative height of 0.7. This applies for plunging as well as for intermediate breaker types, while spilling breakers also reach slightly higher peaks around 1.1. Spilling and intermediate forces were
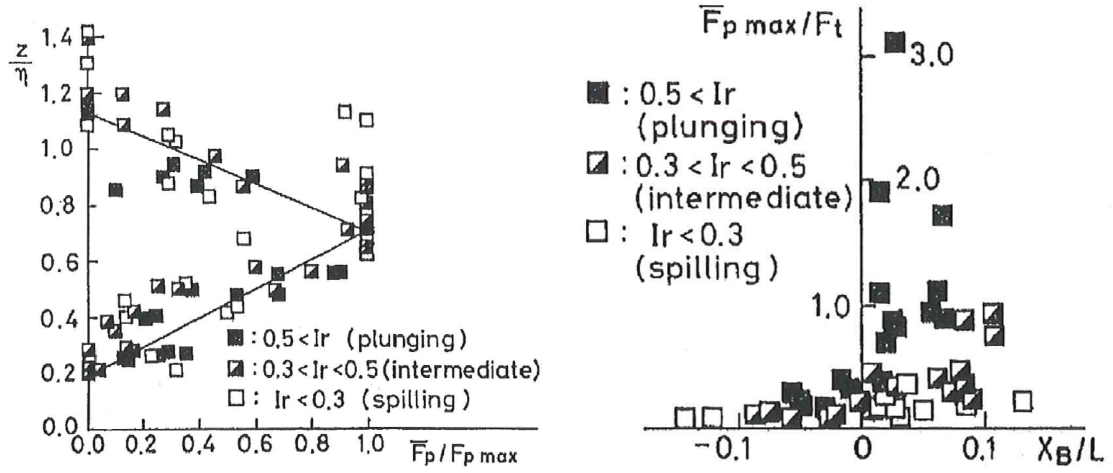
Figure 2.9: Normalized vertical distribution of peak values (left) and relation between $F_{p,max}/F_{Impact,Goda}$ and X_B/L_0 (right) Note, in this case the definition of Ir differs from Battjes (1974) due to the used wave height in front of the cylinder instead of H_0. (Source: Sawaragi and Nochino (1984))

observed up to relative heights of 1.4, while less maximum values around 1.2 were recorded for plunging breakers. Furthermore, Sawaragi and Nochino (1984) point out that force-time records clearly rise near the wave crest and records on a height with the still water level rise slowly without a characteristic sudden onset. However, peak values were reached almost at the same time along the cylinder's span.

Fig. 2.9 (right) shows the relation between the maximum observed forces and the impact force calculated by Goda et al. (1966) on the basis of a slamming coefficient $C_S = \pi$. The abscissa relates the distance of the breaking location X_B and the wave length L_{Airy} for deep water conditions. All maximum values for spilling breakers and regardless the breaking pattern are below 0.5, which corresponds to a slamming factor C_S of approximately $0.5\pi \approx 1.6$. The coefficients of spilling breakers are usually small and do not change remarkably along the breaking distance. However, the highest values were observed over a relatively long distance starting slightly behind zero up to $X_B/L_{Airy} \approx 0.12$. In contrast to the spilling type, the peaks of the plunging breakers only extend up to $X_B/L_{Airy} \approx 0.05$ behind the onset of breaking. Therefore, very high slamming coefficients were estimated for plunging breakers with values up to three times of π, which leads to $C_S \approx 9$.

Chaplin et al. (1992) carried out experiments for different model scales with a bottom-mounted cylinder and regular waves as well as breaking waves. In addition to local pressures, wave elevation, water particle velocities and global forces were measured. Focused wave groups were mainly used to generate breaking waves, while some experiments were conducted including bed slope. The maximum reported pressures are between 300kPa and 600kPa for prototype scale, which corresponds to local slamming load coefficients in the order of 2-4.
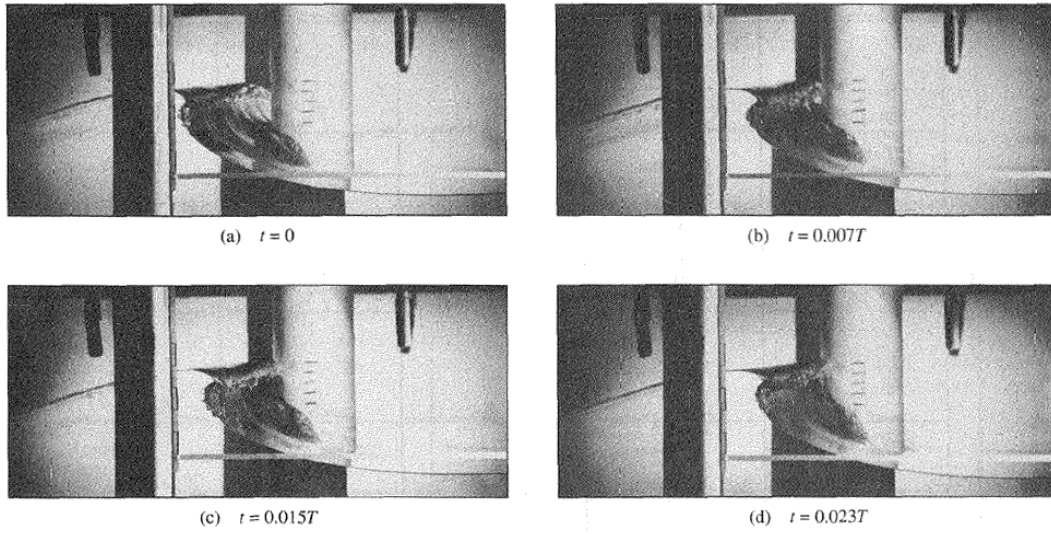
Figure 2.10: Development of the plunging wave breaking near the cylinder at dx/L=0.091 (Chan et al. (1991)).
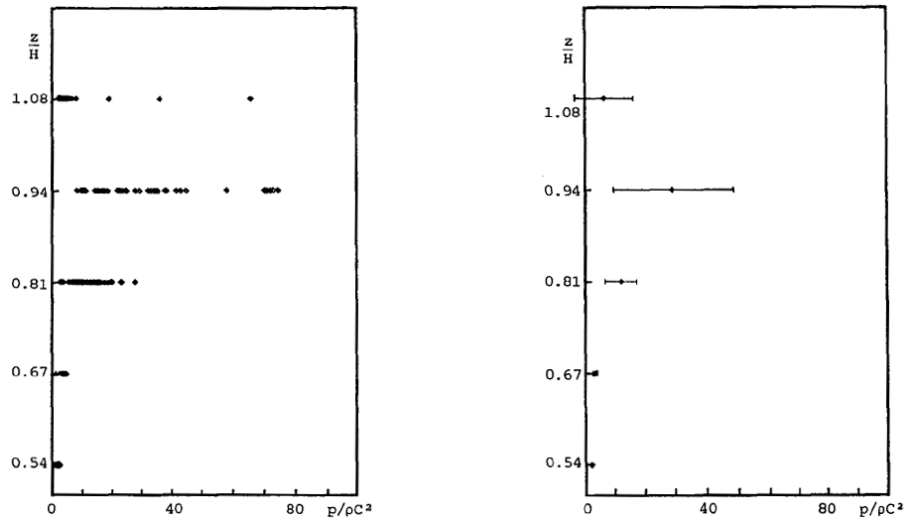
Figure 2.11: Vertical distribution of pressure maxima (left), mean values, and standard deviations (right) obtained from 50 repeated runs (Chan et al. (1991)). Note, H represents the maximum crest elevation η_{max} in this case.

As already observed by former studies and seen in Fig. 2.9 (left), local slamming forces and pressures are dominated by high fluctuations and scattering. This was investigated in more detail by Chan et al. (1991). Snapshots of a developing breaking wave, which is reproduced up to 50 times at the same relative cylinder location are seen in Fig. 2.10. Furthermore, the corresponding pressure characteristics of the plunging waves referenced to the stagnation pressure ρc^2 are plotted in Fig. 2.11. The highest recorded pressure peak along the cylinder's front is $74.7\rho c^2$ and occurs at the relative height z/H=0.94 with H = maximum crest elevation in this case (Fig. 2.11, left). On the same level, the lowest recorded peak pressure amounts $9\rho c^2$, which gives an impression of the high variability. Similar to Fig. 2.11 (left), the mean values of the dimensionless pressure peaks as well as the corresponding standard deviations are shown in Fig. 2.11 (right), which are 30 and ±20 ρc^2, respectively. The pressure intensity varies significantly as well as the relative pressure starting times, rise times, and the subsiding oscillations. Last mentioned may be reasoned by the randomness of entrapped air and the wave kinematics, particularly in the region of the wave crest. The relative location of the structure to the breaking position is of major influence as well. Based on the analysis of the experiments, Chan et al. (1991) characterize wave slamming by pressures higher $3\rho c^2$ and pressure rise times smaller than 1% of the wave period.

Furthermore, the variability of impact pressures due to the breaking wave front and entrapped air is published by Zhou et al. (1991). The dimensions of the 0.12m test cylinder in 0.6m water depth correspond to a scale of 1:50 with regard to the alpha ventus test field conditions in 30m water depth and for the 6m main column. Fig. 2.12a-e illustrate different types of wave breaking in front of the cylinder for various relative positions x/L. The vertical distributions of the mean peak pressures in Fig. 2.12 clearly show impact regions around $z/L = 0.052$ and 0.065 for the positions $x/L = 3.568$, 3.620, and 3.672. These impact areas are characterized by dimensionless pressures between 4 and $13\rho c^2$, rise times < 0.002 T, as well as by oscillations immediately following the pressure maxima. Pressures outside the slamming area are smaller than $2\rho c^2$ with rise times more than 0.003 T. Oscillations associated with the impact area diminish with increasing orientation along the perimeter. Furthermore, each cylinder location reveals decreasing pressures with increasing orientation at all levels z/L. In addition, the elevation of impact shifts downwards from $z/L = 0.065$ to 0.052 as the cylinder moves further downstream by $x/L = 0.1$. The time histories of the pressures are smoothly varying with low intensities in comparison to the locations in between at the cylinder positions "a" and "e" in figure 2.12. Therefore, Zhou et al. (1991) suggest that the vertical region of impulsive pressures is relatively small with values around $\Delta z/L = 0.03$, which corresponds approximately to the radius of the cylinder in this case. In the horizontal direction, the slamming characteristic roughly spreads 20 degrees to the left and right. The highest pressure measured within the impact area is about $32\rho c^2$, while the maximum of the averaged peak values is reduced to $16\rho c^2$ and was observed for the cylinder location "c" in figure 2.12.
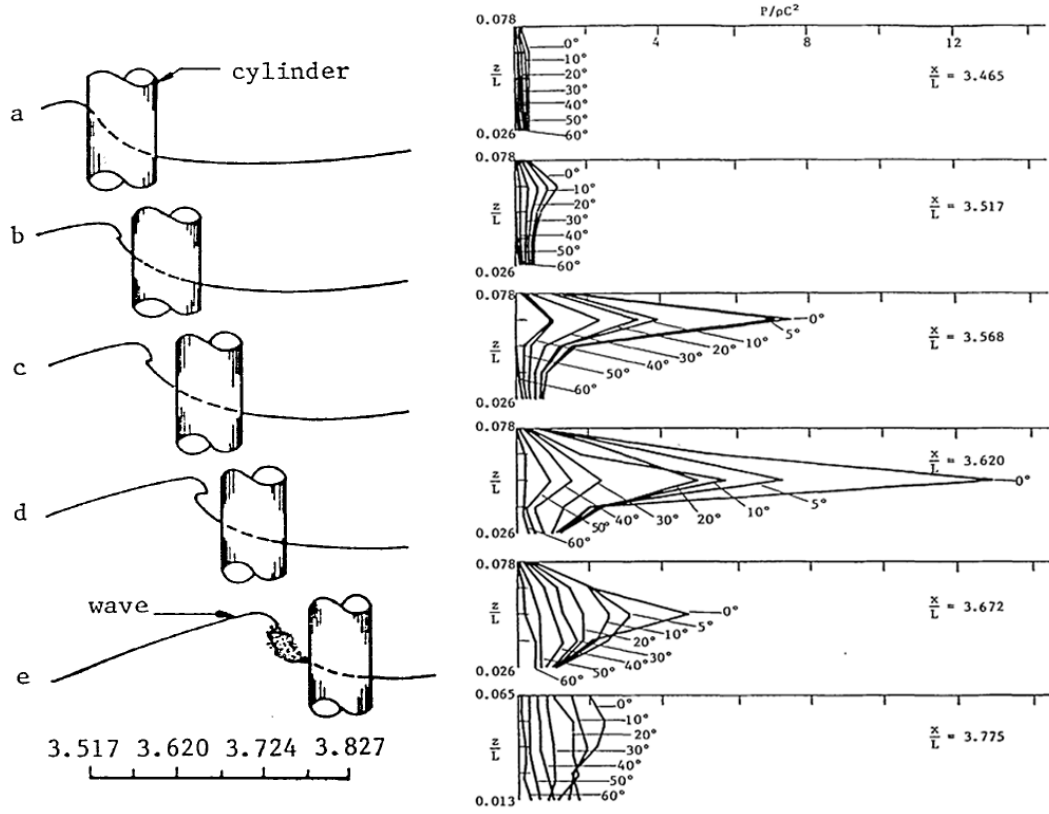
Figure 2.12: Left: Transient steps of wave impact for relative distances (x/L=3.517=+0m, 3.620=+10m, 3.724=+20m, 3.827=+30m, derived from model scale 1:50 with prototype wave length L=96.15m). Pressure distribution of mean peaks over relative heights z/L = 0.013, 0.026, 0.039, 0.052, 0.065, 0.078 and distances x/L for D/L=0.062 (Zhou et al. (1991)).

On the basis of the publications mentioned above as well as by further experiments Chan et al. (1995) classify breaking waves into stages I-V, which show significant sensitivity to the wave breaking position in front of the cylinder. However, the five types are mainly used to describe the relative development of a breaker at the cylinder and transition from one stage to the next is continuous. They are described including characteristics on pressures for reference purposes in this work.

Stage I Fig. 2.12 a: The incident wave front is still steepening while passing the cylinder and no jet formation is present when the wave crest reaches the position z/eta_{max} = 1.08. The pressure time histories at the cylinder front are smoothly varying with maximum values up to $2\rho c^2$ at z/eta_{max}=0.94. The rise time is about 0.0015 T at high locations and several times longer for lower locations.

Stage II Fig. 2.12 b: Jet formation has already begun prior to impingement and corresponding impact pressures are highly impulsive. Sharp increasing peak pressures were observed near the wave crest (z/eta_{max}=0.94) with values between 16 to $47\rho c^2$

and short durations about 0.001 T. Slamming characteristics with pressures $> 3\rho c^2$ were measured along the cylinder's span at z/eta_{max}=0.81-1.08.

Stage III Fig. 2.12 c,d: A plunging jet has already curled down shortly before impingement, however, has not plunged into the water. Pressures are characterized by double peak pressures at several elevations, whereby the first peak shows relatively more impulsive rise- and decay-times. Peak values range from 6 to $17\rho c^2$ and are generally lower than observed for stage II.

Stage IV Fig. 2.12 d,e: Plunging jet hits water surface just before the impact on the cylinder and air is entrained. Less intensive double peak pressures than observed for stage III were measured on lower levels z/eta_{max}=0.54 and 0.67 in the order of 5 to $13\rho c^2$.

Stage V Fig. 2.12 e: The broken wave front consists of an air-water turbulent mixture and pressure time histories show high fluctuations. The impact is considerably dampened by the foamy mass and peak pressures are mostly lower than $3\rho c^2$.

Wienke and Oumeraci (2005) performed a large set of slamming experiments in the large wave flume in Hanover. The diameter of the test cylinder corresponds to large scale conditions of 1:8.6 with regard to the alpha ventus test site and to crest elevations higher than 16m in nature. Several relative wave breaking positions are tested as well as various inclinations of the circular cylinder. Gaussian wave packets are used to generate the breaking waves at the specific locations around the cylinder. Local pressures as well as total forces are measured among other wave and structure related parameters. Local pressures up to $40\rho c^2$ were measured at the cylinder's span for the vertical cylinder arrangement. As previously described in section 2.3.1, these experiments were conducted to develop the approach given by the equations 2.22 and 2.23.

Suyuthi and Haver (2009) report about experiments in a wave basin consisting of a tension-leg platform with circular columns. Impact forces due to steep irregular waves are investigated by the application of force panels, which lead to local forces at the platform columns in terms of integrated pressures along the whole perimeter. Furthermore, this study is performed on a probabilistic approach including 3-hour storm waves for extreme North Sea states with a period of return once in 10000 years. On the basis of the estimated extreme particle velocities in Clauss (2010), the slamming load coefficients C_S are reported to be slightly larger than 10.

Arntsen et al. (2011) set up model tests with a fixed cylinder on a shoal for the investigation of loads due to breaking waves. Several ring force transducers were installed in the cylinder to cover the vertical load profile generated by regular waves breaking on the shoal. The model scale is 1:70 and represents a water depth of 28m, a phase velocity about 20m/s, and approximately 17.5m positive water elevation of the breaker in full scale. It was found

that the highest wave load appears in a relative height z/eta_{max}=13/17.5=0.74 with a slamming coefficient of C_S=4.27 according to equation 2.2.

2.3.3   Numerical methods

Nowadays, the keywords "numerical methods" apply to a broad field of problems and their solutions. They are used to solve partitions of a problem or the full problem. For example, the estimation of the wave load based on the Morison equation or von Karman and Wagner types of formulae requires the input of wave kinematics. Analytical wave theories show strong limitations when it comes to the description of steep and breaking waves as pointed out in section 2.2.2, especially in finite water depth. Numerical methods may then constitute more accurate alternatives. There are two different approaches that employ numerical methods to solve slamming problems:

- Fully numerical simulation can be used to predict the pressures on the structure as well as the wave-structure interaction. The wave-structure interaction includes diffraction effects and the time varying wave load is calculated by pressure integration. However, a high CPU performance is usually necessary and the numerical simulation may not be robust enough.

- Numerical models without structures are used to estimate kinematics of very steep and breaking waves. Subsequently, the impact forces are calculated by means of analytical models. The advantages of this procedure are the significantly lower CPU costs, larger time steps and a higher robustness. Furthermore, it can be combined with linear wave theory and only the wave breaking is solved numerically. However, wave diffraction is not fully taken into account and for the application of analytical slamming models empirical coefficients are needed.

Based on the conditions and assumptions made to calculate the fluid flow, numerical methods can be separated into two main classes:

- Potential flow methods, which are based on irrotational flow and neglected viscosity. For incompressible fluids, the Laplace equation is used as governing equation.

- Methods based on Navier-Stokes (NS) equations. It must be considered here whether the viscous flow is laminar or turbulent. Neglecting viscosity leads to the Euler equations. Wave breaking might generate vorticity, which can be captured by the Euler equations and by the Navier-Stokes equations.

This work uses a NS-equation solver in combination with the VOF method (Volume Of Fluid) for the slamming load simulations. For this reason the following references focus

on the VOF method to point out some characteristics of this method with regard to slamming problems. For other methods like potential flow simulations, smoothed particle hydrodynamics (SPH), or Boussinesq models the reader is referenced to Marino et al. (2011), Oger et al. (2010), and IEC (2009) among others.

Schmittner (2005) demonstrated results of numerical wave tanks for the nonlinear simulation of wave propagation in combination with wave breaking in a VOF model for fluid structure interactions. He used the commercial solvers COMET and FLUENT, which are based on the Reynolds-averaged Navier-Stokes equations and the volume of fluid discretization. Schmittner (2005) proposed a new coupling approach combining the advantages of both methods. The wave propagation is calculated with "WAVETUB" up to a predefined position in the wave tank where the boundary conditions are handed over to the VOF solver.

Corte and Grilli (2006) developed a numerical approach to define the transient load on a cylinder. The Finite Volume (FV) VOF model is used for the wave impact process. The free surface flow of the design wave around the cylindrical structure is simulated in the FV-VOF model. The numerical results are compared to pressure time series of the analytical method of Wienke (2001) (constant fluid density, one-phase potential flow) as well as to experimental results from Wienke (2001) and Wienke and Oumeraci (2005). In all cases the maximum pressures computed with the FV-VOF method are smaller than those predicted by Wienkes method. The differences are assigned to the averaged density in the FV-VOF model in contrast to Wienkes approach based on potential flow. For later stages of the wave impact, the numerical model is in good agreement with the experimental results.

Bredmose and Jacobsen (2010) use the CFD code "OpenFOAM" to determine the impact force on a cylinder by pressure integration. The forces are estimated as well by the Morison approach including the Wheeler stretching for the velocities above the still water line for comparison to the CFD results. Both methods result in nearly similar forces for initial small waves. However, the main impact forces based on Morison are smaller in comparison to CFD results. CFD solutions of a grid convergence study show no significant differences for coarse and fine grids.

Mokrani et al. (2010) investigated the impact force on a vertical wall due to a large plunging breaker by using a Navier-Stokes VOF model. They show total forces and the influence of the mesh size on the numerically solved peak pressures on the wall. The time series of the impact force is in good correlation to experimental data.

Pakozdi et al. (2011) show the demand for highly resolved meshes and small time steps to capture the pressure evolution of a slamming wave. Coarser grids and time steps can be used for wave simulation using second-order implicit time integration.

2.4   Summary, recommended practice, and remaining questions

2.4.1   Summary

The basic problem is to predict the time series of local and total wave forces on offshore structures induced by the complex flow field of breaking waves. The flow field depends on the wave shape and breaking type, which should be evaluated for the local conditions according to GL (2005) and DIN (2009) and gives the motivation for the different tested load cases in this work.

Extreme waves have a high potential for wave breaking, however, studies of Gemmrich and Farmer (1999) in the NE Pacific and the Strait of Georgia as well as studies of Gemmrich (2005) approximately 150km off Monterey (California) report the highest breaking probability for $0.8H_{sig,50}$, which quantifies 12% of all breaking waves as described in section 2.1.2. Furthermore, 90% of the breaking waves are spilling type and only 3.5% reach wave heights larger $1.5H_{sig,50}$.
The $H_{sig,50}$ wave is recommended by GL (2005) and DIN (2009) to be evaluated for 3h storm conditions once in 50 years. Section 2.1.1 describes the subject of the sensitivity of long term statistics for the selection of $H_{sig,50}$ (=11.18m in this case) and the subsequent choice of the extreme wave parameters. The breaking wave height is limited by equation 2.6, as suggested by GL (2005) and DIN (2009). There is no distinct value for the corresponding wave period to a given wave height, however, equation 2.8 provides reasonable boundaries for $T_{max,50}$ based on McCowan (1894) and Miche (1944). The estimation of wave parameters according to the actual guidelines (Chapter 2.1) are used for the selection of reasonable boundary conditions in the physical model and points out uncertainties within the design process, i.e. the estimation of the maximum wave height, the calculation of breaking wave kinematics, and finally the load assessment.

Table 2.3 gives an overview on published and certified approaches, which are based on theoretical formulations and experimental studies. As can be seen in the right column, specifications about the maximum loads and the proposed coefficients scatter, which is partly reasoned by the stochastic nature of breaking waves as well as by the experimental challenges to measure such impulsive events. The maximum slamming coefficient as described in section 2.3.1 is reported by Suyuthi and Haver (2009) with $C_S \approx 10$ from experimental studies. A similar high coefficient ($C_S \approx 9$), based on model tests as well, is observed by Sawaragi and Nochino (1984), while the theoretical slamming coefficients from Wagner (1932) and von Karman (1929) are 2π and π, respectively. The coefficients reduce down to empirical values of 5.15 (Campbell and Weynberg (1980)), 4.27 (Arntsen et al. (2011)), and 2-4 (Chaplin et al. (1992)). Furthermore, Sawaragi and Nochino (1984) dis-

tinguish between plunging and spilling breaking and report slamming coefficients around 1.6 for spilling breakers.

Impact areas spread up to 20° to the left and right of the cylinder span with characteristic pressures between 4-13ρc^2 according to Zhou et al. (1991). These pressure characteristics are observed on a length along the span approximately equal to the radius of the cylinder. Chan et al. (1995) report on impact pressures along the span of approximately 20% of the maximum crest elevation. Averaged pressure peaks of 30ρc^2 are found by Zhou et al. (1991) at a relative height z/eta_{max}=0.94, and the highest local pressures of 40ρc^2 are reported by Wienke (2001).

The variation of the slamming coefficients in literature in combination with the multiple reports on very intensive and fluctuating impact pressures provides the main motivation for the performed large scale experiments in this work. The measuring points of the pressure sensors as well as the selection of the breaking positions of the focused waves are chosen according to the reviewed studies. CFD modeling offers advanced analysis of the slamming process around and on the structure as well as more accurate wave kinematics than available wave theories and therefore used in this work.

Table 2.3: Overview of wave impact studies and essential results.

Authors	Model, Assumptions	Pressures, Forces
van Karman (1929)	Incompressible fluid, irrotational flow, neglected viscosity, air entrainment, and gravitational acceleration. Horizontal water velocity = wave celerity c and constant along cylinder span and over time.	$C_S = \pi$; (Equation 2.17 & 2.18)
Goda et al. (1966)	Extension of van Karman (1929) approach by the curling factor λ, which is assumed to describe the part of a vertical and constantly moving water front with wave celerity c.	$C_S = \pi$ and constant along span for $\lambda \leq 0.4$. Linear decreasing until cylinder front is immersed (Equation 2.19).
Wagner (1932)	Theoretical assumptions as van Karman (1929) for the use of potential flow theory. Taking into account the deformation of the free surface (pile-up effect), which reduces the impact duration and increases C_S.	$C_S = 2\pi$; (Equation 2.21)
Wienke (2001), Wienke and Oumeraci (2005)	Extension of Wagner (1932) approach and improvement of temporal development by a stepwise approximation of the wetted cylinder surface and introduction of load cases. Model tests with $D = 0.7$m, breaking wave heights up to 2.8m, water depth = 44.25m.	$C_{S,max} = 2\pi$, constant along span for $\lambda \leq 0.5$, and time dependent until $T = 13R/32u$. Local pressures up to 40 ρc^2 for the vertical cylinder. (Equation 2.22 & 2.23)
Campbell and Weynberg (1980)	Horizontal cylinder penetrating through a calm water surface with various constant downward velocities.	$C_{S,max} = 5.15$, time dependent until submergence of 2R, afterwards $C_S = 0.8$. (Eq. 2.24)
Sawaragi and Nochino (1984)	Model tests with wave breaking on slopes (1:15, 1:30) for various cylinder positions (D = 7 cm), 7-10 cm water depth, and 12 cm crest height. Hydrodynamic forces were measured by five half-rings.	$C_{S,spilling} = 0.5\pi$, $C_{S,plunging} = 3\pi$. Triangular distribution of loads with peak at $z/eta_{max} = 0.7$ for plunging and 1 for spilling.
Chaplin et al. (1992)	Breaking wave tests with different scales are conducted by wave packets and slopes. Local pressures and total forces are measured.	$C_S = 2 - 4$; Maximum local pressures between 300 kPa and 600 kPa.

Continued

Table 2.3: Overview of wave impact studies and essential results.

Authors	Model, Assumptions	Pressures, Forces
Chan et al. (1991)	Model tests of focused breaking waves on a fixed cylinder with diameter $D = 0.216$m, water depth $d = 0.8$m, $eta_{max} = 0.185$m, wave length $L = 2.48$m, period $T = 1.28$s. Simultaneous measurement at 8 pressure locations.	Triangular pressure distribution with averaged peaks $= 30 \ \rho c^2$ and standard deviation of ± 20 at $z/eta_{max} = 0.94$. Slamming characterized by pressures $> 3 \ \rho c^2$.
Zhou et al. (1991)	Experiments on breaking waves in a 30m long wave flume with 0.6m water depth. The cylinder diameter is 0.12 m and the plunging waves are generated by frequency modulated wave packets. Pressures are measured at five positions between 2.5 cm and 17.5 cm above the still water level.	Impact area spreads $\pm 20°$ to the side with pressures between 4-13 ρc^2 and rise times $<$ 0.002 wave period T. Suggests a vertical region of impact around $\Delta z/L = 0.03 \approx$ cylinder radius in this case.
Chan et al. (1995)	Laboratory tests with a repeated and equally generated plunging breaker are conducted in a 30m long wave flume with 0.8m water depth. The wave is 2.48m long, has a period of 1.21s, a wave speed of 1.93m/s, and the maximum crest elevation is 0.185m. Impact loads are classified into five stages for various positions of the cylinder with regard to the breaking location.	Peak pressures between 16 to 47 ρc^2 with rise times $= 0.001$ T are observed for slightly curled wave fronts. Slamming pressures $> 3 \ \rho c^2$ range between $z/eta_{max} = 0.81$ - 1.08. Triangular pressure distributions are observed for stages 1 - 4.
Suyuthi and Haver (2009)	Model test on a tension leg platform with circular columns and 3h extreme-storm conditions for the North-Sea in a wave basin. Impact forces due to irregular waves are measured by force panels.	C_S values around 10 are reported on the basis of corrected water particle velocities by Clauss (2010).
Arntsen et al. (2011)	Model tests with breaking waves for a fixed cylinder on a shoal with diameter $D = 8.6$ cm. Local forces are measured by ring force transducers.	Highest wave load is $C_S = 4.27$ observed at $z/eta_{max} = 0.74$.
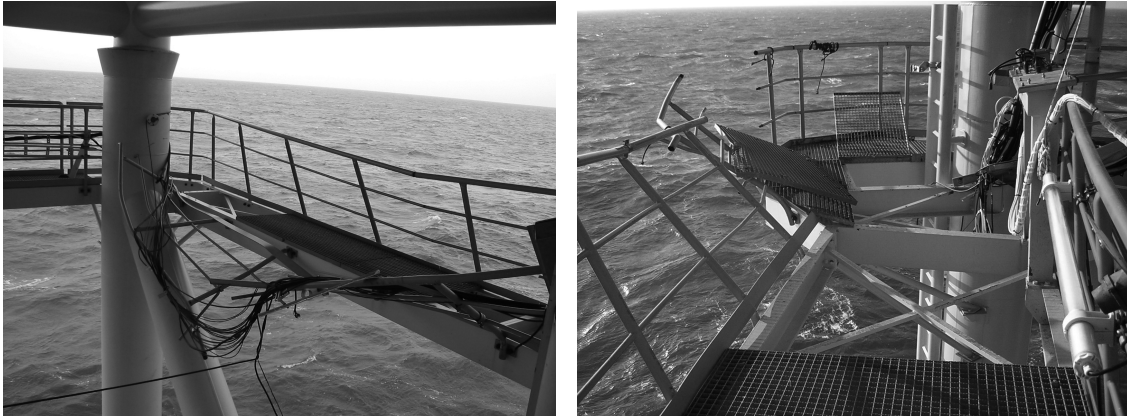
Figure 2.13: Damages at FINO I on the front- (left) and on the rear-side (right) due to the former mentioned breaking waves in November 2006. (Source: BSH)

2.4.2   Recommended practice & remaining questions

Basically, two models are recommended by international guidelines for dynamic load analysis of slamming loads on tubular members. The first one is the analytical model of Wienke and Oumeraci (2005), i.e. recommended by GL (2005), ABS (2011), and IEC (2009) among further guidelines referring to the listed standards. As already pointed out, the maximum load of the time variant force coefficient is $C_S = 2\pi$. The height of the impact area is defined by the empirically chosen curling factor up to $0.5\eta_{max}$ for plunging breakers. The width of the impact area is equal to the diameter and impact pressures are averaged across the full width of the cylinder.

The second model is the one proposed by Campbell and Weynberg (1980) and recommended by DNV (2007), which provides time variant coefficients as well, initially starting with $C_S = 5.15$. Local impact pressures are assumed to symmetrically spread 22.5° towards both sides of the cylinder's span, which leads to the width of the constantly distributed pressures. It is further recommended that the vertical range of the impact area is set to 20% of the breaking wave height. The impact load is defined until the cylinder is fully submerged, in contrast to the shorter and more suitable duration defined by Wienke and Oumeraci (2005).

Other standards like API give recommendations in terms of quasi-static load calculations, i.e. for horizontal slender pipes, for the flow force given by equation 2.2 in combination with published slamming coefficients.

Fluid forces depend on the squared velocity as described in the beginning of this chapter. Since the highest velocities are anticipated near the breaking wave crest, maximum forces should appear near $z/\eta_{max}{=}1$. However, the overview in table 2.3 as well as further descriptions in the previous sections indicate

intensive loads at relative heights $z/\eta_{max} \geq 0.7$ for plunging breakers. This might imply that the mechanism of impact forces due to breaking waves differs from the often assumed horizontally layered velocity distribution, which is sometimes used to account for the non-constant line force within the impact area. The required velocity distribution of the impacting wave crest is recommended to be estimated by stream function theory for spilling and plunging breakers, due to the lack of breaking wave kinematics from theory. For plunging breakers the application of wave theories is limited to the region below the still water level (DIN (2009)).

Therefore, question-marks remains for the velocity distribution above the still water level and consequently for detailed slamming loads in this region, too. Conservative loads are generally applied with relatively large curling factors and high slamming coefficients. Large curling factors imply wide areas of averaged pressures and further details on the temporal and spatial pressure development might be useful to avoid damages as documented at FINO I (Fig. 2.13). Furthermore, detailed information about the locations and dimensions of impact forces provides potential for load reduction by means of adapted curling factors.

These aspects give the motivation for the objectives listed in chapter 1.2 on the basis of physical and numerical modeling, which is underlined by recent recommendations in ABS (2011):

"The most important research area includes models for strongly nonlinear waves as well as for the resulting slamming loads on structures. CFD itself or in combination with other methods appears to be a very promising path...

A significant amount of work is still needed for... validating against qualified experimental data. This is a very challenging task partially because of the difficulties in having a consistent interpretation of wave slamming measurements."

3 Physical model of breaking waves

Physical model tests with breaking waves have significantly improved since the 80's due to the rapidly developing measurement devices. The duration of wave slamming lasts for about 10 to several hundred milliseconds, which is why it is difficult to consistently measure slamming pressures. As already mentioned in chapter 2, reports on slamming pressure experiments show significant scattering due to different setups and unavoidable inherent uncertainties. Relatively small pressure cells and high sampling frequencies are necessary to record the rapid and highly variable pressures in the slamming area. Pressure cells with small dimensions, low latency to pressure changes, and high natural frequencies are generally available nowadays. In addition, the complex flow field of breaking waves is a key factor as input parameter to numerical methods and analytical approaches, as described in chapter 2.3. However, the measurement of the flow field remains a very challenging task for both, small and large scale experiments. On the one hand small scale experiments are more influenced by air bubbles than large scale tests. On the other hand, non-intrusive optical measurement methods are applicable and able to cover a relatively large cross-section of the flow, which is difficult to realize for large scale experiments. Furthermore, scale effects are more or less always present unless prototype conditions are tested due to the proportions and the balance of forces. Since free surface tests are dominated by the ratio of inertia and gravitational forces (Froude law) in comparison to frictional forces, large scale physical model tests are realized for this study and performed for the investigation of loads and fluid kinematics of breaking waves on a tripod structure.

3.1 Experimental setup

Fig. 3.1 illustrates the cross-section of the large scale experiments (1:12) with the tripod model in the large wave flume ("Großer Wellenkanal" - GWK), at the Coastal Research Center (FZK) in Hanover, Germany. The wave flume is 7m deep, 5m wide, and 330m long. A trapezoid sand profile is integrated in the test setup for model tests on scour development around the tripod structure (Stahlmann and Schlurmann
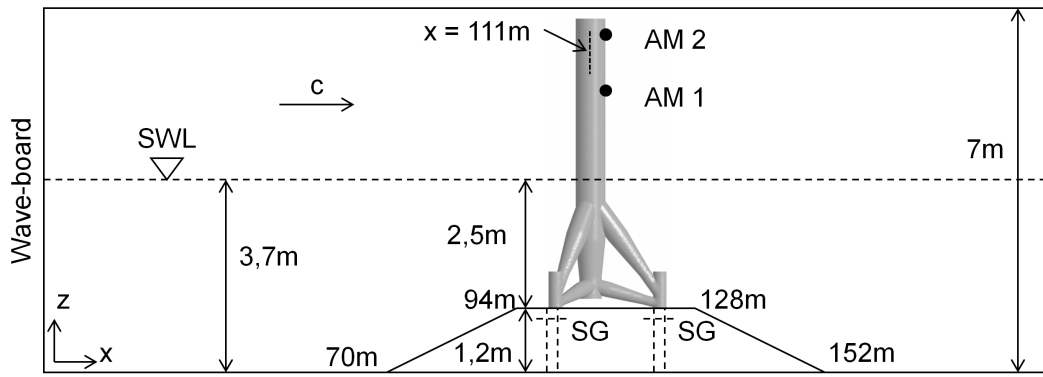
Figure 3.1: Cross-section of the experimental setup with still water level (SWL), acceleration meter (AM), and strain gauges (SG).
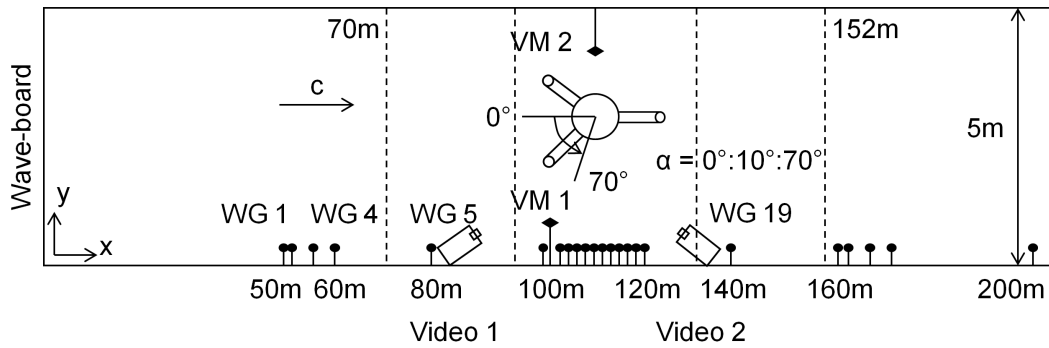
Figure 3.2: Plane-view of the experimental setup with wave gauges (WG), velocity meters (VM), Video cameras, and angle of rotation.
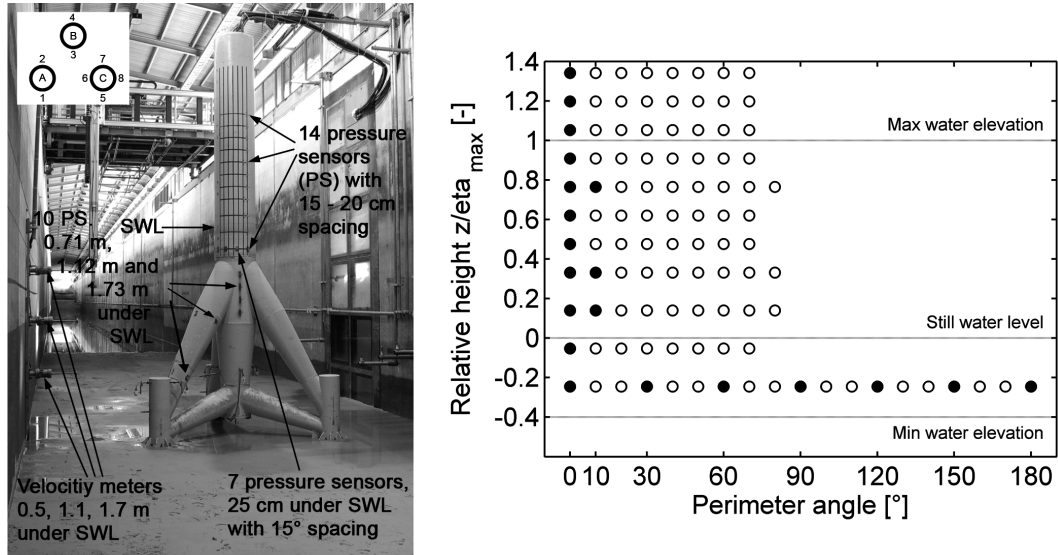
Figure 3.3: Left, large scale tripod structure (1:12) with water pressure sensors (PS), strain gauges (SG), acceleration meters (AM), and velocity meters on a level with the tripod main column. Right, positions of water pressure sensors in the rotating section of the tripod main column.

(2012)). After 70m with a constant water depth of 3.7m the sand profile increases along 24m to a level height of 1.2m, which corresponds to a slope of 1:20. Therefore, the water depth is 2.5m above the 34m long horizontal sand profile, whereafter the slope on the rear side decreases with 1:20 until 152m behind the zero position of the wave maker. 24 wave gauges with 0.7m distance to the southern channel wall are installed along the wave flume to capture the water surface elevation and the development of the breaking waves, which is why the horizontal spacing of the wave gauges becomes smaller in the near field of the tripod and partly reduces down to 0.25m (Fig. 3.2). Furthermore, six electromagnetic velocity meters are installed to measure the horizontal (x-direction) and vertical (z-direction) water velocities in a 2D plane parallel to the channel wall. Three current meters are located 101m behind the wave maker (6m behind the slope) with 0.6m distance to the southern wall. The other three current meters are positioned on a level with the main column of the tripod at 111m with 0.4m spacing to the northern wall of the flume (Fig. 3.2). At both locations the velocity meters are positioned 0.5, 1.1, and 1.7m below the still water level (Fig. 3.3, left) and are submerged in the water at all times during the experiments. Two video cameras are installed at the southern wall of the wave flume (Fig. 3.2) to capture the wave impact with 200 frames per second. They are mounted in front of, next to, behind, and above the main column to record the repeated breaker types from different view points.

The main column of the tripod has a diameter of 0.5m with an upper (yellow) rotating section and 20 installed pressure sensors. Fig. 3.3 (right) illustrates the locations of the 20 instrumented pressure sensors for the 0° angle position by the filled circles. The upper section of the tripod is shifted from 0° up to 70° angles by 10° intervals. A wide range of measuring positions along the cylinder's span as well as along the perimeter is covered in this way, which results in the plotted grid shown in Fig. 3.3. Ten additional pressure sensors are instrumented in the stationary lower (gray) part of the structure and indicated in Fig. 3.3 (left). Three sensors record the pressures approximately 1.73m below the still water level (SWL) at the upper brace "A" according to Fig. 3.3. Likewise, three other sensors are installed 1.12m below the SWL and the remaining four pressure sensors are vertically aligned at the upper part of the main column, 0.56, 0.71, 0.86, and 1.01m below SWL. In addition to the pressure sensors, two three-dimensional acceleration meters are installed in the main column 1.18m and 2m above SWL, which recognize the onset and intensity of the tripod's movement. The tripod is fixed on a steel pipe substructure, which is submerged in the sand and connects the three legs of the tripod with the bottom of the wave flume (see Fig. 6.12 for a perspective view). Eight strain gauges are positioned at the three steel pipes A, B, and C as sketched in Fig. 3.3 (left). They are
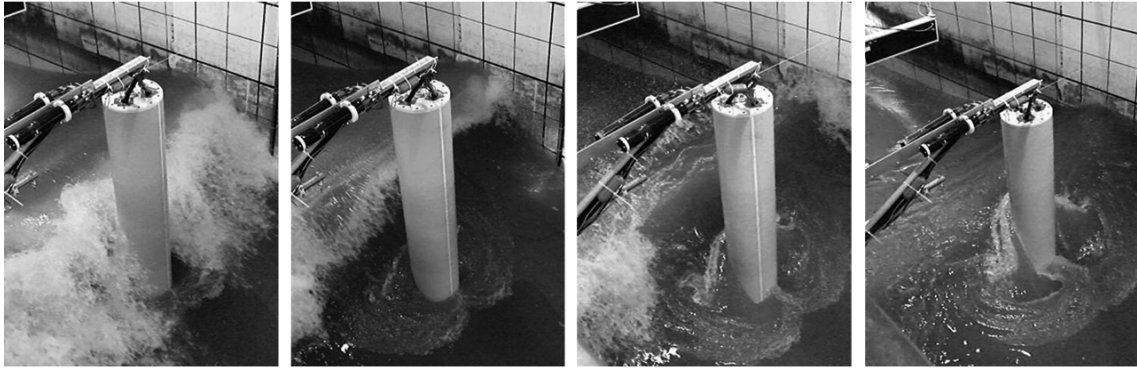
Figure 3.4: Snapshots of breaking wave types 1 to 4 from left to right.

applied to estimate time dependent total loads on the tripod structure due to their position right below the bolted joint connection of the tripod and the substructure.

The signals of the wave gauges, velocity meters, and the wave board consist of harmonic components without discontinuities and are sampled with 100 Hz. In contrast to that the time series of the acceleration meters and especially the pressure sensors in the slamming area are subject to jumps and discontinuities due to the wave impact. Therefore, the strain gauges and acceleration meters were sampled with 600 Hz and the pressure sensors with 10 kHz. Due to the 16-bit sampling i.e. the resolution of the wave gauges is below 0.0001m and of the 10bar pressure sensors below 0.0003bar.

3.2   Test program

Four different types of wave breaking with various distances to the main column of the tripod are tested in the experiments and described in the following. Fig. 3.4 shows snapshots of the four cases 1-4 from left to the right. All breaking waves are generated by focusing wave packets (Sparboom et al. (2005)) with a characteristic wave height of 0.8m and a peak period of 4 seconds, which results in four different breakers with instantaneous pairs of breaker heights H_B and periods T_B shown in Fig. 3.6. The characteristic wave parameters are kept constant for all test cases and only the focusing point of the wave packet is shifted from 111m, 115m, 119.5 m to 132m for the load cases 1-4, respectively. However, due to shallow water effects and the slope of the sand trapezoid in front of the tripod the above given focusing point does not match the location of wave breaking. The onset of the four wave breaking locations is not clearly distinguishable in the wave gauge signals, and is therefore estimated by video records and visual observations during the experiments.

Table 3.1: *List of experiments with two braces directed to the front-side (position 1).*

Rotation	Load case 1	Load case 2	Load case 3	Load case 4
0°	3	5	7	2
10°	3	4	3	2
20°	3	4	3	2
30°	4	3	3	2
40°	3	3	3	2
50°	3	3	4	2
60°	3	3	3	2
70°	3	3	3	2
Sum:	**25**	**28**	**29**	**16**

For load case 1, wave breaking sets in 6m in front of the tripod main column. The wave is a broken wave with a foamy wave front due to the mixture of entrapped air and the mass of water, similar to stage V described by Chan et al. (1995). Load case 2 is generated with a wave breaking position starting 4m in front of the main column. The wave has a concave wave front with jet formation or curling breaker tongue, which hits the cylinder at higher elevations before falling downward into the water; similar to Stage III+IV according to Chan et al. (1995). Load case 3 starts breaking right in front of the tripod main column with a partly vertical wave front at the crest and corresponds to stage II by Chan et al. (1995). As can be seen in the two pictures in the middle of Fig. 3.4 the wave breaking is not exactly two-dimensional. This is mainly reasoned by the sand slope of the experimental setup and affects the pressure development along the perimeter in the region of the wave impact. Further details on this matter will be given in chapter 6.1.2 in conjunction with the onset of impulsive pressures. Load case 4 is becoming instable at the main column and thus breaking behind the structure. This represents the quasi-static load component without slamming loads, however, with a non-breaking wave shape at the cylinder as similar as possible to the combined wave loads.

In total, $25 + 28 + 29 + 16 = 98$ tests are performed with two of the three tripod legs pointing in the direction of the wave maker, as shown in Fig. 3.2. Table 3.1 lists the number of experiments for each load case and for each angle of the rotating tripod section. The highest number of tests is performed for the zero angle position, which represents the vertical alignment of pressure sensors in the cylinder's span. Load case 4 (no impact) is repeated only two times due to the very small deviations of the pressure time series at all levels (Chapter 6), while the other load cases are tested at least three times.
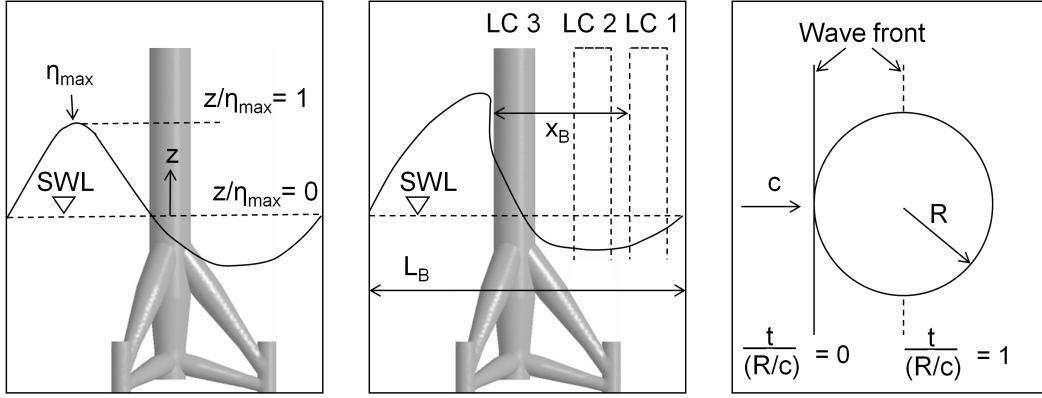
Figure 3.5: Definition of relative height z/η_{max}, impact duration t/T with $T=R/c$, and breaker distance x_B/L_B.

3.3   Definition of dimensionless parameters

Several dimensionless parameters are introduced at this point and will be used throughout the following chapters for illustration purposes as well as for comparison to other studies from literature.

Fig. 3.5 (left) shows the definition sketch of the *relative height z/η_{max}* along the cylinder's span. The vertical coordinate z is zero at the still water level and positive coordinates point upwards, while negative coordinates describe a position below the SWL. z is referenced by the maximum surface elevation η_{max} and thus, z/η_{max} equals one on a level with the wave crest and zero at the SWL. Fig. 3.6 shows case-averaged wave gauge records and time dependent standard deviations of the tested breaking waves at the front side of the main column. Each load case is averaged over the number of tests listed in the corresponding column in table 3.1. Small differences are observed for the maximum water surface elevations 1.01m, 1.02m, 1.05m and 1.07m for load cases 1-4, respectively. Since the mean value of 1.04m has a maximum variation of 3% in regard to the individual values of η_{max}, the mean value is taken as reference for all load cases. This simplifies the handling of the pressure sensors plotted in Fig. 3.3, due to the fixed relative positions for all load cases. Likewise, the minimum values of the wave troughs are close to each other (-0.41m, -0.43m, -0.44m, and -0.41m) and therefore averaged to -0.42m, which leads to a breaking wave height $\overline{H}_B = 1.46$m.

Also seen in Fig. 3.6, the four snapshots of the transient wave differ up to 4.64s/3.84s = 20% from each other at the cylinder front. This is reasoned by the wave packets with various focussing points, which results in a transient wave with continuously
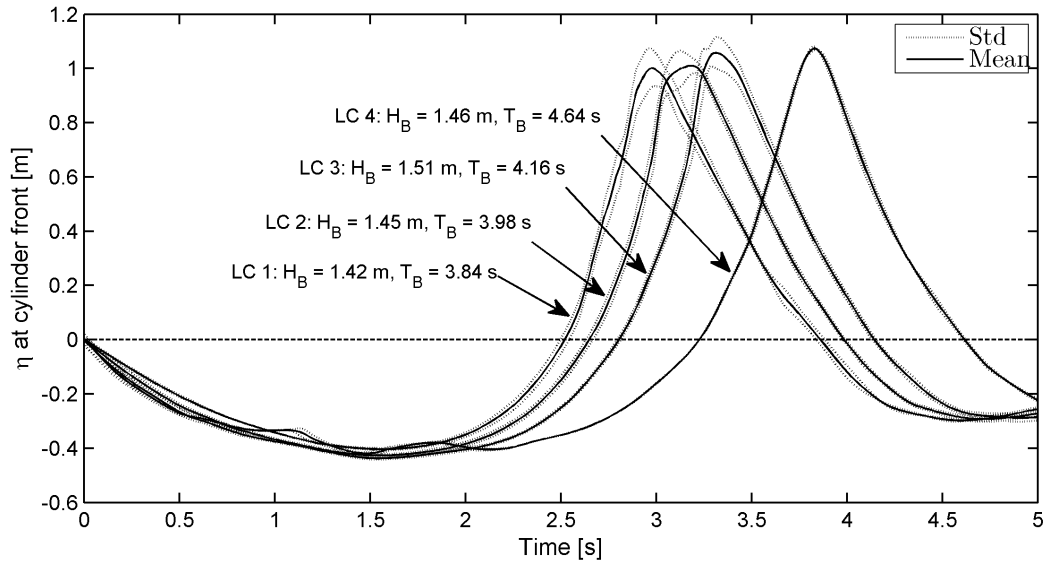
Figure 3.6: Breaker heights H_B and periods T_B of the four tested waves on a level with the front span of the cylinder.

changing wave period (and height) during wave propagation. Keeping the effect of the slope and further laboratory effects in mind, the wave periods of the three breaking waves are similar at the above mentioned locations for the onset of breaking. They are averaged in the same way as the wave heights, which leads to a mean value of $\overline{T_B} = 4.08$s with maximum differences of roughly 2% taken from:

- LC 1, breaking 6m in front of the cylinder front: T=3.99s at wave gauge 7.

- LC 2, breaking 4m in front of the cylinder front: T=4.09s at wave gauge 9.

- LC 3, breaking 0m in front of the cylinder front: T=4.16s at wave gauge 14.

There is no direct measure of the *wave length* when dealing with time series of local wave gauges. The wave length is used according to the sketch in the middle of Fig. 3.5 for the relative distance x_B/L_B of the breaking location to the front side of the cylinder. It is iteratively calculated for $L_B = 18.16$m by the dispersion relation with wave length L, water depth d, gravitation g, and the mean period $\overline{T}_B$:

$$L = \frac{g\,T^2}{2\pi}\,\tanh\left(\frac{2\pi d}{L}\right) = \frac{9.81 \cdot 4.08^2}{2\pi}\,\tanh\left(\frac{2\pi \cdot 2.5}{L}\right) \qquad (3.1)$$

The result is checked for plausibility within the capabilities of the surrounding wave gauges. For example, load case 3 is directly breaking at the cylinder front after 78.24s. The backward zero crossing of the wave crest is passing between wave gauges

8 and 9 at the same time and the zero crossing of the preceding trough shortly behind wave gauge 18, which leads to a distance longer than 13.5m and significantly shorter than 33.5m.

The tripod is fixed in the physical model, which is why the different breaking locations for one wave need to be generated by the shifting focusing points. This method is not as exact as a shifting tripod in combination with only one repeated wave, like in a numerical model. Small differences in the wave height and period are present and difficult to avoid in large scale experiments. With reference to the definition in Fig. 3.5, the *relative breaking distances* x_B/L_B are $6/18.16 = 0.33$ for LC 1, $4/18.16 = 0.22$ for LC 2, and 0 for LC 3.

The geometrical *wave steepness* H/L at the instant of induced breaking comes to a value of $1.46/18.16 = 1/12.44 = 0.08$.

For non-focusing waves the *phase velocity* is equal to the wave length divided by the period. Assuming that the dispersion relation gives the actual wave length for these experiments, the celerity could be calculated to $18.16m/4.08s = 4.45m/s$ in this case. Due to the focusing wave packet and the shallow water effects especially caused by the sand slope, the estimated wave length probably differs from the real one. Furthermore, not the velocity of the whole wave but the water velocity of the wave crest just before wave breaking is of special interest in regard to the slamming problem, since this water mass contributes the impulsive forces. Video observations as well as averaged wave gauge records up to 10.75m in front of the main column are analyzed to estimate the developing crest velocities. Based on the outcome 4.8m/s for LC 1, 4.8m/s for LC 2, and 4.82m/s for LC 3, the reference celerity is set to 4.8m/s.

The *reference pressure* by means of the stagnation pressure is $p_{ref} = \rho c^2 = 23\text{kN/m}^2$ and the *reference line force* on the main column with a diameter D of 0.5m results in $f_{ref} = D\rho c^2 = 11.5\text{kN/m}$.

3.4   Scale effects

Scaled models are inevitably affected by scale effects. One aspect is the influence of surface tension, because the wave celerity depends on the surface tension and it introduces a wave damping effect. According to Le Mehaute (1969) these effects need to be taken into account for water depths smaller than 2 cm and up to wave periods of 0.35s. The shortest waves of the focusing wave packets described in section
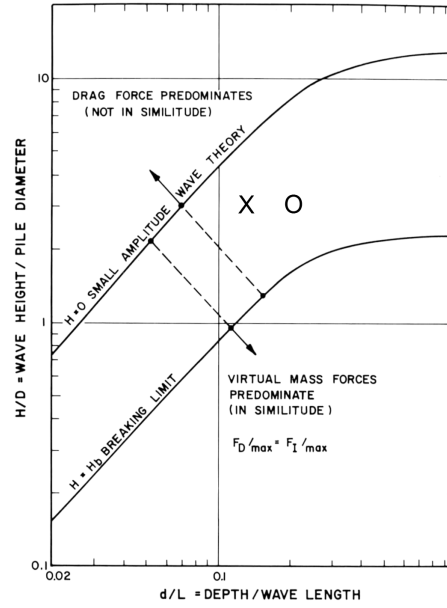
Figure 3.7: Category of similitude for waves predominated by drag or inertia forces plotted over d/L and H/D (Le Mehaute (1969)).

3.2 possess a period of 2.3s and therefore surface tension is of minor importance; at least apart from the wave impact.

The similitude of inertia and drag forces is of major importance in this section, since this work deals with wave loads on a structure scaled by 1:12. Generally, the significance of the these two forces is distinguished by the ratio of the pile diameter D by wave length L, which is $D/L = 0.5/18.16 = 0.0275$ for the above mentioned cases. Formally, 0.0275 is smaller than the approximate boundary value of 0.05, which classifies the test cylinder as small and indicates the importance of drag and inertia forces. Both force components on small piles are commonly estimated by the Morison formula given by the first two terms in equation 2.14 on page 34. The coefficients C_D and C_M are time dependent functions for non-uniform flow as induced by waves and obtained experimentally. With regard to the drag component, similitude is only possible for uniform flow with a Reynolds number (Re) higher than $2 * 10^5$ (Le Mehaute (1969)), while inertia forces are less sensitive to scale effects. On the one side $Re = 2 * 10^5$ is exceeded as soon as the water velocity is higher than ± 0.1m/s due to the large scale. On the other side the flow under waves is non-stationary and therefore prototype conditions are needed in theory to satisfactorily account for the drag contribution. Although shear stresses are more or less present at the structure's surface during wave breaking, impact loads are clearly dominated by inertia forces, which will be pointed out in the following chapters.

Le Mehaute (1969) illustrates this aspect in figure 3.7 by the two lines representing inertia forces equal to the drag forces based on linear wave theory, whereby the abscissa denotes the relation d/L and the ordinate H/D. Drag forces predominate cases with small amplitudes while the virtual mass forces contribute the major part of the loads for waves close to and during breaking. The two marks indicate the regime of the test waves for 2.5 (x-marker) and 3.7m (o-marker) water depth. Both cases are roughly positioned in the middle of the boundaries, whereas the x-marker represents the regime at the tripod and is therefore more substantial.

3.5   Summary

Chapter 3 describes the physical model including dimensions of the wave flume and the scaled structure (1:12), the applied sensors and their positions as well as benefit of the large wave flume regarding scaling effects. The useage of the rotational tripod main column for the spatial pressure measurement is illustrated, which is further discussed in section 4.1 in combination with the reproduction of the tests. Furthermore, the test program and the number of waves for each orientation of the main column and the type of wave breaking is given in table 3.1. Parameters like (transient) wave period, wave length, wave breaking distance in front of the main column, wave steepness, phase velocity, and reference pressure used for the normalized illustration of test data and results are introduced and derived in section 3.3 for further reference in this work.

4 Analysis part I: Data processing and wave-structure interaction

4.1 Synchronization and reproduction of tests

In order to measure the spatial and temporal distribution of the wave impact the central cylinder is rotated along the vertical axis in 10° steps. The rotational section provides a relatively high resolution of measuring points using a limited number of pressure sensors. Prerequisite for this approach is a good reproducibility of the breaking wave forms as the individual experiments are plotted and analyzed in one combined grid. The movement of the wave maker in conjunction with the constant water level is one parameter to cross-check the wave shapes as well as all measurements at the structure. The variance of the measurements, i.e. wave gauges and velocity meters, increases with decreasing distance to the onset of wave breaking. The standard deviation of the water level elevation is of special interest on a level with the front of the cylinder. At this position the breaking wave interacts with the structure, which is why this location is the most important one for checking the reproducibility of the test series.

The tested transient waves are continuously changing along the wave channel and have an averaged period of $\overline{T}_B = 4.08$s and $\overline{H}_B = 1.46$m (see section 3.3). Fig. 3.6 shows the four different waves and the corresponding standard deviations for each point of time. The maximum standard deviations are 0.075m for LC 1 with an average positive crest elevation $\overline{\eta}_{max} = 1.01$m, 0.056m for LC 2 with $\overline{\eta}_{max} = 1.02$m, and 0.06m for LC 3 with $\overline{\eta}_{max} = 1.05$m. LC 4 is the non-breaking wave with $\overline{\eta}_{max} = 1.07$m and maximum standard deviation less than one centimeter, which is practically zero. The deviations aside the wave crests are very small for all test cases and marginally vary after the passage of the wave crest due to negligible laboratory effects. They are caused by small reflections at the structure, which spread concentrically from the cylinder in the direction of the wave maker after the passage of the wave. At the wave crests the signals vary with differences of 5-7%, which are probably caused by variations in the exact position of the onset of wave breaking and by air inclusions. A variation up to 7% is an acceptable number in the
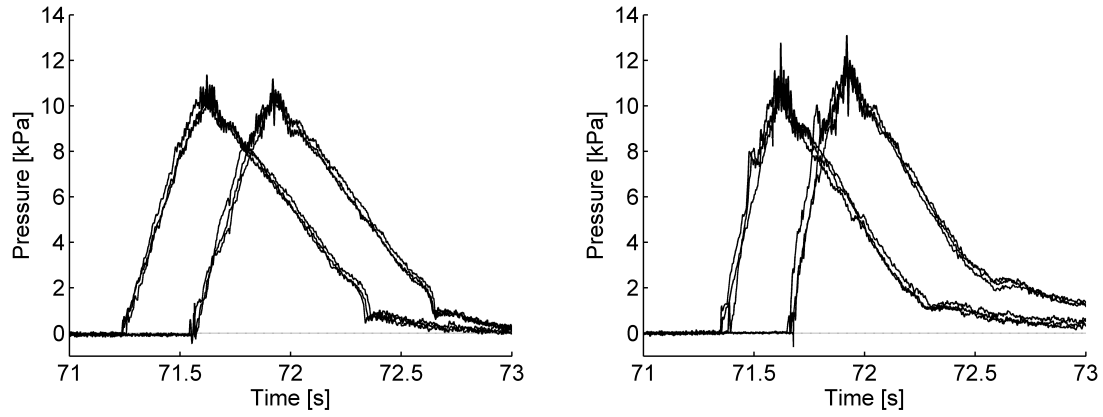
Figure 4.1: Similarity of hydrodynamic pressures at height $z = 0.14 * \eta_{max}$ (left) and $z = 0.33 * \eta_{max}$ (right) for different test waves.

general context of engineering purposes. In this case, 7% is a rather high number and this aspect must be kept in mind for analyzing the slamming wave fronts and for a critical discussion of the results later on.

The problem of wave gauge records influenced by air entrainment is excluded for the time series of lower positioned hydrodynamic pressure measurements at the tripod. Fig. 4.1 (left) shows two sets of pressure signals with a 300 ms shift for better illustration purposes. Each set represents three experiments with identically generated waves, but with different angle positions of the rotational tripod section. The sensors are located at the relative height 0.14 according to the grid in Fig. 3.3. Likewise, Fig. 4.1 (right) illustrates two sets of pressure records at a relative height 0.33. The similar time series of the pressure signals indicate the good reproducibility of the breaking waves directly at the structure. The exemplarily plotted signals are taken from load case 2 with a high amount of air entrainment at the crest. Rise time, peak shape as well as the distinctive drop seen at 72.3s in Fig. 4.1 (left & right) are reproduced by each test wave. Furthermore, the standard deviations of the pressure signals are very small even around the peak.

In addition to the evaluation of the reproducibility the well correlated signals during rise time and the peak characteristics are especially useful for the synchronization of the tests. Therefore the horizontally and next to each other arranged pressure sensors described in the prior paragraph are used to couple the experiments. Since the time series are in good agreement the data sets with angle positions between 0° and 70° are synchronized by the rise time and peaks of the overlapping sensor positions of the rotating section. For this purpose sensors at positions above the SWL are favorable compared to the pressure sensors located at the stationary part

of the tripod below SWL. As the wave front shape is the most important part of a
breaking wave the synchronization of the front should be as accurate as possible in
the order of milliseconds. Pressure sensors below SWL do not have a pointed peak,
but a curved crest instead. In contrast to that, the pressure signals plotted in Fig. 4.1
have a specific onset of the rise time, are close to the impact zone, and have a pointed
peak. This provides a far more accurate synchronization, better reconstruction and
correlation of the wave front. Theoretically, the two pressure sensors at the higher
position $z/\eta_{max} = 0.76$ (Fig. 3.3) offer even more accurate correlations, since they are
positioned inside the impact area. Practically, this location is strongly affected by air
bubbles in the wave crest and by additional oscillations of the structure. Therefore
time series at that location show considerable variations and small random peaks,
which are difficult to correlate.

Synchronization of the pressure signals exclusively on the basis of the wave gauges
leads to inaccurate results for the short-timed impulsive pressures. Firstly, this is
due to the air entrainment and slight changes of the wave front, which are barely
distinguishable in the range of the above given standard deviations. Secondly, the
lateral distance between the wave gauges and the main column is nearly 2m and
wave breaking is not ideally two-dimensional across the flume width. This includes
additional uncertainties for the synchronization based on wave gauges, since the
wave tongue might be different at the wave gauge and the main column.

Therefore, the wave gauges and pressure sensors located below the SWL are only
used for plausibility checks and the synchronization is performed with the pressure
sensors at the relative heights 0.14 and 0.33 above the SWL. Subsequently, the
measuring positions are combined to one grid (Fig. 3.3) for the investigation of the
spatial and time dependent pressure development around the main column.

4.2   Signal denoising

Recordings are generally overlapped by noise due to the electronic setup with am-
plifiers and measurement devices. Typical noise is seen in Fig. 4.2 (right), which
is high frequent and more or less constant in amplitude. Ideally, the filtering iso-
lates the signal and removes the noise without significant phase shifts and cut-offs
of the signal. However, this is not straight forward for the slamming signals with
sharp peaks and sudden pressure onsets, since inadequate filters strongly distort the
signal. There are several possibilities to filter the measurements, which differ in
performance and quality. The observed pros and cons with regard to the slamming
tests are briefly described for some methods.

	$i-4$	$i-3$	$i-2$	$i-1$	i	$i+1$	$i+2$	$i+3$	$i+4$	
1st Ord.:				[1	2	1]				/4
2nd Ord.:			[−1	4	10	4	−1]			/16
3rd Ord.:		[1	−6	15	44	15	−6	1]		/64
4th Ord.:	[−1	8	−28	56	186	56	−28	8	−1]	/256

Table 4.1: Weighted moving averages up to the forth order for sample position "i".

Weighted moving average is a fast method and takes a specified number of sample points ahead and after a location into account for the weighted average. Table 4.1 shows smoothing coefficients for moving averages up to the forth order, which were used for the signal processing. The method is satisfactory for the continuous signals, like the wave gauges and velocity meters. However, the weighted moving average is less useful for the slamming pressure signals with a sharp rise time and a pointed peak, since both characteristics are significantly modified by the averages.

Similar problems are observed for low-pass and band-stop filter as plotted in Fig. 4.2, for example. In addition to the reduced peak values for the band-stop filtering with f_{stop} = 47-53 Hz, oscillations are seen before the sharply increasing peak as well as amplified oscillations after the peak during the dampening of the signal. The additional oscillations correspond to the cut-off band-stop frequencies and a similar effect is observed for low-pass filter with various f_{pass} and f_{stop} frequencies. For example, Butterworth-type low-pass filtering with f_{pass} = 50 Hz and f_{stop} = 55 Hz reduces the peak value by nearly 10%. The difference decreases with increasing frequencies and high-frequent noise can be filtered with butterworth $f_{pass} > 150$ Hz and $f_{stop} > 200$ Hz combinations.

Both, the noise around 50 Hz due to the system voltage as well as the high-frequent noise can be filtered without phase shifts of the signal or truncated peaks by wavelet transformation. The method works very well for the continuous signals and for the records with impulsive characteristics, too. Therefore the wavelet transformation is performed to denoise the various signals of all tests.

In contrast to the Fourier transformation based on a linear combination of sine and cosine components the wavelet transformation uses a so called mother wavelet. A wavelet family is generated by the mother wavelet in combination with a scaling function, which translates and dilates the wavelet for correlations with the signal f(t). The similarity between the signal and the analyzing wavelet function is computed separately for different time intervals, resulting in a two dimensional representation. The definition of a continuous time wavelet transformation of f(t) is given by:

$$CWT_\psi\ f(a,b) = |a|^{-1/2} \int\limits_{-\infty}^{\infty} f(t)\ \psi^* \left(\frac{t-b}{a}\right) dt \qquad (4.1)$$
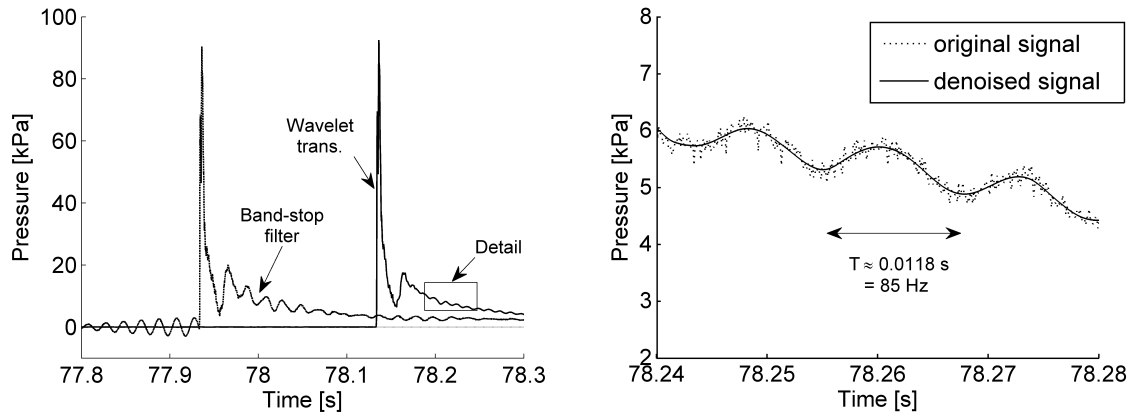
Figure 4.2: Comparison of impact pressures for LC 3 denoised by wavelet transformation and band-stop filter (left) as well as detail of high frequent noise (dotted line) and distinct structure oscillations (right).

Hereby a and b are real numbers with a $\neq$ 0 as dilating and translating coefficients, respectively, while the asterisk denotes a complex conjugate. The term is multiplied with $|a|^{-1/2}$ to normalize the energy so that the energy is the same for all scales. The CWT performs a multi-resolution analysis by contraction and dilatation of the wavelet functions and the discrete wavelet transform (DWT) uses filter banks for the construction of the multi-resolution time-frequency plane.

The choice of the wavelet is neither unique nor arbitrary and must satisfy the following two criteria (Schlurmann (2004)):

- The wavelet needs an adequate fast decay, i.e. a wave like shape, to discriminate between different frequencies in time-domain.

- The wavelet is not to be a standing wave and must integrate to zero.

In practice, the selected wavelet affects the frequency spectrum of the denoised signal due to its specific shape. Furthermore, the chosen wavelet should capture the transient spikes in the measured signal. There is no general method for the choice of the mother wavelet. One common approach is the correlation between the signal of interest and the denoised signal to distinguish between the level of quality for different wavelet types. Due to the strongly increasing pressure and the immediately following pointed peak the correlation method is less satisfying for the signals with slamming characteristic. This is because the whole time window of a signal section is taken into account for the coefficient of correlation and the onset of the rising pressure and the peak are not subject to special sensitivity. An analogous problem is observed for comparisons of the cumulated energy of the two
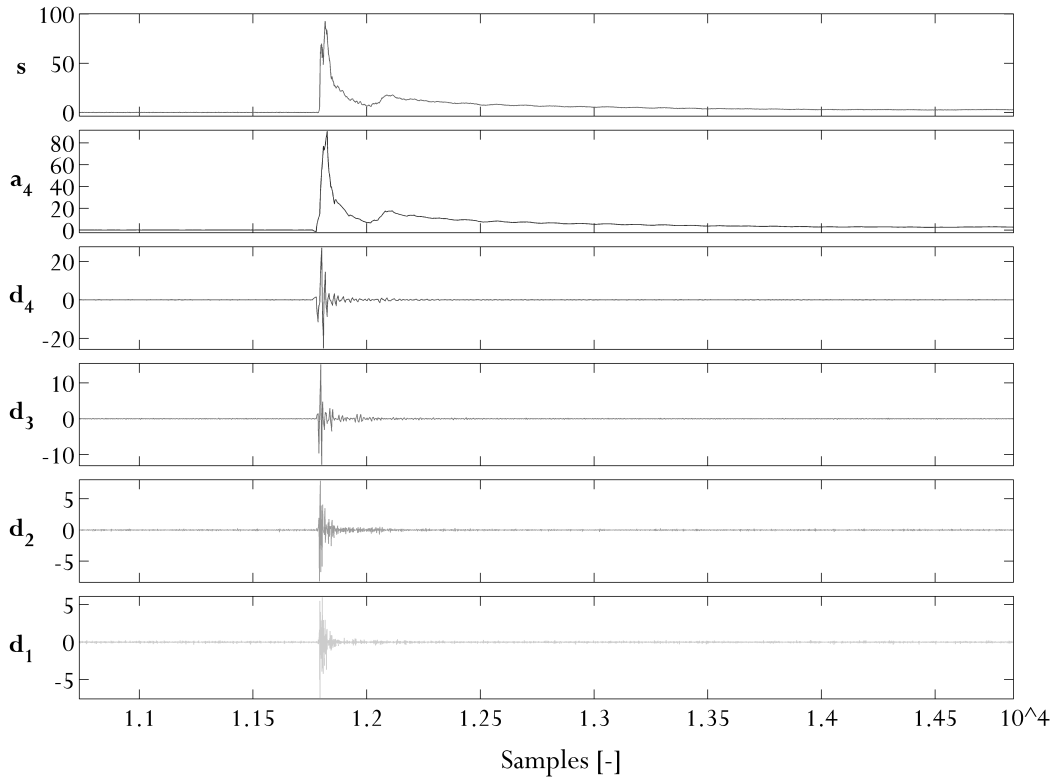
Figure 4.3: Decomposition of the "s" labeled impact pressure for LC 2 by "Daubechies 2" wavelet into average a_4 and details $d_1 - d_4$.

signals, which is a general method for the wavelet selection as well. Finally, the best results to denoise the previously described measurements is achieved by eyeball inspection and Fig. 4.4 shows the selected wavelet Daubechies 2 on the left. The best compromise between the noise filtering and the conservation of the peak as well as the rise time was observed for the Daubechies 2 and Daubechies 3 wavelets. These two wavelets decompose the signal into an almost constant distribution of coefficients plus the remarkable peaks along the samples (Fig. 4.3). Higher orders of the Daubechies-wavelets as well as other types, i.e. "Symlets" or "Coiflets", result in fuzzy distributions of the coefficients, which is not preferable in regard to the settings of the threshold levels.

As pointed out above the noise is almost constant in amplitude and frequency over time and represented by the small constant fluctuations of the decomposed details 1-4 in Fig. 4.3. Smoothing is performed by thresholding the wavelet coefficients and then returning the threshold code to the time domain. The thresholds of the four details are set by hard levels close to the small fluctuations. Since the original signal is down-sampled after each level of decomposition (wavelet tree) the thresholds of level one adjust the highest frequencies and the subsequent levels adjust for the stepwise lower frequencies. Thresholding for higher levels than four modifies the
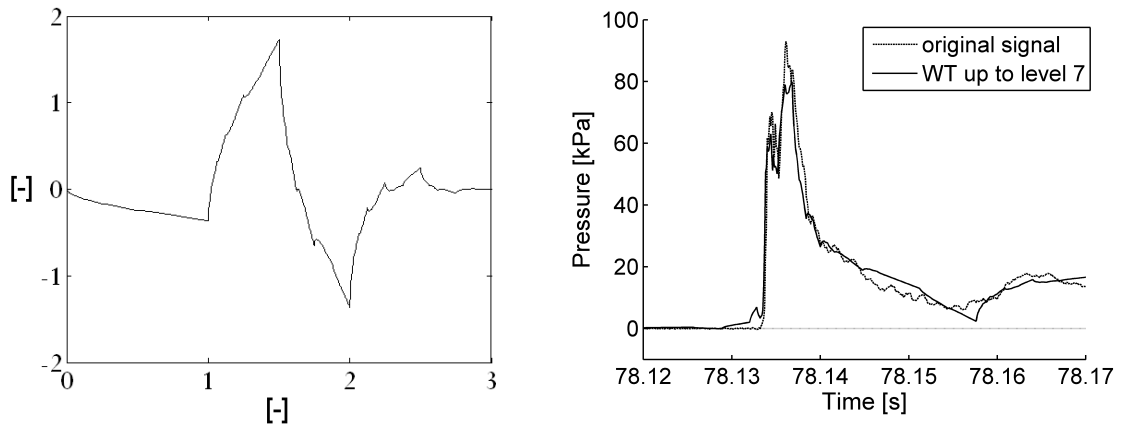
Figure 4.4: "Daubechies 2" wavelet function ψ (left) and signal composition of impact pressure up to level seven (right).

rise time of the impact pressures due to low frequency oscillations similar to the previously described band-stop filtering. Therefore the slamming measurements are denoised by decompositions up to level 4 with the Daubechies 2 wavelet.

4.3 Video analysis of wave-structure interaction

Fig. 4.5 - 4.7 show several snapshots of the breaking waves taken from the high-speed cameras before and behind the tripod as indicated in Fig. 3.2. They give an impression of the involved physics during wave breaking and support the analysis and interpretation of the measured data.

Load case 1 represents a broken wave and Fig. 4.5 a) shows the first contact of the wave front and the cylinder. This instant of time is used as reference for the subsequent snapshots and the turbulent, foamy water mass ahead of a relatively clam wave crest is clearly seen. Snapshot e) shows the same point of time from the rear side of the main column and further illustrates the front shape of the overturning wave tongue. Fig. 4.5 b) was captured 240 ms later (t/T=240/52=4.6) right before the wave crest reaches the cylinder. The foamy water mass passes the cylinder without intensive splashing, which is seen as well in snapshot f), and air bubbles are observed under the calm wave crest. Last mentioned probably originate from the turbulent water front as well as from enclosed air due to the overturning water. The wave tongue hits the back- and upward streaming flow of the preceding wave front/trough and takes in the air, which is then transported backwards into the wave crest. Fig. 4.5 g) shows the progressive interaction of the air-water mixture

Figure 4.5: Front- and rear-view of load case 1 with time shifts referenced to image a):
b) 240 ms (t/T=4.6), c) 390 ms (t/T=7.5), d) 1140 ms (t/T=22);
e) 0 ms (t/T=0), f) 150 ms (t/T=2.9), g) 250 ms (t/T=4.8), h) 500 ms (t/T=9.6).

Figure 4.6: Front- and rear-view of load case 2 with time shifts referenced to image a):
b) 150 ms (t/T=2.9), c) 180 ms (t/T=3.5), d) 360 ms (t/T=7);
e) -150 ms (t/T=-2.9), f) 0 ms (t/T=0), g) 100 ms (t/T=1.9), h) 175 ms (t/T=3.4).

with the cylinder, before the wave crest starts splashing up at the cylinder (snapshot c)). According to the experiments the splashing of broken waves is connected to the progressive motion of the wave crest, indicated by the wave run-up on the front side and the formation of horizontal spray beside the cylinder seen in snapshot h).

Load case 2 is characterized by the formation of a horizontal water jet at the wave crest due to a reduced wave breaking distance to the tripod and is documented in Fig. 4.6. The snapshots a) and f) show the point of time again, when the water reaches the cylinder. Air is only entrapped at the wave crest and not jet transported back and mixed into the water body under the wave crest in contrast to load case 1. Snapshot e) illustrates the steep wave front and the onset of wave breaking 150 ms prior (t/T=150/52=2.9) to the images a) and f). At this point of time the wave breaking is nearly two-dimensional, while three-dimensional effects are obviously present along the wave crest for the subsequent stages. This is mainly reasoned by the sand profile and the frameworks of measuring devices at the wall of the flume (Chapter 3.1). Even though the formation of the splash is nearly symmetric (Fig. 4.6 b), c), h)), this effect is present for load cases 2 as well as 3 and slightly varies from test to test. This affects the pressure development around the cylinder and will be investigated on the basis of the pressure time series in section 6.1.2. Snapshot b) is captured shortly after the wave crest hits the cylinder and shows the instantly developing splash. The impulsiveness of the impact is indicated by the rapid spreading of the splash in Fig. 4.6 b) and c). Both images have a time shift of 30 ms whereas the cylinder is immersed by t/T=0.58. The splash spreads approximately 0.3 to 0.4m during that time step, which results in a water velocity more than twice as high as the wave celerity of about 10 - 13m/s. Furthermore, the formation of the wake due to the former generated and redirected vortex is seen behind the cylinder in snapshot e) - h).

Load case 3 has no jet or wave tongue formation prior to the impact before the partly vertical wave front encounters the cylinder. Snapshots a) and f) in Fig. 4.7 illustrate the onset of the impact from both perspectives. Last mentioned shows the effect of three-dimensional wave breaking in the near field of the channel walls, while the wave front in the vicinity of the cylinder is predominately two-dimensional. Furthermore, an almost symmetric splashing can be seen along the cylinder's span in the following snapshots g) and h). Air entrainment is less intensive at the instant of slamming in comparison to the previously described load cases and only present in the upper part of the overturning water front. Air pockets are transported upwards by the wave run-up and observed at the cylinder's front, i.e. t/T=180/52=3.5 times of submergence after the impact (Fig. 4.7 c)). Another three-dimensional effect is
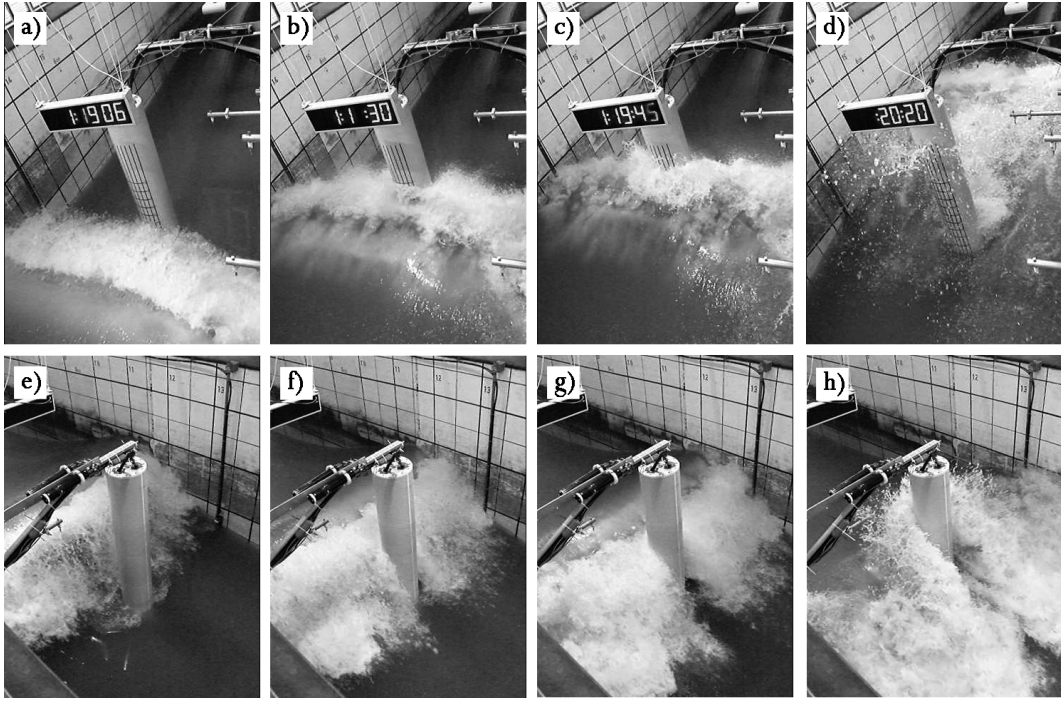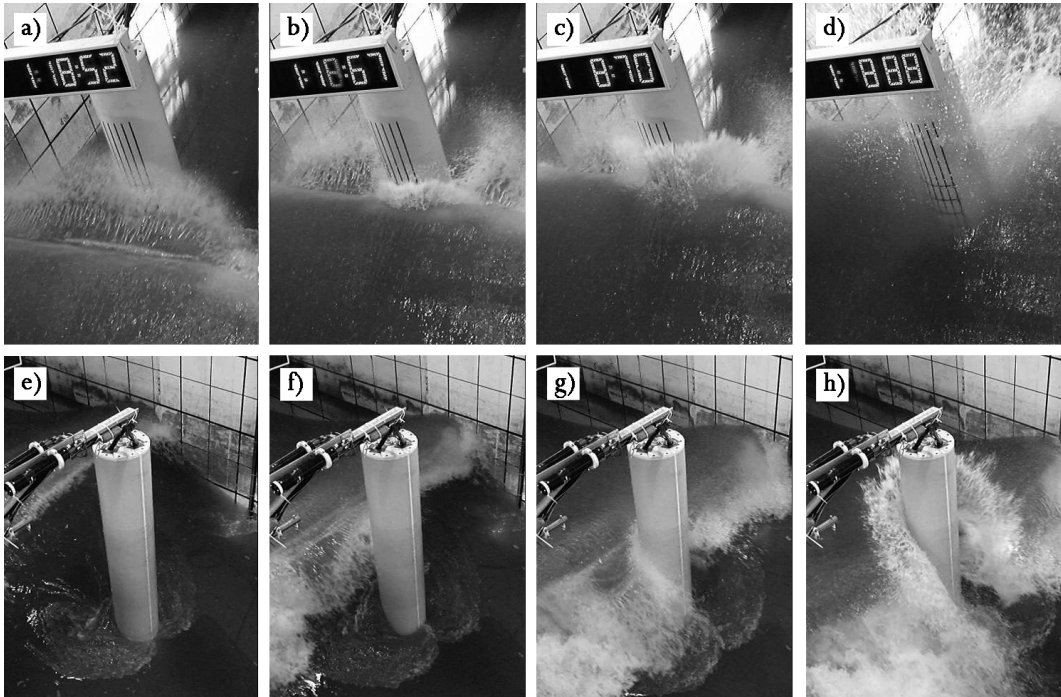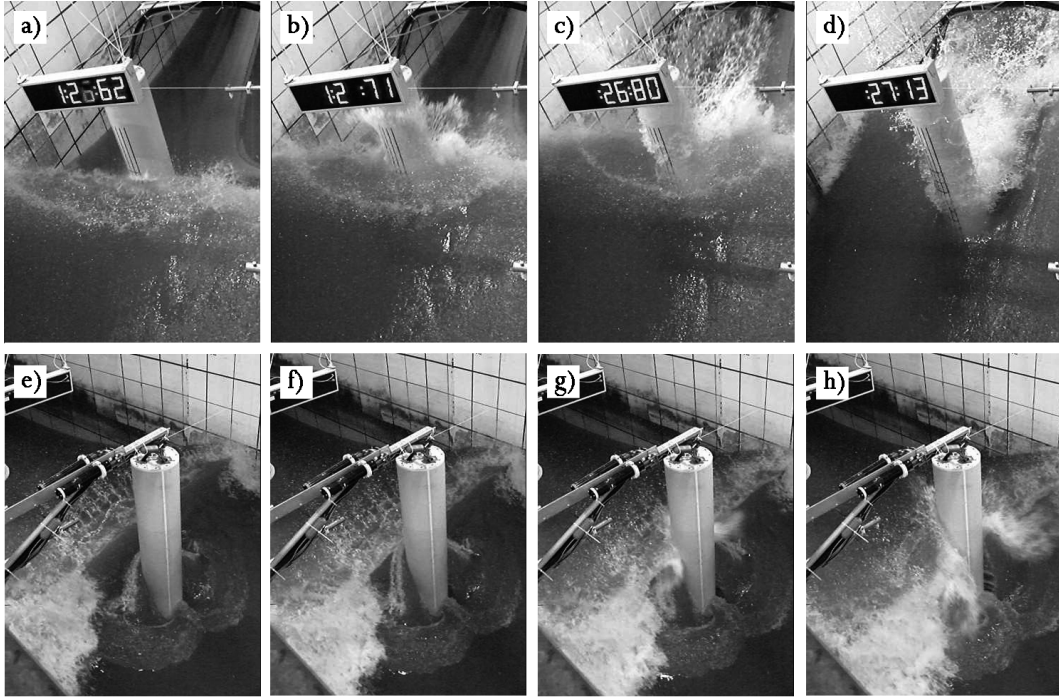
Figure 4.7: Front- and rear-view of load case 3 with time shifts referenced to image a):
b) 90 ms (t/T=1.7), c) 180 ms (t/T=3.5), d) 213 ms (t/T=4.1);
e) -50 ms (t/T=-1), f) 0 ms (t/T=0), g) 25 ms (t/T=0.5), h) 50 ms (t/T=1).

seen by the concentric circle around the pile, which is indicated by air bubbles in the snapshots a), b), and c). Due to the blockage of the tripod the water mass in front of the pile is decelerated, while the water progresses faster beside the main column. The formation of the semi-circular arch indicates the influence of the added mass, which finally generates the hydrodynamic force. However, the extend of the decelerated water volume as well as the resulting velocities are very difficult to measure in laboratory tests. Instead, the availability of the full hydrodynamics are one of the major advantages of the numerical model and analyzed later on in this chapter. Likewise to load case 2, the wave run-up spreads with roughly 10-11m/s across the cylinder surface. The splashing consists of a thin layer and propagates radially in the upper half above the wave crest (Fig. b)). Radial splashing is barely seen downwards the wave crest, instead, 25 ms (t/T=0.5) after the hitting wave the spray is predominantly horizontal (Fig. g)). Besides, a bow wave is observed in snapshot e) and f) at the front side of the cylinder and running upwards until the wave front encounters the cylinder as well. On the backside of the cylinder, vortex shedding develops and the formation of a symmetric wake can be seen.

Load case 4 is the non-breaking wave used as a reference for the load cases 1-3. Snapshots of LC 4 will be shown in combination with the data analysis in the subsequent sections.
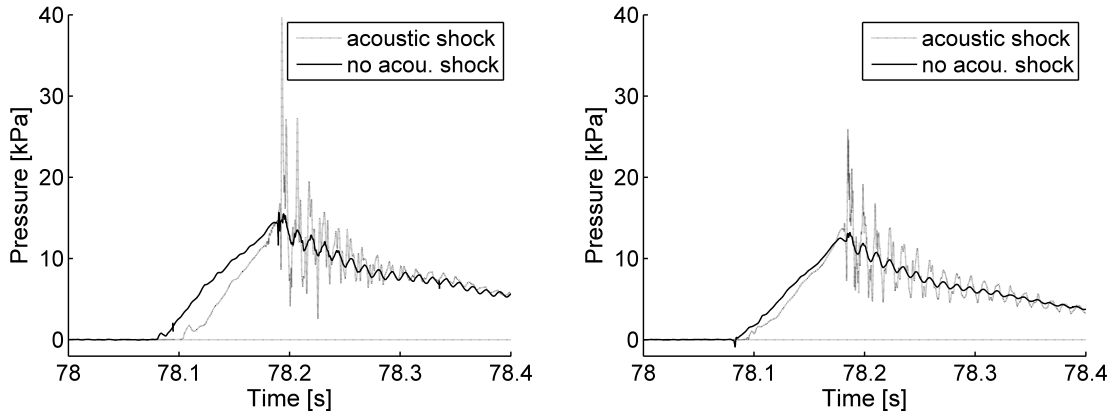
Figure 4.8: Comparison of pressures from LC 3 with and without acoustic shock in a relative height $z/\eta_{max} = 0.82$ at a perimeter angle 0° (left) and 20° (right).

4.4 Structure response and pressure oscillations

In addition to the visual impressions (Fig. 4.5-4.7) of the wave-structure interaction, Fig. 4.8 shows several time series of pressure records for load case 3. The pressure time series clearly shows major oscillations after the impact, which are caused by the structure response of the tripod and are investigated in the following.

The pressure signals in Fig. 4.8 (left) are measured at the cylinder's front in zero degree position. Both exemplary signals are recorded at the relative height z/eta_{max} = 0.82, which is located shortly below the impact of the vertical water front from load case 3 (Fig. 4.7). The dotted line illustrates a test case with an audible acoustic shock at the instant of time when the water front encounters the cylinder. An equally generated test case is represented by the solid line with the distinction that no acoustic shock is observed in this case. Both time series show different magnitudes of oscillations, which are mainly reasoned by the displacement of the main column and the subsequent vibration of the whole tripod structure. The breaking wave represented by the solid line only generates a very week dynamic response and the time series nearly shows the mean trend of the pressure development. Likewise, Fig. 4.8 (right) shows the significance of the cylinder oscillations to the pressure records by the dotted and the solid lines at a perimeter angle of 20° degree. The oscillations for the 20° position are less intensive in comparison to the 0° case, however, predominant to the signal as well. On the one hand this is reasoned by the 20° rotation of the pressure sensor in regard to the main oscillations in the 0° degree plane. On the other hand the difference might be originated by the variance, and thus varying intensity, of the test waves.
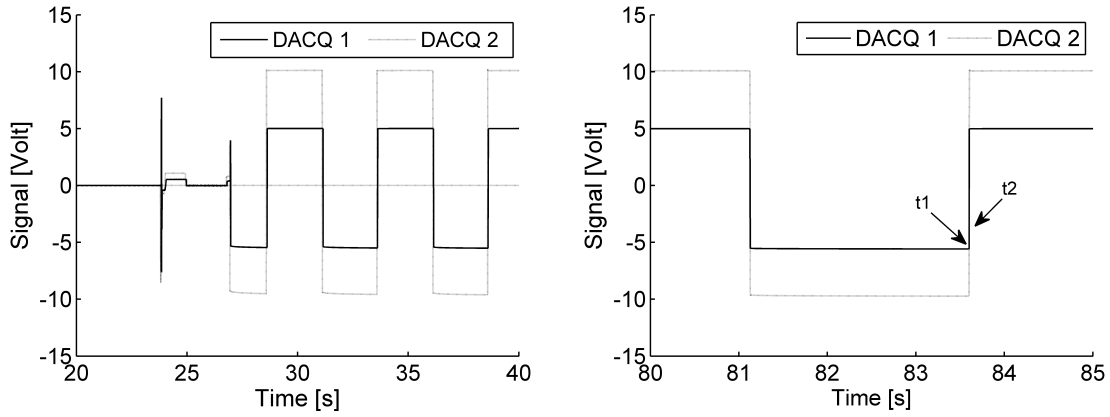
Figure 4.9: Synchronization of data acquisition systems (DACQ) 1 and 2 by a square-wave signal.

The oscillations of the tripod have a major influence on the time series of the measurements, especially on the pressure sensors. They attenuate the real pressure during displacements in wave direction and increase the signal when the main column is bending forward again. Therefore, the dynamic response of the structure is analyzed in more detail in the next subsection. The natural response frequency of the tripod is of major interest and especially the time shift between the impacting wave and the onset of the structure's reaction due to the inertia of the tripod.

4.4.1 Time frequency analysis of acceleration meters

Displacements of the rotational cylinder section are captured by the two acceleration meters perviously described in section 3.1. They directly record the oscillations of the cylinder without being influenced by entrapped air like the pressure signals are. Besides the frequencies of vibration, the time series of the acceleration meters also indicate the point in time of the first displacement as well as the direction. The acceleration meters and the strain gauges are sampled with an additional amplifier and digital interface [1], while all other devices are recorded by the equipment of the large wave flume. The two independent systems need to be synchronized for the overlapping of the acceleration and pressure data. This is realized by a square-wave signal shown in Fig. 4.9 on the left, which is sampled by both systems. A square-wave signal provides clearly indicated positions at the jumps due to their sharp edges. Furthermore, automatic cross-correlations can be easily performed if

the oscillograph is started during the sampling of both systems. The characteristic impulse seen in Fig. 4.9 (left) in combination with the square-wave offers a definite synchronization within the range of the sampling. 1000 Hz is the sampling frequency of the large wave flume system (DACQ 1) and the second setup records with 600 Hz (DACQ 2), which leads to the possible time offsets dt_{sync} listed below. The four cases and intermediate states are randomly distributed and the maximum time offset is 1.6 ms, which must be taken into account as worst case for the investigation of correlated pressure and acceleration data.

$dt_{sync} \approx 0$ s: Both systems sample the change of the square-wave signal shortly after position t1 indicated in Fig. 4.9 (right).

$dt_{sync} \approx 1/600 - 1/1000$ s: Both systems sample the change of the square-wave signal shortly before position t2 indicated in Fig. 4.9 (right).

$dt_{sync} \approx 1/1000$ s: DACQ 1 samples at position t1 and DACQ 2 at position t2.

$dt_{sync} \approx 1/600$ s: DACQ 2 samples at position t1 and DACQ 1 at position t2.

Previous to the combined analysis of the cylinder displacement and the pressure development some hammer shock tests on the main column are investigated. They are preformed to determine the natural frequencies of the tripod and the upper rotational section. Fig. 4.10 shows two similar hammer shocks with the time in seconds given on the abscissa and the acceleration in m/s^2 on the ordinate. The upper one is performed with the still water line 2.5m above the sand profile and labeled with the suffix "SWL". Analogously, the lower time series illustrates a similarly conducted hammer shock without water, which is labeled by the suffix "dry". Both hammer shocks are positioned at a relative height $z/eta_{max} = 1$ and are practically similar in magnitude as well as in shape. The high frequency vibrations last less than a second and show a gradually damped signal.

"Short Time Fourier transformations" (STFT) are used to calculate the spectra over time. On the one hand changes in amplitude and frequency can be handled due to the windowed analysis. On the other hand it is not possible to achieve both a good frequency resolution and a good time resolution (Heisenberg uncertainty). A basic difference of the STFT in comparison to a wavelet analysis is the fixed window length. In a wavelet analysis the width of the window is changed as a function of the analyzing frequency. Futhermore, the wavelet can be chosen with regard to the problem in contrast to the sine and cosine functions used in STFT. However, the main reason to use STFT for the oscillation analysis instead of wavelets is the higher achievable frequency resolution with STFT and the good fitting of the trigonomet-
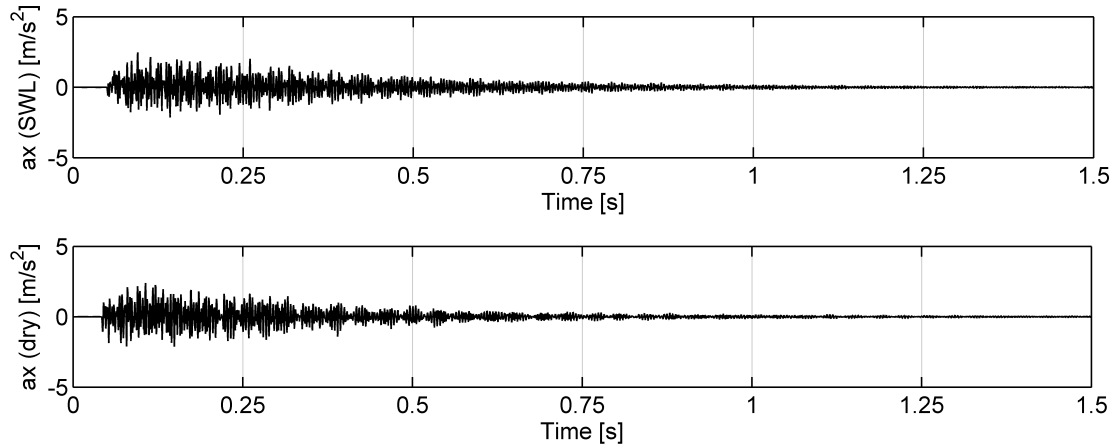
Figure 4.10: Horizontal acceleration due to hammer shocks on a level with the wave crest; for still water level depth (upper) and without water (lower) plot.

ric functions, since the oscillation problem mainly consists of harmonic fluctuations with significantly changing amplitudes over time but rather slightly changing frequencies (i.e. Fig. 4.11). Therefore the STFT produces more satisfying results for these gradually changing signals, while wavelets show a better performance for the detection of trends, discontinuities or breakdown points.

In Fig. 4.11 the abscissa gives the time in seconds, the colorbar shows the magnitude of the power spectra, and on the ordinate the range of measurable frequencies is limited to 300 Hz due to the previously mentioned sampling rate of 600 Hz. The detection of the contained frequencies is sensitive to the chosen length of the time window. For the analysis the window size was varied by whole numbers of power 2 with regard to the sampling rate. This leads to the following useful time frames of $2^8/600$=0.43 s, $2^7/600$=0.21s, $2^6/600$=0.1s, $2^5/600$=0.05s, and $2^4/600$=0.027s to analyze the hammer shock with a duration less than a second. Window sizes in the range of 0.027 and 0.05s are too small for the detection of the lower natural frequencies around 11-12 Hz of the structure. Only high frequency vibrations are found by these window sizes due to the lower limit 1/0.05=20 Hz and 1/0.027=37 Hz of included frequencies. Larger time windows overcome this problem, however, large window sizes are no longer capable to firstly detect modified frequencies within the signal and secondly to recognize any changing amplitude with time, i.e. the damping of the hammer shock. A Fourier transformation implies a periodic signal with various but stationary frequency components. While a constant 20 Hz oscillation in time domain is represented by one amplitude and phase information in frequency domain, the signal of a damped 20 Hz oscillation is decomposed into a relatively broad spectrum around the 20 Hz peak frequency. Even tough the frequency in the signal is not modified the Fourier transformation "needs" more frequencies as

Figure 4.11: Time frequency spectra of the acceleration meter positioned at $z/eta_{max} =$ 1.1 with a window size of 0.1s and 50% overlap from hammer shock tests in still water level conditions (2x left) and without water (2x right).

substitution for the decomposition of the fading amplitude. Small window sizes are advantageous for the localization of frequency changes in the time series, while large windows have a higher frequency resolution and are capable to estimate the amount of amplitude change. Therefore a window size of 0.1s is taken for the analysis of the hammer test, since this time frame is the best compromise in regard to the detectable frequencies and at the same time short enough to recognize changes in time.

Furthermore, the succeeding time frames can be overlapped to obtain more spectra along the time series of the signal and to zoom into the time frequency changes, if necessary. For example, a 0.1s frame with an overlap of 0% splits a one second time series in ten spectra. 50% overlap between the time frames doubles the number of spectra for the same signal with equal window size.

Fig. 4.11 displays the frequency spectrum of different hammer shocks. The two first plots on the left show the frequency spectra for still water conditions of the tripod while the other two plots illustrate the shocks without water in the flume. On the ordinate the subscriptions indicate the position of the hammer shocks, which are performed at the top end of the cylinder and shifting downwards by 0.5m steps down to the SWL. The location on a level with the targeted maximum water level is indicated by the index "top" and the lowest position by "bottom". There is no significant variation of the spectra along the cylinder's span, which is why the "top" and "bottom" cases are selected for illustration purposes in Fig. 4.11.

All four displayed hammer shock spectra show the high frequency vibrations with distinctive peaks at 262 Hz as well as at 235 Hz. In correlation with the time series given in Fig. 4.10 they last about a second and also show the gradually decreasing amplitudes as well as the rise time of 0.08s before the peaks. These natural frequencies are relatively high and originate from the stiff rotational section

fixed by tension. The motion of the cylinder connected to these high frequencies is very small, while the less activated frequencies around 105 Hz and 28 Hz have a greater contribution to the displacement of the cylinder. The last mentioned components are present in all spectra, although they are barely seen due to the week excitation of the tripod substructure by the hammer shocks. As mentioned above the spectra of the various hammer shock positions do not change remarkably and the frequencies as well as their period of oscillation are too similar to point out significant differences.

Fig. 4.12 shows the spectra of the four wave types measured with the same acceleration meter located at $z/\eta_{max} = 1.1$. Each subplot contains a series of frequency spectra with three test waves for the load cases 1-3 and with two tests for load case 4. For illustration purposes the limits of the colorbars are adjusted to maximum values of 1 for LC 1 and 2, five times higher for LC 3, and reduced to 0.05 for LC 4, while the ordinates equally range from 0 to 300 Hz. *Load case one* with the broken wave shows two major peaks in the corresponding spectra on the top left in Fig. 4.12. They are most obvious in the third spectrum and located at the frequencies 100-105 Hz and 12 Hz. Higher frequencies and the perviously observed 262 Hz and 235 Hz are marginal pronounced or not present in these three spectra. Instead, the high component around 235 Hz is observed in *load case 2* in addition to the lower frequencies 12 Hz and 85 Hz. The fist spectrum clearly shows these three peaks in combination with a weak fluctuation around 185 Hz. The same spots are seen with less intensity in the spectrum of the second test wave and the third spectrum only highlights the two lower frequencies at 85 Hz and 12 Hz. No distinct peaks are present in the region higher than 100 Hz for the third case. The periods of oscillation are roughly 0.36s and hence of similar duration in comparison to LC 1. The wave impact of *load case 3* produces the most intensive structure response by the hitting water front on a high level in contrast to the former cases with a downward directed wave tongue, as described in section 4.3. Note that the upper limit of the colorbar is therefore set to five in Fig. 4.12. Two frequencies are present in all three test waves of LC 3. This is 85 Hz in correlation with LC 2 and the second one is 10 Hz slightly reduced to the 12 Hz observed before in LC 1 and 2. Furthermore, test wave one and two of LC 3 show the same high frequent components at 190 Hz and 205 Hz as well as at 230 Hz, while the third spectrum practically shows no excitation at 205 Hz and 230 Hz. The period of oscillation is slightly increased in comparison to the former load cases and takes 0.36-0.4s. *Load case four* barely displaces the tripod and therefore the two spectra only consist of very weak oscillations around 10 Hz and of even minor fluctuations around 85 Hz.
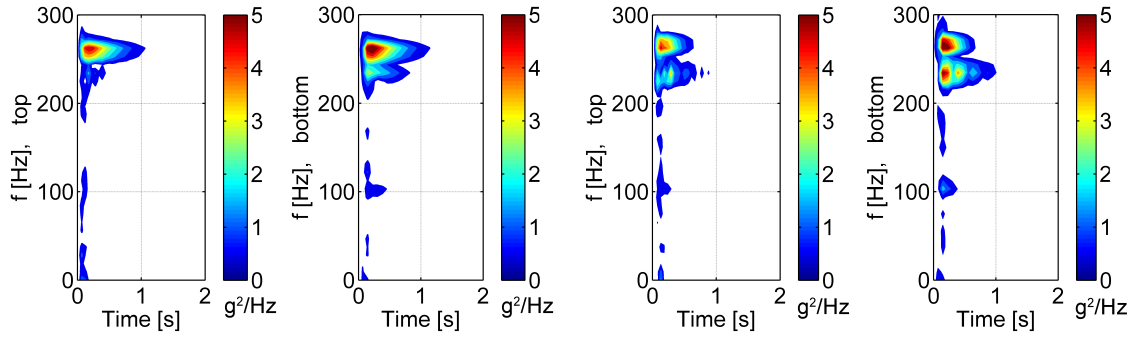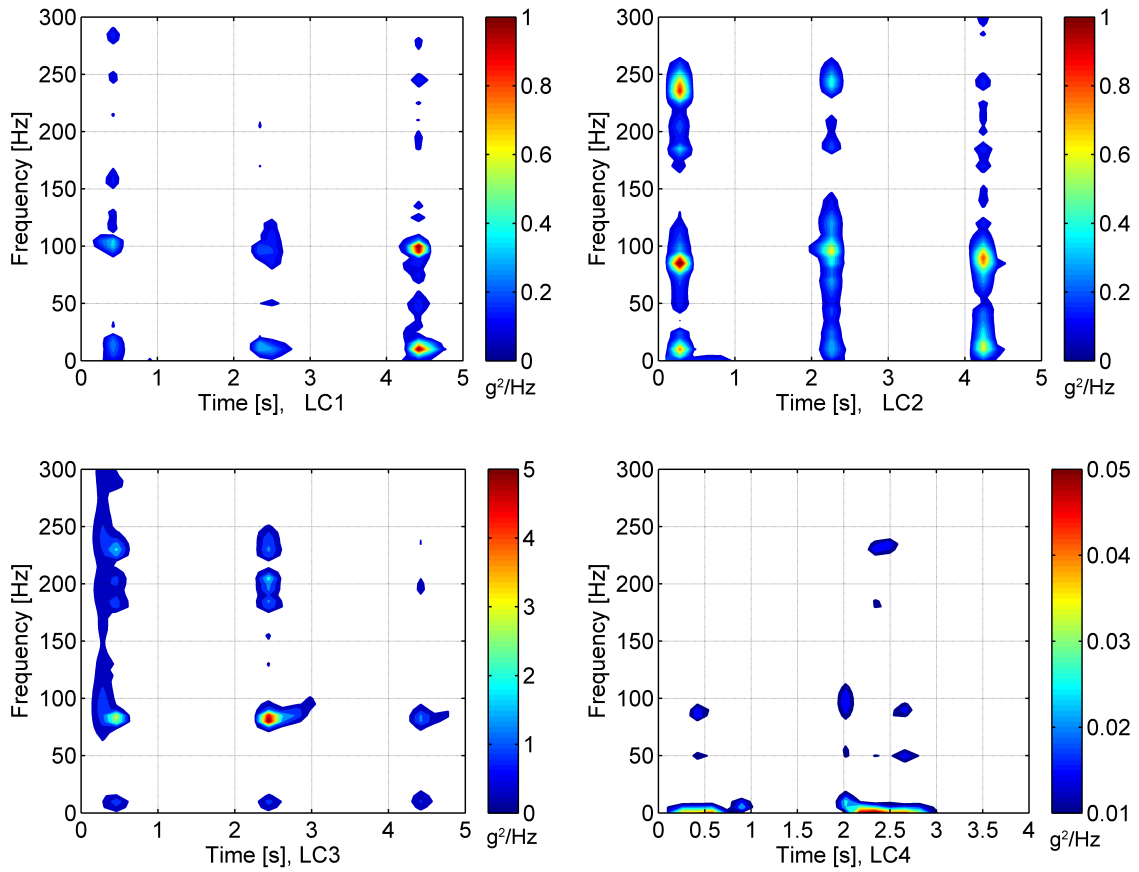
Figure 4.12: *Time frequency spectra of the acceleration meter positioned at $z/eta_{max} = 1.1$ with a window size of 0.2s and 20% overlap. All spectra are measured with the rotational section in 0° position and three test waves for LC 1-3 and two for LC 4.*

The oscillations of the cylinder due to the hammer shock tests differ form the measured spectra of the tested waves. The lowest frequency observed by the hammer shock tests is about 28 Hz in contrast to the 10-12 Hz found for all excitations by the test waves. Furthermore, the next higher frequency around 105 Hz seen in the hammer shock spectra only appears in LC 1, while LC 2-4 show a reduced frequency of 85 Hz. In addition to the changed natural frequencies the periods of oscillation ranging from 0.3 to 0.4s are about half as long as recorded for the hammer shock tests, although the wave slamming is more intensive. These observations might be reasoned by the effect of the hydrodynamic water mass. During the hammer tests the main column freely vibrates above the still water level. In contrast to that the fluctuations of the cylinder generated by the impacting water front are quickly dampened by the immediately passing wave crest. The increased water level up to 1.1 m in combination with the maximum velocities under the wave crest significantly influence the structure's response according to the previous observations. This as-

pect probably gives reason to the frequency shifts as well from 28 Hz down to 12 Hz and from 105 Hz to 85 Hz, since the "added mass" of the water body increases the inertia of the system and consequently reduces the oscillations. In comparison to LC 3 and 4, the first two load cases have less high water elevations at the main column and contain much more entrapped air duo to the wave breaking distance (compare Fig. 4.5-4.7). The lower crest level as well as the reduced water density by the enclosed air might be the cause for the minimal frequency shift from 12 Hz (LC 1 + 2) down to 10 Hz (LC 3 + 4).

4.4.2 Time frequency analysis of pressure sensors

The preceding analysis of the acceleration meters clearly shows oscillations of the tripod in response to the test waves. Major frequencies are 10-12 Hz, 85 Hz, as well as 230 Hz and presumably the structural response is influenced by the wave breaking type and depends on the flow of the passing water mass. Two questions arise with regard to the pressure measurements:

- Are the pressure signals influenced by the oscillations of the tripod structure?

- Is there a time shift between the slamming pressure and the response of the tripod due to its inertia?

With regard to the first item, Fig. 4.13 shows pressure measurements of LC 1-3 from left to right as well as the corresponding frequency spectra of the time series for direct comparison to the above given spectra of the acceleration meter. All signals are taken from the pressure sensor at the relative height $z/eta_{max} = 1.03$, which is located close to the acceleration meter ($z/eta_{max} = 1.1$) and within the area of the slamming wave front. Each plot illustrates the pressure signals of three equally generated waves, whereby the plots are shifted to each other by one second for better illustration purposes. The three pressure time series differ more and more from each other with increasing load case number, which will be further described in chapter 6.

The oscillations of the cylinder and the appearing frequencies in the pressure signals show similarities and differences at the same time. For *load case 1*, the first spectrum shows additional frequencies around 20 Hz, 35 Hz, and 60 Hz in the pressure measurements next to the already observed components at 12 Hz and 100-105 Hz for the motion of the cylinder. These frequencies are reproduced as well in the second and third spectrum, however, the higher components above 60 Hz are less intensive
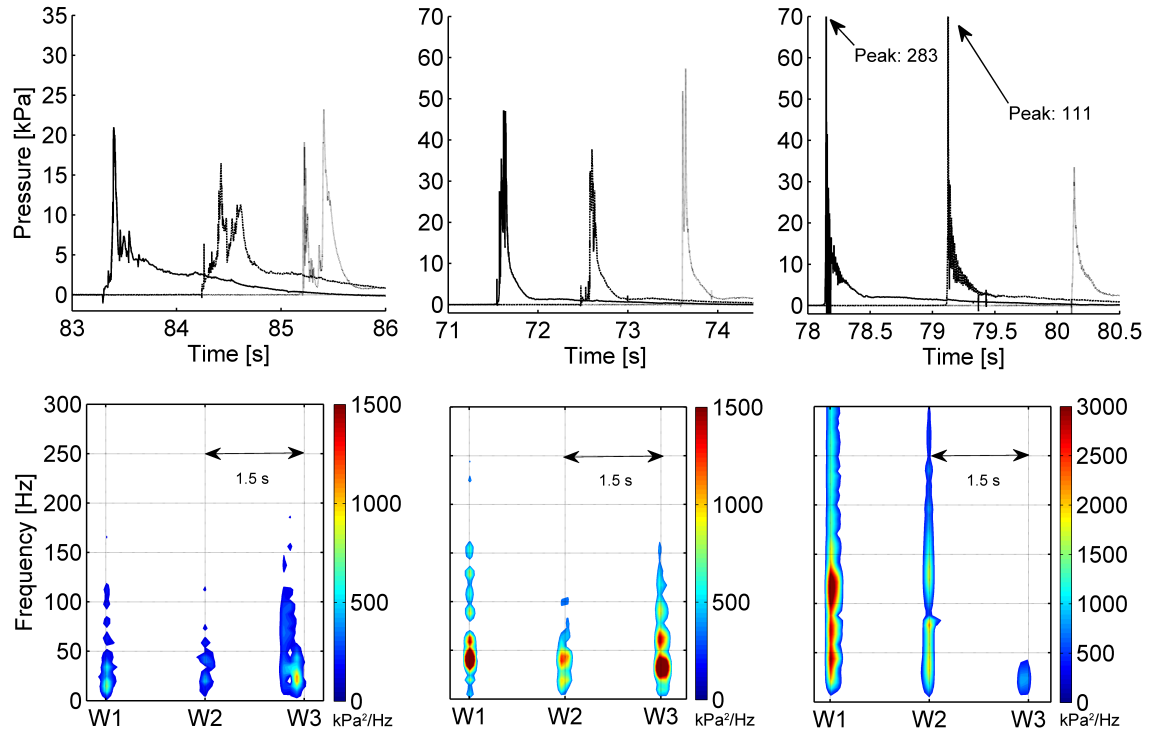
*Figure 4.13: Pressure signals of three test waves at z/eta_{max} = 1.03 for LC 1-3 from left to right and corresponding time frequency spectra of the acceleration meter positioned at z/eta_{max} = 1.1 with a window size of 0.2s and 50% overlap.*

in the second spectrum. Besides the local fluctuations on a level with the wave crest Fig. 4.14 gives an overview of the fluctuations along the whole cylinder's span. Again, the abscissa ranges from 0 Hz to 300 Hz and the x-labels indicate the relative heights of the synchronously recorded pressure sensors. All three contour-plots show the first test wave out of three, whereby the spectra of the second and third waves are similar to the selected one. The above mentioned characteristics for the relative height 1.03 are also observed for the lower located pressure spectra between the relative heights 0.62 and 1.03. At these positions the dominant frequencies appear at 12 Hz, 85 Hz, and 100-105 Hz in correlation to the spectra of the acceleration meter as well as the peaks at 20 Hz, 35 Hz, and 60 Hz only present in the pressure signals. Fluctuations below z/eta_{max} are rather weak and no dominant peaks are obvious in comparison to the upper section. Same applies for the top section above the hitting wave crest at the relative heights z/eta_{max} 1.13 and 1.24. Practically no oscillations are found at the two upper heights except short excitations around 35 Hz. The middle section with the most intensive fluctuations might correlate with the vertical width of the foamy water mass seen in Fig. 4.5. As previously described in section 4.3, the air transported into the wave crest might cause the additional frequencies by the entrapped air bubbles.

For *load case 2* the natural frequencies of the tripod near 12 Hz, 85 Hz, and 105 Hz are also found in the three pressure spectra as seen in Fig. 4.13. Similar to LC 1 additional peaks are seen at 20 Hz, 40 Hz, and 60 Hz. Furthermore, the first and third test case reveals moderate oscillations near 120 Hz and 155 Hz. By comparison to LC 1 the intensive fluctuations for LC 2 cover a smaller area along the cylinder's span and focus between the relative heights 0.83 and 1.13 (Fig. 4.15) with frequencies at 20 Hz and 40 Hz. The central location around the wave crest at z/eta_{max} 0.93 - 1.03 is additionally characterized by oscillations at 60 Hz and higher components, next to the structural response around 10 Hz, 85 Hz and 105 Hz. The re-occurring frequencies at 20 Hz, 40 Hz, 60 Hz in combination with the more distinct high frequencies above 105 Hz give rise to the thought of air bubble interaction, again.

The possible connection of pressure oscillations and entrapped air is underlined by the observations for *load case 3*, since the intensity and the appearance of these frequencies is even more focused at $z/eta_{max} = 1.03$ for the wave breaking directly at the main column. Fig. 4.16 shows the most intensive pressure oscillations on a level with the wave crest at the frequencies 40 Hz, 70 Hz, and 115-120 Hz. In comparison to the former observations these components are far more energetic (note the doubled range of the colorbar) and slightly shifted to higher frequencies. Furthermore, the two neighboring positions to $z/eta_{max} = 1.03$ contain lower frequencies around 10-50 Hz and around 115 Hz as well. Except for $z/eta_{max} = 1.24$ the structure response at 85 Hz is present in all pressure recordings due to the strong wave impact. The intensity of the local impact pressure near the wave crest level significantly varies in LC 3 (Fig. 4.13). Likewise, the three associated spectra differ in intensity from left to right. Broad spectra with the above mentioned lower frequencies as well as components in the range of 73-85 Hz, 115-120 Hz, and beyond are characteristic for the two first intensive pressure time series. In the third time series the tripod is accelerated ten times weaker in contrast to the first case, whereby the maximum force in horizontal direction is 90% of the force estimated for the first test wave (Chapter 6.2). Maybe this is why the natural frequencies around 10-12 Hz, 85 Hz, and 105 Hz are missing in the spectrum and only light fluctuations at 20 Hz and 40 Hz are present in correlation to the former cases, presumably caused by air bubbles.

4.4.3   Conclusions

The reproduction of the breaking waves is of significant importance for the usage of the rotational main column. Water elevation records as well as pressure sensor

Figure 4.14: Time frequency spectra with a window size of 0.2s and 50% overlap of pressure signals along the cylinder front at relative height z/eta_{max} for LC 1.

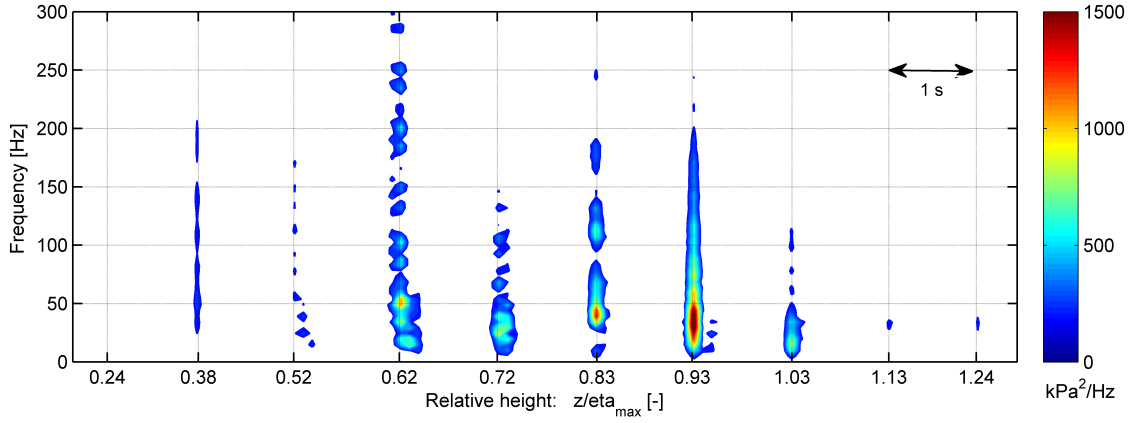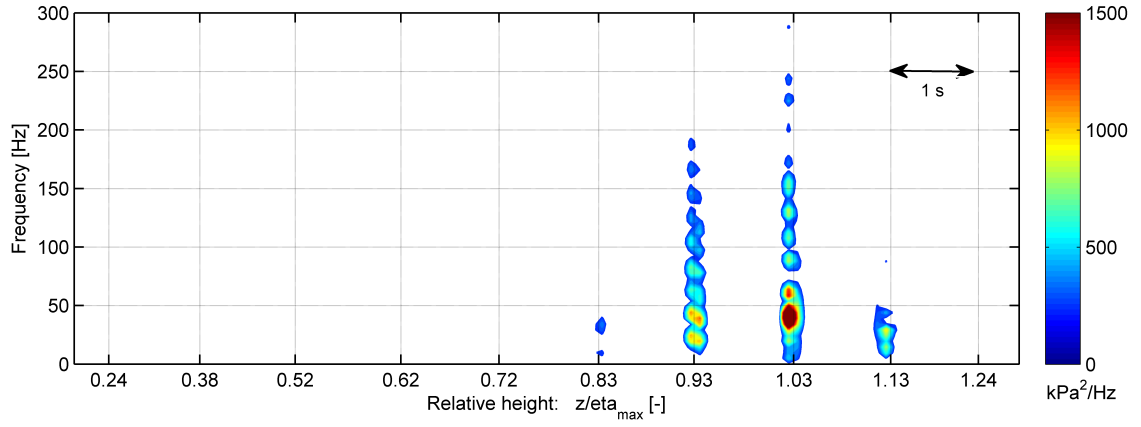
Figure 4.15: Time frequency spectra with a window size of 0.2s and 50% overlap of pressure signals along the cylinder front at relative height z/eta_{max} for LC 2.
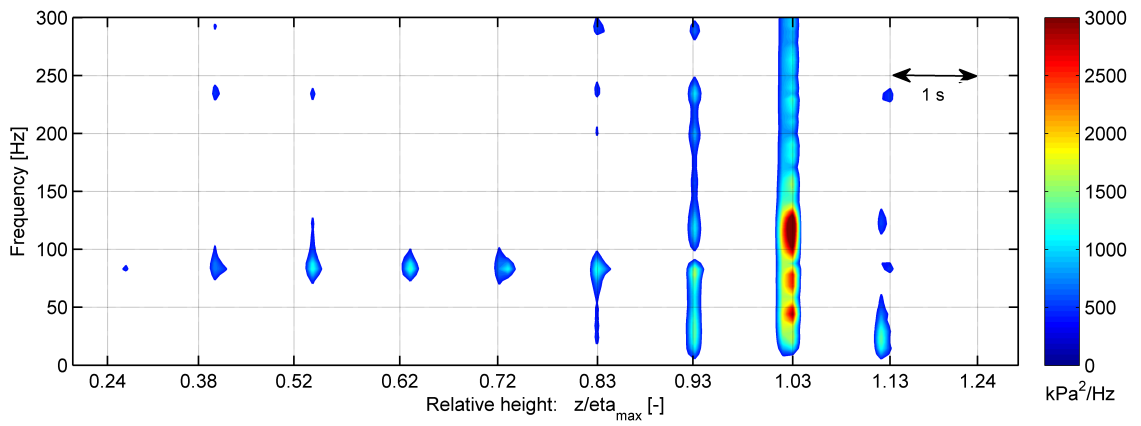
Figure 4.16: Time frequency spectra with a window size of 0.2s and 50% overlap of pressure signals along the cylinder front at relative height z/eta_{max} for LC 3.

data below the impacting wave tongue reveal negligible deviations for the four tested waves. However, this work is focussing on the pressure and force development within the splashing area where pressure deviations are present. Therefore, the slamming tests could be improved by a high number of pressure sensors to simultaneously measure and cover the tripod surface. Nevertheless, 20 out of 30 simultaneously measuring pressure sensors are fixed to the rotational main column and provide a valuable data basis for the validation of the CFD model described in the next chapter. Moreover, it was found that the single test runs can be coupled with limitations, despite the present fluctuations in some pressure signals due to the distinctive characteristics of the pressure time series, which will be used in Chapter 6. A major aspect regrading the limitations of the coupling and therefore a reason to include a CFD model is the structure's response, which is discussed in the following.

The tested load cases show oscillations of the tripod structure at similar frequencies, mainly at 10-12 Hz, 85 Hz, 100-105 Hz, and approximately 230 Hz. Since any back and for movement of the cylinder has influence on the pressure records, the spectra of the pressure time series show oscillations at these frequencies combined with additional peaks caused by the wave impact and probably by entrapped air, as described above. The structural motion is challenging for the analysis of the time dependent trends of the pressures and especially for the analysis of the peak values. This aspect is most pronounced in some test cases of LC 3 and exemplarily illustrated in Fig. 4.17 (right). Pressure and acceleration signals are displayed by the solid and dashed lines, respectively, whereby the positive axis of the horizontal acceleration meter points to the wave maker and the negative axis in direction of wave propagation. The acceleration is the second derivative of the cylinder's displacement as illustrated in Fig. 4.18. The cylinder moves forward beginning at the acceleration minimum t_1 until the direction of motion is reversed at the acceleration maximum t_2. It should be noted here that a sampling rate higher than 600 Hz would be favorable for this high level of details.

The first movement of the cylinder is induced by the approaching lower part of the wave crest prior to the pressure peak, which gently (no impact yet) pushes the tripod in wave direction. This is seen in Fig. 4.17 (right) by the small negative trend of the dotted acceleration signal followed by the forward movement until 78.1467s. The wave hits the cylinder somewhen during or after the forward bending of the cylinder and its motion is reversed 1.7 ms later at 78.1484s. The peak pressure of nearly 300 kPa includes speculation since value and position of the acceleration maximum cannot be determined exactly. On the one side the peak value might be too high, if the cylinder is still moving forward during the impact. This would be the case if
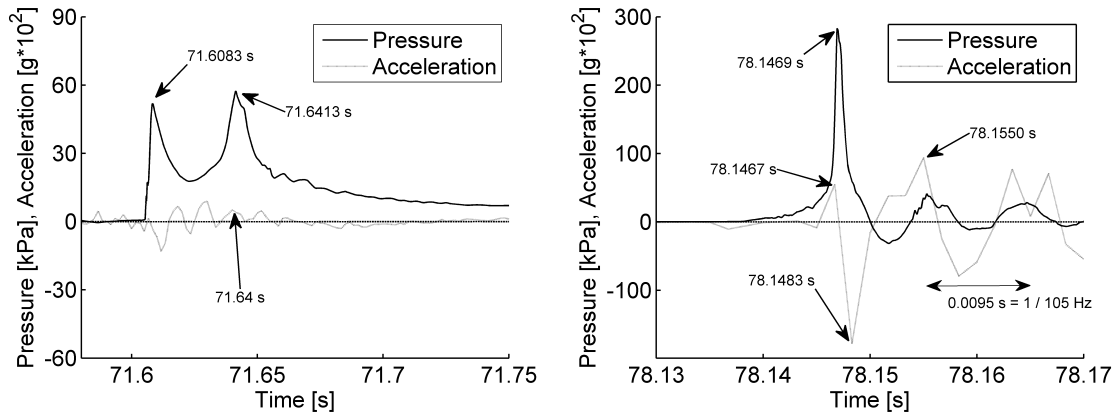
Figure 4.17: Pressures time series at $z/eta_{max} = 1.03$ and horizontal acceleration at $z/eta_{max} = 1.1$ for LC 2 (left) and LC 3 (right).

the acceleration maximum occurs after the pressure peak at 78.1469s. On the other side the peak value might be reduced in comparison to the real acting pressure, if the maximum acceleration occurs before 78.1467s. In this case the cylinder would already move in wave direction, again, before the maximum pressure occurs and thus suspend from exposure. For LC 3 the acceleration due to the impact is roughly $1.8g$ in wave direction and clearly dominates the pressure record, seen by the structure's 105 Hz oscillation with even negative pressure values.

For LC 2 the representatively shown acceleration is 18 times smaller and only amounts $0.1g$ in wave direction (Fig. 4.17 left). The small fluctuations of the acceleration as seen between the two pressure peaks have a frequency of 85 Hz and are superimposed to a barely seen longer oscillation of about 11-12 Hz. These two frequencies belong to the previously observed natural oscillations of the tripod. In this case they have no significant influence on the pressure signal and are hardly visible in the pressure signal after the second peak.

Principally, the structural response is of major importance for the prototype design since the interaction of design-loads and the structure defines materials, dimensions, and resulting oscillations. However, for the investigation of the design-load's magnitude itself this effect is generally unwanted in physical model setups, unless the test structure has a scaled stiffness with realistic oscillations. Last mentioned is barely found in literature and most studies deal with a higher stiffness in comparison to the prototype case. The structure needs to be stiff and practically should not oscillate during impact to investigate the pure pressure development. This might be the reason why Chan et al. (1995) are part of a small selection in literature who have published such pressure details, since they report about an adequate test structure.

Most other studies report about integrated forces, often indirectly estimated by the convolution integral whereby the load is kind of iterated in combination with the known structure stiffness until the measured structure response is reproduced.

This work aims on the spatial and temporal pressure distribution as well as the subsequently derived forces on the structure. Although the tripod structure is relatively stiff, some of the measurements are partly influenced by the motion of the cylinder. Therefore, the approach of this work includes a numerical CFD model, which is additionally used for further pressure details due to the infinitely stiff structure. The three-dimensional flow simulations are validated by experiments with marginal structure response, as pointed out above and described in the following.
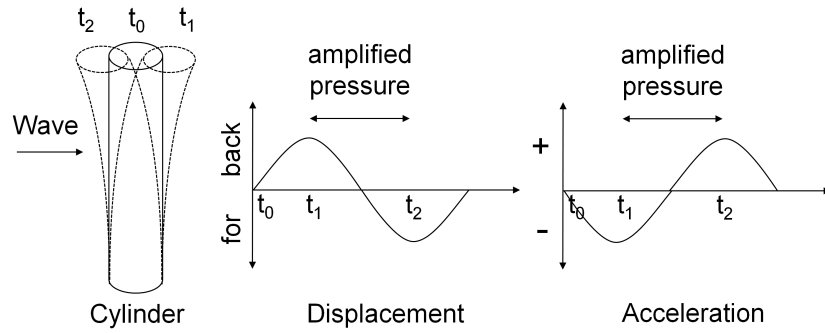
Figure 4.18: Cylinder displacement and sequence of amplified pressures between t_1 and t_2.

5 CFD model for wave impact simulations

On the one side numerical modeling depends on laboratory tests with regard to the model validation and to set boundary conditions, for example. On the other side validated numerical models provide several advantages in comparison to physical models. Deterministic breaking waves are reproduced exactly so that the position of the structure in regard to the impact can be modified without affecting the wave geometry, which is not always possible in large scale experiments. In general, parameters such as hydrodynamic pressure or velocity meters are available for the complete flow domain under the wave and around the structure, whereas in laboratory experiments data points are taken at individual positions and the equipment can even interfere with the flow. The three-dimensional flow simulations based on the Navier-Stokes equations, and described in the following, are simulated with the software package Ansys CFX ® on the basis of the volume of fluid method for surface tracking.

5.1 Modeling of focused waves

The numerical simulations of the large wave flume experiments are conducted in two steps to reduce computation times. At first the development of the wave from the wave maker until shortly in front of the structure is simulated in a quasi-two dimensional model containing only one element in the plain of projection. Subsequently, the velocities immediately before the onset of wave breaking are exported and implemented as boundary conditions in the three-dimensional tripod model. Enormous CPU performance would be necessary to numerically solve the focussing of waves ahead of the tripod as well as the wave impact in a full three-dimensional model.

Since the propagation of the wave packet basically is a two-dimensional problem, a cross-section of the large wave flume is modeled by a thin slice with three-dimensional elements as illustrated in Fig. 5.1 and 5.2. Both figures show the complete domain, which is 4.8m high and 152m long. The width of the slice is adapted to the subsequently described mesh sizes with regard to adequate aspect ratios of the volume
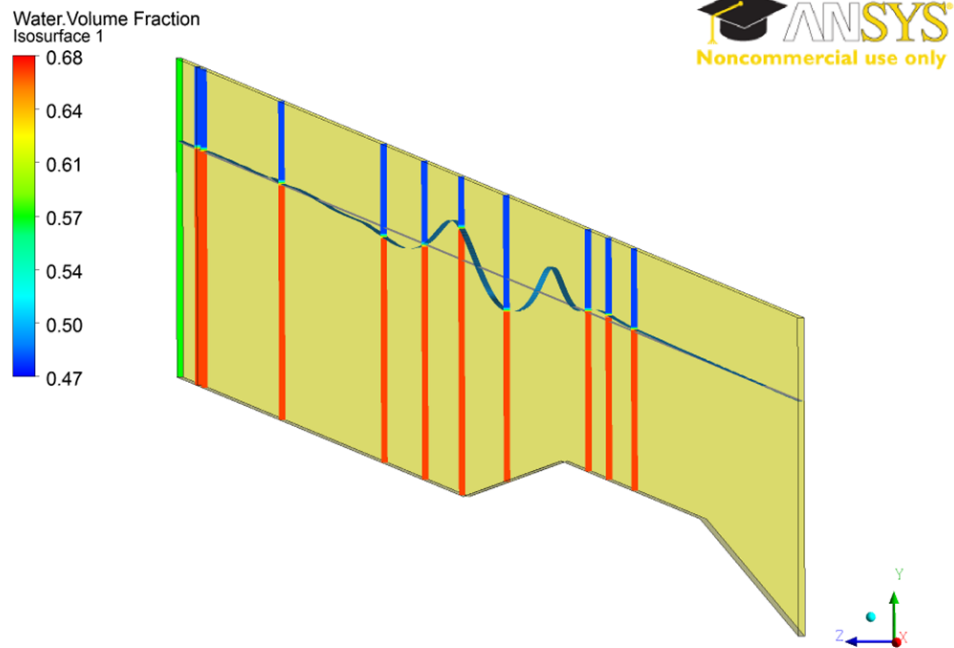
Figure 5.1: Snapshot of the focusing wave packet 65 seconds after the onset of wave generation in front of the tripod position at x = 111m.
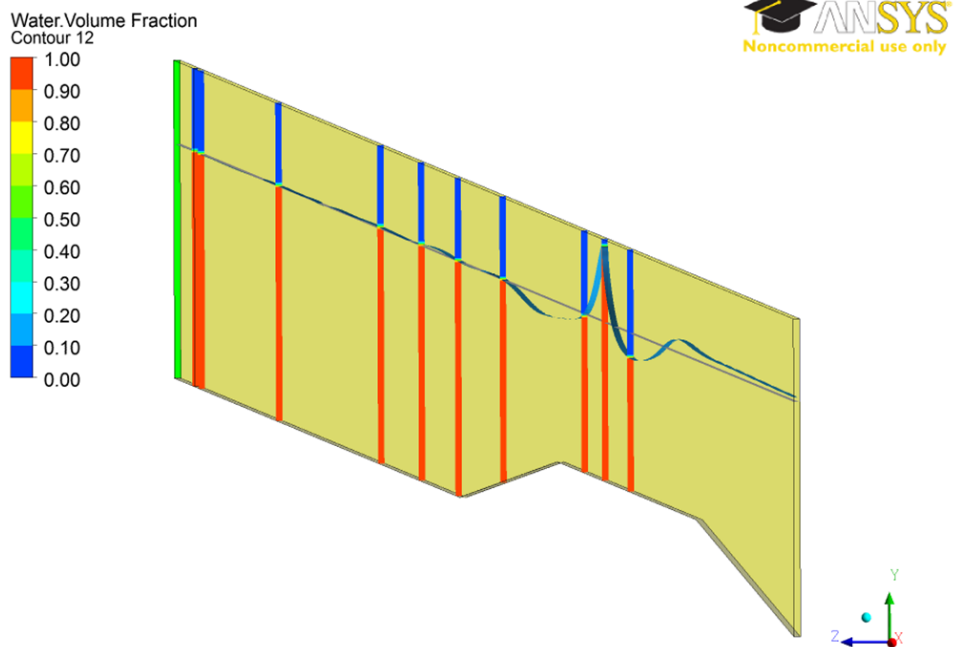
Figure 5.2: Snapshot of the focusing wave packet 72 seconds after the onset of wave generation on level with the tripod position at x = 111m.

elements, because the performance tends to decrease rapidly if there are large element aspect ratios present. In correlation to the physical model the water depth is kept constant at 3.7m in the numerical flume and the bottom is horizontal up to 70m behind the wave maker including the adjacent trapezoid profile with the two 1:20 slopes, as illustrated in Fig. 3.1.

5.1.1   Boundary conditions

The wall boundaries are symmetric on both long sides of the flume. The boundary condition on top is an opening, which keeps the atmospheric pressure in the whole domain by inflow and outflow of air, due to pressure changes at the top side induced by the wave motion.   Opposite the wave maker the outlet of the wave flume is an opening as well, which regulates inflow and outflow of water relative to the hydrostatic pressure distribution for the 3.7m high water level.   In this way the approaching waves are significantly dampened at the wall, however, wave reflection is not fully suppressed. Fig. 5.1 shows the focusing wave packet on a level with the first slope 65 seconds after the onset of wave generation. At this time no wave has reached the backside of the flume yet, while small water elevations ≤ 0.05m are observed at the outlet 7 seconds later (Fig. 5.2). The refections have no significant influence on the focused wave, since they are small and still located in the rear 47 meters, while the wave kinematics at 105m are exported as boundary condition for the tripod model.

Free slip conditions are used at the wave flume bottom, since the friction and the boundary layer effects at the concrete bottom in the physical model are assumed to be negligible for the wave propagation. Shear stresses and normal velocities are zero at the bottom, while the horizontal velocity is not set to zero in contract to smooth walls with slip boundary conditions. For smooth walls the viscous sub-layer is fully established (for steady flow conditions) and viscous shear forces are essential. This viscous sub-layer is not present at rough walls any more and the viscous forces might be neglected. A near-wall flow is considered laminar if y+ ≤ 11.63 and the shear stress at the wall is assumed to be viscous from the beginning. For y+ $>$ 11.63 the flow becomes turbulent and the velocity gradients are taken from the wall function approach. Velocities and derived shear stresses are sensitive to the mesh near the wall, which is usually highly resolved by implemented prism-layers. The assumption of free slip conditions for the channel bottom of this model therefore saves a significant amount of mesh cells and CPU time, since the vicinity of the bottom is not meshed with small boundary layer cells.

Fig. 5.3 shows the recorded motion of the wave board for load case 2 (left) as well as
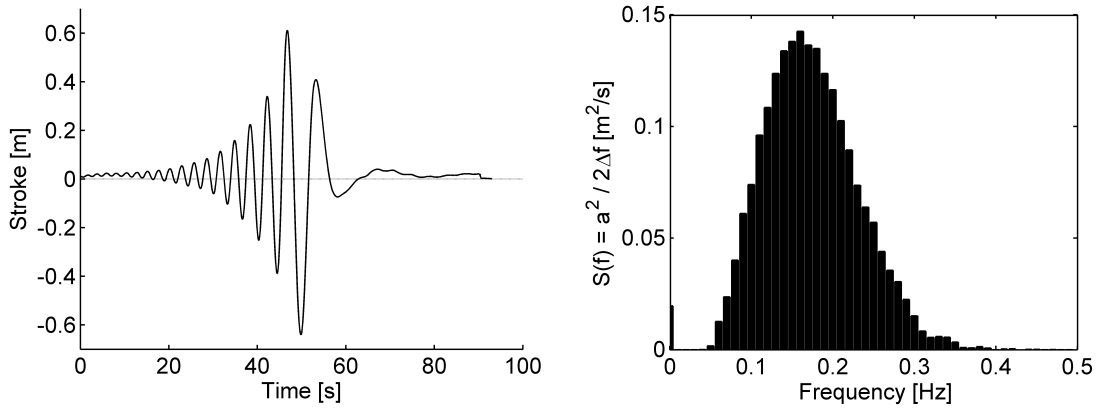
Figure 5.3: Time series of the wave board motion for load case 2 (left) and corresponding power density spectrum (right).

the power density spectrum of the signal (right). The main frequency components of the signal range from 0.05 Hz to nearly 4 Hz and the time series is given by the sum of the components from frequency domain by:

$$\eta(t_x) = \sum_{i=1}^{\frac{N}{2}-1} a_i \, \cdot \, \cos(2\pi \, \cdot \, f_i \, \cdot t_x + \alpha_i) \tag{5.1}$$

with $\eta(t)$ = free water surface in time domain, t_x = 1, 2,... N = t/Δt, N = number of time steps Δt in the time series, a = amplitude, f = frequency, and α = phase shift of a component. This function is implemented as expression to the pre-processor for the motion of the wave board taking arbitrary time steps for adaptive runs into account.

5.1.2   Fluid model and mesh

The fluid domain is isothermal and the turbulence is modeled by the SST k-ω-Model (Shear-Stress-Transport, Menter (1994)), which copes with near wall regions and free stream conditions by the use of a blend-function. Areas close to walls and inside the boundary layer are handled by the k-ω formulation, while the k-epsilon model is used for free flows. Since the domain is enclosed by symmetry-walls and the water motion predominantly takes place in the upper section of the water body at the surface, the turbulence principally is modeled by the k-epsilon model in this quasi two-dimensional case.

Usually, the volume of fluid method is based on a fixed grid within a domain and the

free surface is located inside. The position of the water surface is computed by the volume fraction of fluid inside the elements at the air-water interface. An equation is solved for the transport of the liquid phase as well as for the motion of particles at the interface, also known as marker-and-cell method (MAC) proposed by Harlow and Welch (1965). The precision of the determined free surface is important, since the velocities are derivatives and the result is used as boundary condition for the next time step. Four cases are differentiated. If three sides take inflow, the fourth side is solved by the continuity equation. If only two sides take inflow the direction of the momentum does not change and opposite walls get the same flow. Likewise, the inflow at only one side sets the outflow at the opposite wall. Finally, a falling drop or enclosed water represents the fourth case, which is challenging to track by markers. In comparison to moving mesh methods this method is characterized by a higher robustness. The breaking wave problem of this study can be handled, however, a very fine and time consuming mesh is needed in the area of splashing with rapidly changing velocities and surface deformation, as pointed out further down below.

Table 5.1: Hexa-mesh sizes for simulations a to f with element height H, length L, width W, number of nodes and elements, and elements per meter height and length.

Mesh	H [cm]	L [cm]	W [cm]	Nodes	Elements	Elem./m_H	Elem./m_L
a	14	20	10	39572	19000	7	5
b	8	10	10	155142	76000	13	10
c	3	8	5	311144	153790	33	13
d	2	5	5	729840	361760	50	20
e	1,7	5	3	1216400	604960	59	20
f	1,3	2,6	3	2625000	3943493	77	38

As listed in table 5.1, the hexa-mesh sizes are increased stepwise for the quasi two-dimensional case until the wave shape in terms of wave period and wave height matches the wave gauge records from the experiments. In addition to the height and length of the wave the wave front steepness is of special interest. Practically, the time series between the preceding trough and the crest height of the breaker is the decisive criterium for the quality of the simulation. This is reasoned by the high sensitivity of this time frame to the shape of the breaker observed in the two-dimensional model as well as in the three-dimensional model. Furthermore, the mesh size affects the time series of the board motion like an applied filter due to the numerical diffusion along wave propagation. On the one hand numerical diffusion is accepted and commonly used in regions behind a certain point of interest, i.e. behind the tripod structure to dampen out reflections from the rear wall. On the other hand the diffusion blurs details of the simulations like small frequency components
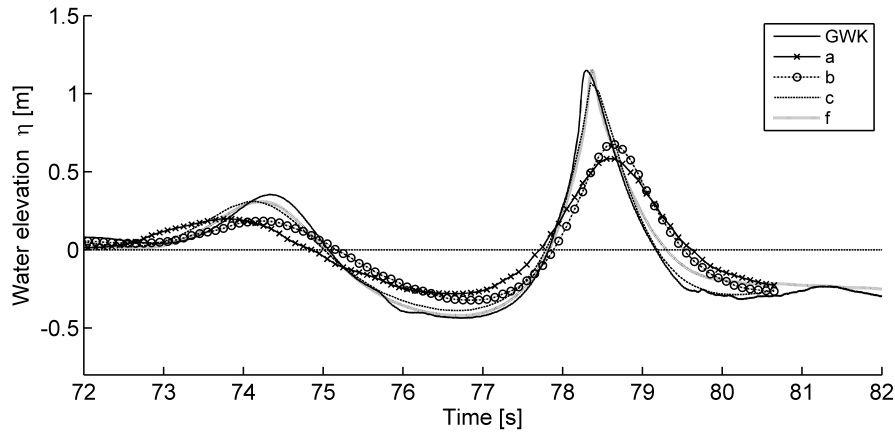
Figure 5.4: Wave gauge signal from large wave flume experiments (GWK) at the tripod position in comparison to time series of CFD simulations with meshes a, b, c, f in the quasi 2D model as listed in table 5.1.

of the wave board motion, as observed by these studies.

This is illustrated in Fig. 5.4 by the comparison of wave gauge series at the tripod position from CFD runs and GWK experiments. Case a represents the coarse mesh with cell dimensions of 14 cm height and 20 cm length. The wave shape shows the lowest crest height, longest period, and the broadest trough and crest width due to the diffusion of the higher frequency components. It can be seen by the exemplarily plotted cases b, c, and f that increasing mesh densities preserve the higher components. The crest height increases, the horizontal and vertical asymmetry of the wave shape is reproduced as well as the wave period. Similar effects, but less pronounced as seen for the mesh density, are found for varying time step sizes from 0.1s down to 0.01s and 0.001s.

Finally, the focused wave package simulated with mesh f is used as boundary condition for the three-dimensional case. The simulation time is 80s and took 8 days on 12 CPUs with nearly 10 GB memory.

Note that the wave board motion was also used to simulate the focussing wave package by potential flow theory up to the moment of wave breaking. The code developed by Sriram et al. (2006) takes only a couple of minutes in this case and the wave profile fits equally good to the GWK measurements as the CFD results.

5.2   Modeling of wave impacts

Fig. 5.5 gives an overview on the breaking wave and the tripod structure in the three-dimensional model. The time steps between the snapshots are referenced to
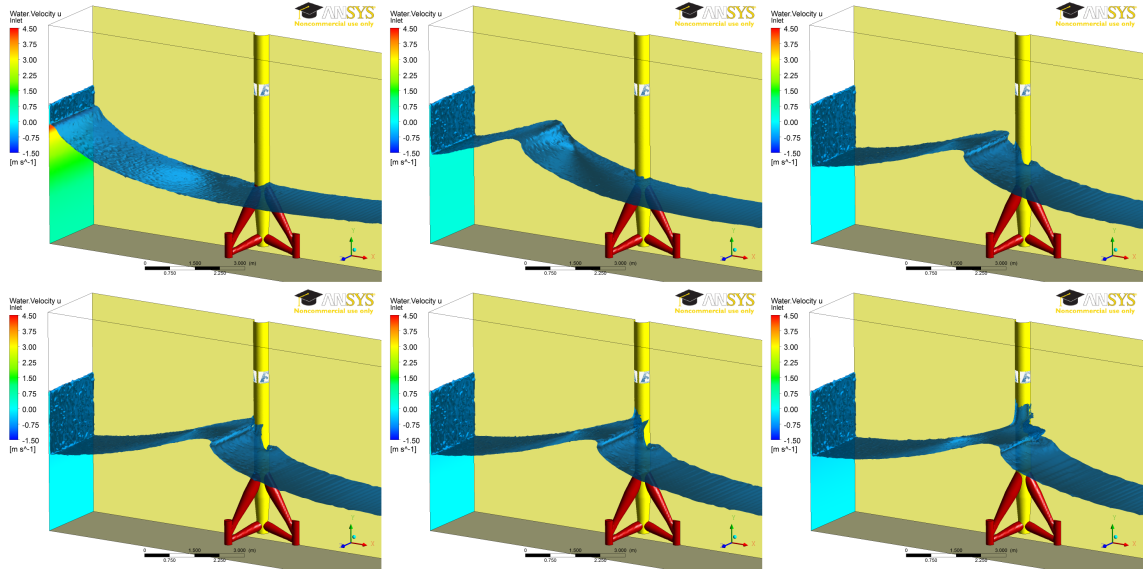
Figure 5.5: *Breaking wave impact on the tripod structure in the three-dimensional model illustrated by snapshots referenced to the wave period T taken from two successive zero down-crossings at the center line of the main column. t/T = 0.60, 0.75, 0.84, 0.86, 0.87, and 0.90.*

the wave period T taken from two successive zero down-crossings at the center line of the main column, which is the duration of the crest and the preceding trough of the breaking wave. The point in time t/T = 0 denotes the approaching trough at the tripod, while the value t/T = 1 is the point in time when the breaking wave crest has passed the main column. The snapshots illustrate the developing wave profile initialized by the velocity distribution of the focused wave exported from the two-dimensional model. The wave crest propagates with 4.8m/s and steepens along the 6 meter distance to the tripod (t/T = 0.75). Shortly before the main column the wave crest starts to curl over at t/T = 0.84. Subsequently, the wave encounters the cylinder on the front side, while a deep sunk develops on the rear side of the main column (t/T > 0.86). Snapshot t/T = 0.90 shows the broken wave as well as the developing wave run-up at the cylinder. As further described in the next chapter the 6m distance between the tripod and the inlet is chosen with regard to different load cases, whereby the tripod is shifted back and for within the same breaking wave.

The fluid model for the tripod simulations is similar to the settings described in section 5.1.2, whereby inhomogeneous multi-phase flow is used in this case to separately solve the differing velocity fields of air and water, especially during splashing. The bottom is assumed to be frictionless again, and the walls on the left and right side are set to symmetry conditions. Slamming pressures and acting forces are symmetric to the cylinder's span in practice (i.e. Chan et al. (1995) and Wienke (2001)),
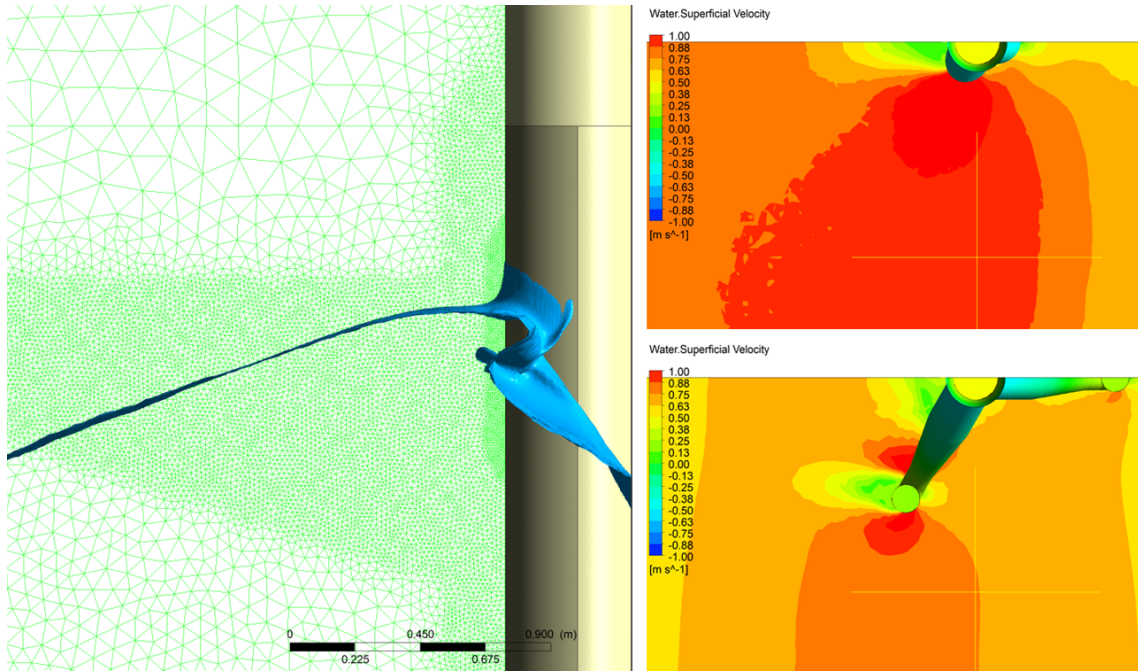
Figure 5.6: Left: Cross-section of the left symmetry plane with various mesh densities adjusted to the impact region and wave propagation. Right: Horizontal water velocities 2m (top) and 0.7m (below) above the bottom for the wave crest on a level with the tripod main column.

which is why the domain is split through the middle of the tripod. Comparisons of symmetric models and selected cases with a full tripod structure do not reveal obvious differences with regard to the splashing, wave run-up, water levels around the cylinder, as well as for pressures and forces. The symmetry condition is acceptable for the wave breaking problem as long as vortex shedding effects have no significant contribution to the total forces. Otherwise the shedding process and the wake is constricted by the symmetry condition.

Computation times are further reduced by truncating the flume width on the outer side of the domain. The symmetric model of the wave flume is 2.5m wide and Fig. 5.6 (right) shows the horizontal water velocities 0.7m and 2m above the bottom for the passing wave crest next to the main column of the tripod. Contour lines orthogonal to the opposite wall of the tripod indicate regions not affected by the structure. This area extends over 1m at the lower levels (Fig. 5.6, right below) and clearly longer at higher levels next to the main column (Fig. 5.6, top right), which is why the width of the modeled flume is reduced to 1.5m.

For the tripod model a tetrahedral mesh is used because of the ability to adapt to the surface, i.e. at the pointed angles of the braces and at the pile sleeves. Mesh sizes in terms of edge length are adjusted to the wave breaking process and range
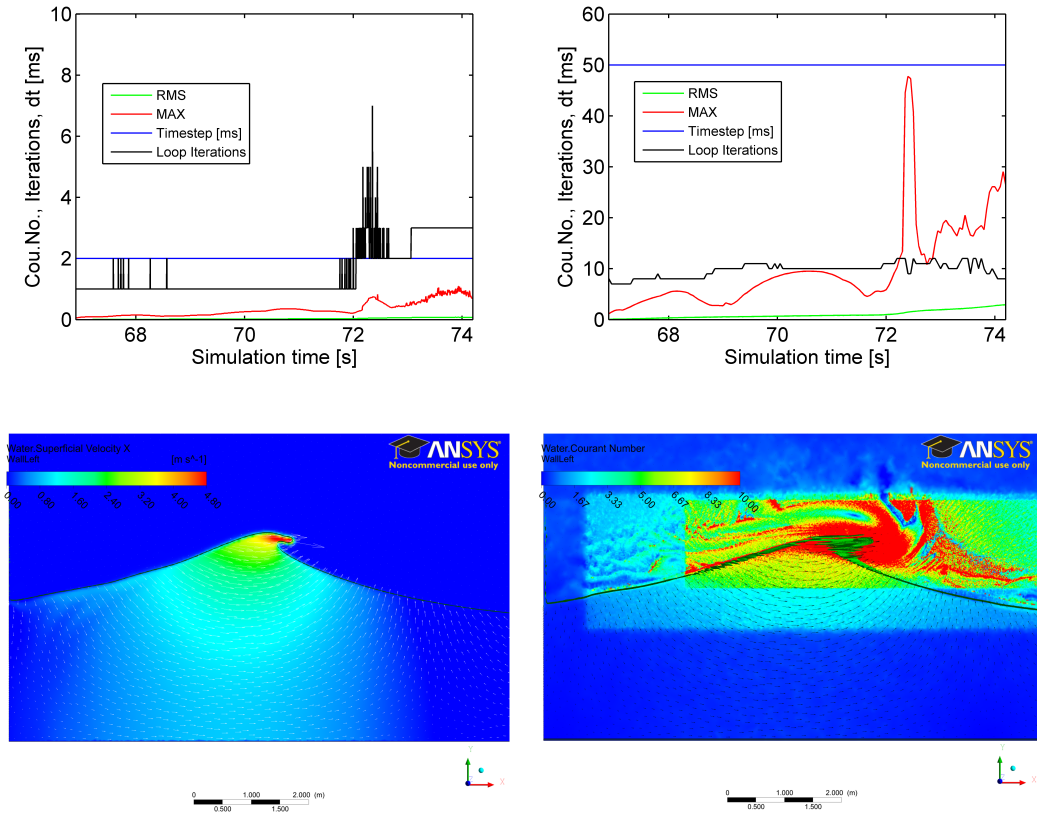
Figure 5.7: Illustration of converging (left) and not converging simulations (right) for the additionally displayed wave profiles. Green lines show the root mean squared Courant numbers (RMS), red lines the maximum Courant numbers (MAX), blue lines the time step size, and the black line the loop iterations.

between 1 cm in the impact area up to 10 cm for insignificant regions above the wave profile. Fig. 5.6 (left) illustrates several used mesh densities and the coarse mesh is visible on the top left above the wave crest up to the top of the domain. Elements ≤ 3 cm are used along the propagating wave crest, especially behind the point of the over curling wave tongue. Mesh sizes smaller than 1 cm are applied onto as well as around the cylinder in the vicinity of the wave impact (Fig. 5.6). This area is characterized by high gradients of pressures, velocities, wall shear stresses, and iteratively adapted by means of previous case studies.

Regions with high mesh densities increase the computation times in two ways, which is the high number of nodes itself, but also the effect on prism layers. Last mentioned are stepwise inflated parallel to the surface mesh until the boundary layer is sufficiently resolved and therefore significantly contribute to the global mesh size. The tripod is meshed by 3 cm elements outside the impact area and distant flow regions to the wave crest are meshed by 5 - 8 cm elements under the wave. For comparison purposes specific numbers are given with reference to the breaking wave

height of 1.46 m in this case. The impact is then resolved by more than 146 nodes per breaker height since the vertical element height is smaller than the element edge length. The wave crest region is resolved by more than $\approx$ 50 nodes per breaker height and underlying regions by 20 - 30 nodes per breaker height.

Calculation times for the wave impacts in the three-dimensional model depend on the used mesh densities in conjunction with adequate time steps as well as on the targeted residues. Relatively small meshes without prism layers and simulation durations of about 5s are calculated in less than 24h by 12 CPUs, while the large meshes with up to 8s simulation time took nearly one week with 24 CPUs. Small time steps are required in order to keep the residues and numerical stability, even tough CFX uses implicit solver. In contrast to the explicit method with Courant numbers $\leq$ 1, numerical stability in CFX is usually maintained up to Courant numbers $\leq$ 5. Fig. 5.7 gives an example of a stable and converging run on the left side next to an unstable run on the right side. Both cases use the same mesh, are limited to 12 loop iterations (shown by the black line), and show the same modeled wave. The left side is calculated with constant time steps of 0.002 s and the other case with constant time steps of 0.050s, as indicated by the blue lines. Both cases have root mean squared (RMS, green line) Courant numbers below five through out the simulation. However, the simulation on the right does not converge and often reaches the maximum number of iterations. As a consequence the maximum Courant number given by the red line nearly increases up to 50, while the other case barely exceeds 1. The two additional snapshots show the wave profiles at 72.5s for the high Courant number. Red colored regions indicate Courant numbers higher than 10 in the right plot and are predominately located near the wave crest with the highest water particle velocities. A diffuse wave crest is seen on the right side in contrast to the sharp profile of the developing wave tongue on the left. The settings of the last mentioned case are used for the impact simulations described in the following.

5.3   Validation of the impact model

The setup of the numerical model is validated by comparison of water level and pressure data with measurements from the large wave flume experiments, as also described with less details in Hildebrandt and Schlurmann (2012a). Out of the first three physically tested breaking waves (Chapter 3.2) load case 2 provides the best reproducibility with relatively low standard deviations of the averaged pressure time series in the region of wave impact, as concluded in chapter 4.4.3. All load cases show

small standard deviations for the pressure signals outside the impact area as well as for the wave gauges. However, load case 1 is characterized by strong pressure fluctuations near the impact area due to the highly turbulent mixture of air and water. In contrast to that load case 3 is defined by a sharp wave profile with almost no air entrapped. Even though, marginal variations of the vertical wave profile generate strong pressure deviations near the wave crest and complicate the local comparison of pressure measurements to the numerical model. Therefore, load case 2 is presented in the following in combination with the same numerically simulated load case. Comparisons to the other load cases including data analysis of wave gauges, velocity meters, as well as pressures inside and around the corresponding impact areas are further described in chapter 6.

The right plot in Fig. 5.8 illustrates the records of three wave gauges of load case 2 positioned at the main column of the tripod as well as 2m and 4m in front of it. The data shows the water elevation over time whereby the solid lines represent the numerical model and the dashed lines experimental data from the large wave flume. The maximum water elevation slightly decreases with decreasing distance to the tripod because of the curling and thus, downward falling, wave crest. Principally, all three time series are in good correlation and the wave gauges of the simulation reproduce the measured results with sufficient accuracy. Minor differences are detectable between the preceding trough and at the wave crest of the 1.46m high wave. On the one hand the deviation might be caused by small variations of the breaking wave front in the laboratory as well as entrapped air in the wave crest, which affects the wave gauge records near the wall of the large wave flume. On the other hand the numerical results are only approximated solutions of the real physics and thus imply uncertainties as well.

In addition to the wave gauge data the left plot in Fig. 5.9 compares three time series of the hydrodynamic pressures measured at the tripod. The positions of the sensors are located 0.71m, 1.12m and 1.73m below the mean sea level and indicated by the arrows in Fig. 3.3 (left). Due to the highest hydrostatic pressure the top time series represents the lowest pressure sensor and vice versa. In contrast to the wave gauge records, these results are not affected by air bubbles. Again, the simulations agree well with the test data, seen by the wave profile fitting over the whole wave period in terms of steepness, minimum and maximum values. However, the pressure sensors beneath the water column do not accurately detect the slight but significant changes in the shape of the wave tongue so that additional pressure sensors at higher elevations are used to compare further details from experiments and simulations.
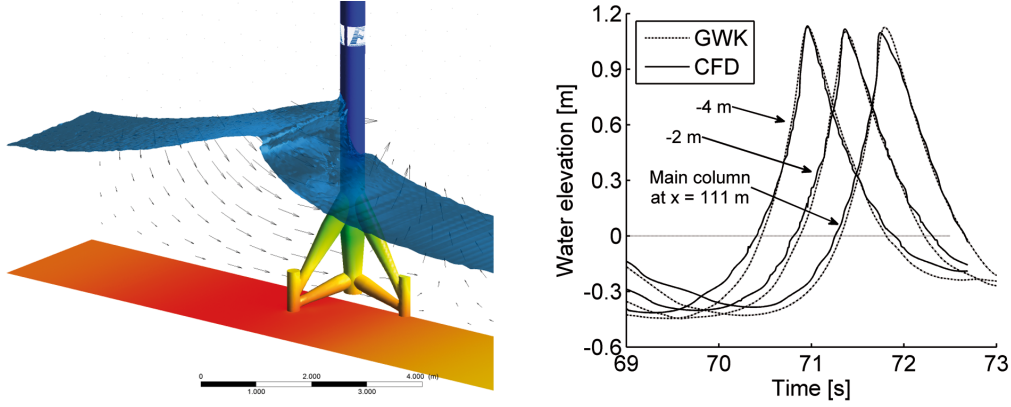
Figure 5.8: *Wave impact on the tripod structure with indicated velocity vectors in the CFD model (left) as well as wave gauge records of the developing breaking wave in the large wave flume and in the numerical model at three positions near the cylinder.*
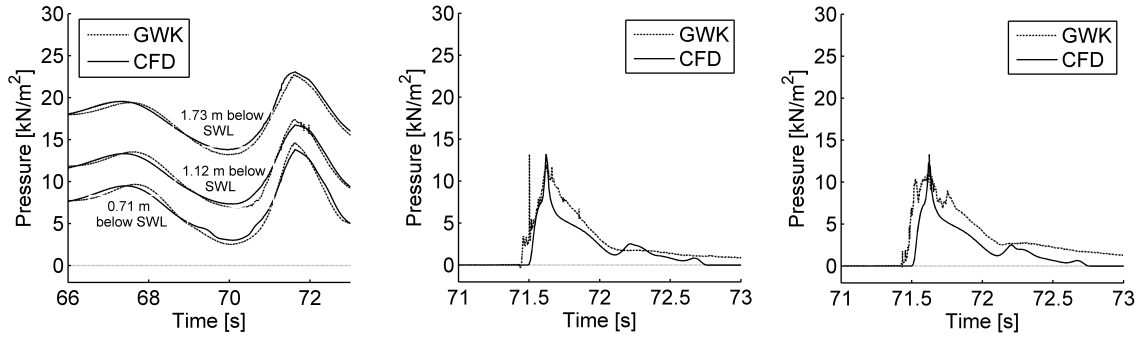
Figure 5.9: *Time series comparison of hydrodynamic pressures in the substructure of the tripod (left, and indicated in Fig. 3.3 by arrows) as well as in the relative height z/eta_{max} = 0.62 at the perimeter angle 0° (middle) and 20° (right). Solid lines show data from the CFD model and dashed lines GWK measurements.*

Two exemplary plots show the pressure time series in a relative height z/η_{max} = 0.62 in the middle and on the right in Fig. 5.9, which is located shortly under the impact area. The solid lines illustrate the numerical calculations analogous to the comparisons above, while the dashed lines show the average of five pressure signals with the main column in zero degree orientation (middle plot) and the average of four equally generated test waves with 20 degrees orientation on the right. Basically, both orientations show good agreements of simulated and tested pressure data, only with a small time shift after the peak value. The numerical results match the maximum experimental pressures of nearly 15 kN/m^2 as well as the rising times. Small differences between the time series are observed with regard to high frequent fluctuations, which are only present in the experiments due to the entrapped air in the wave crest. As mentioned above, these fluctuations are of minor importance in this load case and have more influence on the pressure records of the broken

wave. The maximum pressures last a bit longer under the wave crest in the physical model than in the numerical model. In addition to numerical reasons the signals also deviate due to variations of the bow wave in both models, which occurs on the front side of the cylinder due to the rapidly rising water level connected to the steep approaching wave front. As previously observed by the wave gauge records in Fig. 5.8 (right) and by the pressure measurements below the still water level in Fig. 5.9 (left) the full wave period and pressure amplitudes of the physically and numerically modeled breaking waves are nearly similar. The additional comparison of local pressures at higher levels underlines the validity of the numerical model up to the lower boundary of the impact area. Furthermore, the following chapter with details on the developing pressures in the impact area illustrates the reproducibility of the breaking wave by the numerical model as well, even though differences are present. In addition, the time dependent total forces are in good correlation, too, which indicates the validity of the integrated pressures on the whole numerical tripod and is also described in the following chapter.

6 Analysis part II: Impact pressures, forces, and hydrodynamics

This chapter combines analysis and results of both, large wave flume experiments as well as simulations with different types of wave breaking. Measurements and numerical results are compared and discussed to continue the validation for the impact area and to evaluate differences, as mentioned before in chapter 5.3. The first section is about the pressure development of impact areas due to various wave breaking distances in front of the tripod. The temporal and spatial characteristics of each load case are described with special attention to the peak values. Afterwards, the previously described advantages of the numerical model (Chapter 5) are used to derive local and total forces and to extract details on the hydrodynamics.

6.1 Pressures due to breaking waves

As concluded in chapter 4.4.3, load case 2 is predominantly used for the validation of the numerical results to the large wave flume measurements and is therefore described first. Subsequent to load case 2 the other experimental load cases are compared to the respective numerical results in the same way. Note that the wave impacts of LC 1 and 3 are not modeled with boundary conditions taken from quasi two-dimensional simulations of the focusing wave packets, as for LC 2. Instead, the tripod is shifted back and for with regard to the wave breaking position to model different load cases. This procedure is advantageous in comparison to the fixed cylinder with shifting focusing points in the large wave flume, since the wave shape remains the same for all cases. Thereby the only changing parameter is the distance to the wave breaking, while the wave height, wave period, and wave asymmetry is reproduced in the numerical load cases. As pointed out in chapter 3.3 and shown in Fig. 3.6, the wave parameters vary in the physical model due to the wave generation and due to the permanent changes of the transient wave itself.

Figure 6.1: Comparison of normalized impact pressures from large wave flume experiments (GWK) and from numerical simulation (CFD) for LC 2 at relative time steps $t/T_i = t/(R/c)$: 0.01 (a), 0.03 (b), 0.05 (c), 0.10 (d), 0.15 (e), 0.20 (f), 0.25 (g), 0.35 (h), 0.45 (i).

6.1.1   Development of impact regions

Fig. 6.1 shows plots of the pressure distribution at the main column of the tripod structure. Slamming loads are symmetric to the span of the cylinder at the perimeter angle zero, which is why the results from the large wave flume (GWK) experiments are shown on the left side in direct comparison to the CFD results on the right side for each subplot. The abscissa shows the perimeter angle of the cylinder up to 50 degrees to both sides and the ordinate represents the vertical relative height z/eta_{max}. Last mentioned is defined by the vertical coordinate z, zero at the still water level, divided by the maximum water elevation η_{max}. The measured pressures are normalized to the stagnation pressure, given by the water density ($\rho = 1000$ kg/m^3) multiplied with the squared wave celerity (c = 4.8m/s), which is estimated from the experiments in section 3.3. The time shifts between the plots are referenced to the time of immersion T_i defined by the duration the wave crest takes to submerge the cylinder's front half. This is calculated by the phase velocity of the wave c divided by the radius R of the cylinder. The first contact of the wave tongue with the cylinder front sets the point of time $t/T_i = 0$, while $t/T_i = 1$ refers to the submerged cylinder front up to the center line by the wave tongue.

Plot a) in Fig. 6.1 shows the pressure distribution around the main column of the tripod for load case 2 shortly after the wave tongue has encountered the cylinder ($t/T_i = 0.01$). The tongue of the slamming wave hits the cylinder at the level of the wave crest ($z/\eta_{max} = 1$) in both models and the pressure is roughly 1 ρc^2 at the cylinder's span. Subsequently, the pressure horizontally spreads up to 30 degrees across the perimeter in the CFD model within 10% of T_i (plot d). The impact area nearly remains constant in vertical direction during that time and values higher than 0.8 ρc^2 only occur between $z/\eta_{max} = 0.9$ and 1.1. This initial and horizontal spreading is connected to the immersion of the hitting wave tongue. However, the wave shape in the physical experiment is not strictly two dimensional as can be seen in the snapshot of load case 2 in Fig. 3.4. The wave breaking starts at the channel walls and propagates to the middle of the flume. Furthermore, the wave tongue also consists of single droplets and entrapped air in contrast to the more idealized tip of the wave tongue in the CFD model. This is why the impact of the more naturally breaking wave in the physical model shows several spots of fluctuating pressures at the upper section of the cylinder between 0° and 30° (plots a-d). Nevertheless, the pressure spots in the experiments and the CFD results show comparable intensity: Between 0.15 and 0.25T_i the pressure becomes more intensive and spreads from 0° up to 25° in both models (subplots e - g). Pressures up to 1.5 ρc^2 are reached in the CFD model for t$/T_i = 0.2$ (plot f) in comparison to a maximum value of 1.7ρc^2 in the physical model tests. Higher differences are observed for t$/T_i = 0.25$ (plot g) with maximum CFD pressures of 1.7 ρc^2 in contrast to 3.5 ρc^2 recorded in the laboratory tests. Further comparison of the impact area at various time steps shows that the intensive pressure field in the CFD simulation generally exceeds the area covered by high pressures in the experiments. Impact pressures obtained by the CFD simulation and values greater 1 ρc^2 cover the cylinder span up to 30% of the maximum water elevation η_{max} (plot g). Later on, the impact region becomes narrower again at high perimeter angles and extends approximately along 20% of η_{max} with reduced pressures around 1c^2 (plots h, i). The impact pressures observed by the laboratory tests stretch over 30% of η_{max} along the cylinder front as well, however, do not occur at higher angles than 30 or 40 degrees (plot g-i). As already seen at the initial stages of the wave impact, the measured pressures at later stages with $t > 0.35$ T_i show fluctuations as well, although less dominant as before (plots h, i).

With regard to the validation of the numerical model, the maximum differences between the physical and numerical results are found in the upper section ($z/\eta_{max} > 0.62$) of the main column in the vicinity of the hitting wave tongue. On the one hand the models differ by the outer extension of the impact area and by the
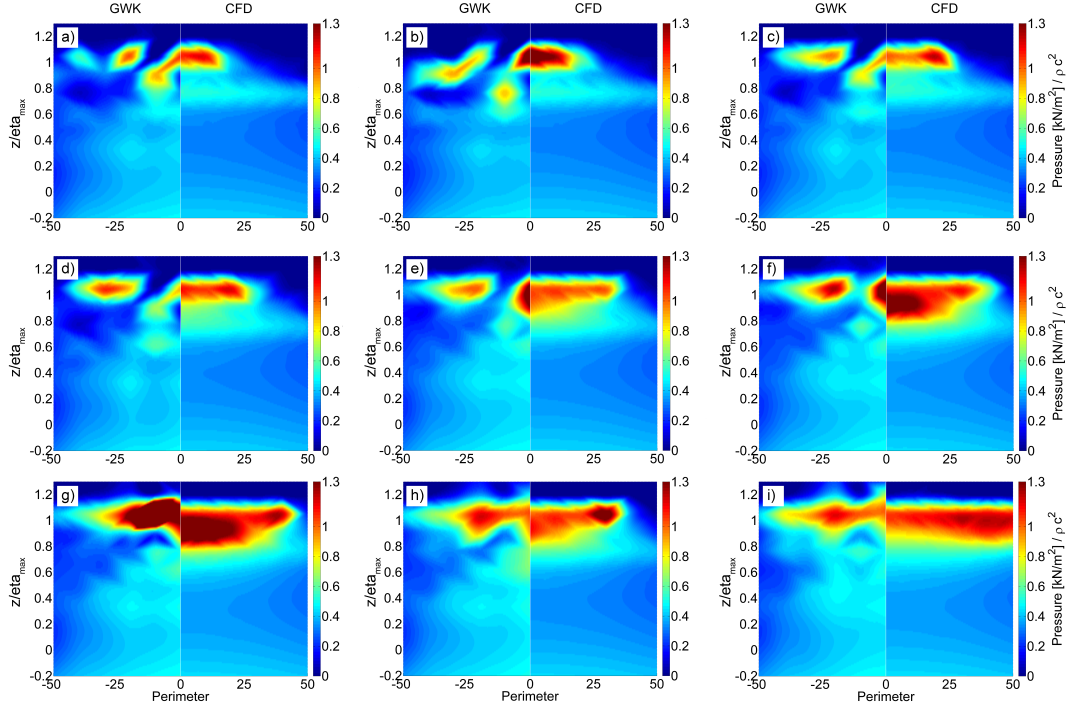
Figure 6.2: Comparison of normalized impact pressures from large wave flume experiments (GWK) and from numerical simulation (CFD) for LC 1 at relative time steps $t/T_i = t/(R/c)$: 0.02 (a), 0.20 (b), 0.40 (c), 0.50 (d), 1.60 (e), 1.70 (f), 2.30 (g), 2.35 (h), 2.65 (i).
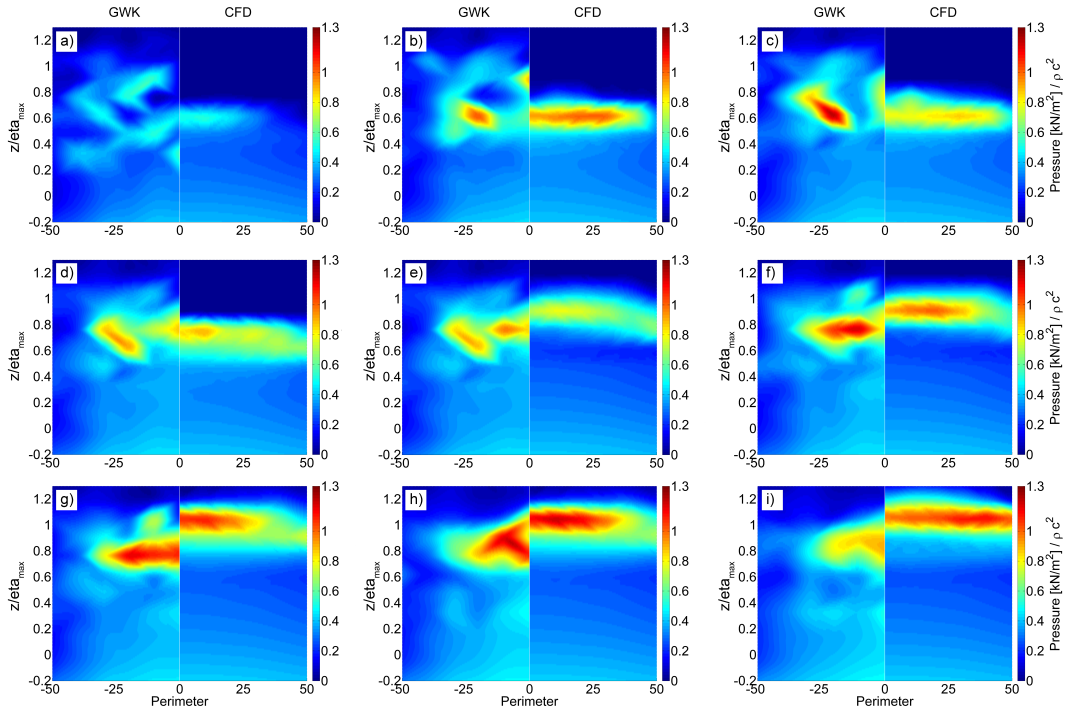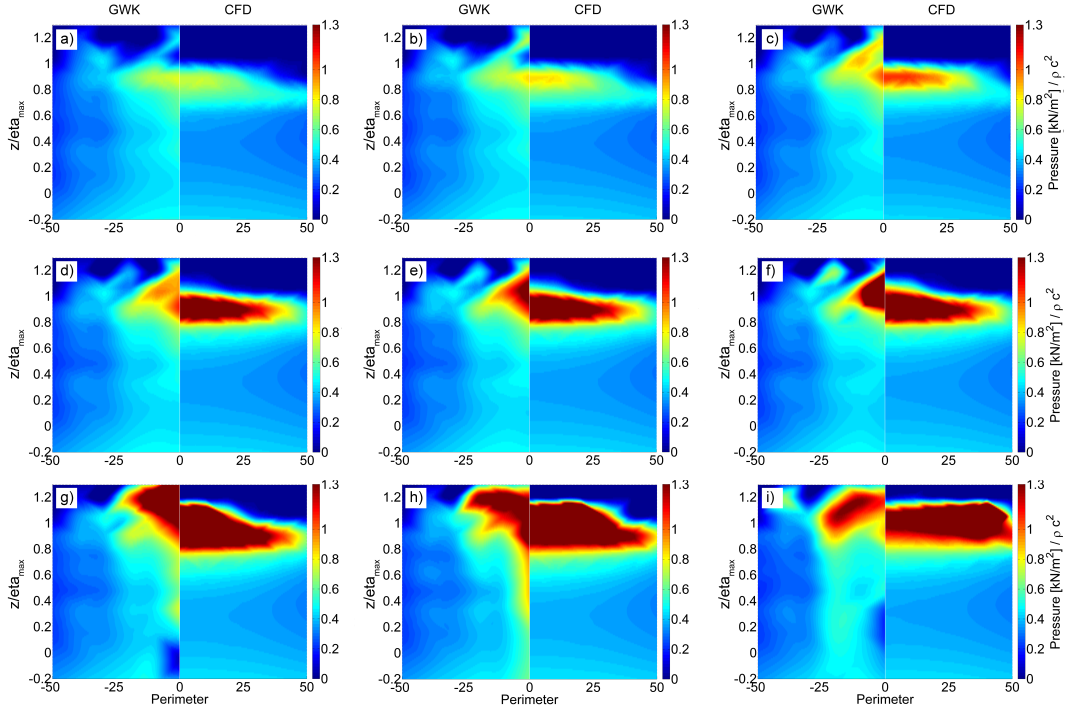

Figure 6.3: Comparison of normalized impact pressures from large wave flume experiments (GWK) and from numerical simulation (CFD) for LC 3 at relative time steps $t/T_i = t/(R/c)$: 0.02 (a), 0.05 (b), 0.10 (c), 0.23 (d), 0.24 (e), 0.25 (f), 0.30 (g), 0.35 (h), 0.42 (i).

under prediction of the local maximum value at $t/T_i = 0.25$ in the CFD model. On the other side the time dependent spreading of the impact in combination with the vertical positions along the cylinder's span, as well as the pressure intensities are in good agreement and demonstrate the good approximation of the numerical model to the experiments. In addition to the pressure and wave gauge data compared so far, total forces on the tripod structure as well as velocities are recorded in the experiments and used for validation in sections 6.2 & 6.3, respectively.

As can be seen in Fig. 6.2 the impact region due to the broken wave of load case 1 differs in several ways to the previously described pressure distribution caused by the curled wave tongue. The broken wave front encounters the cylinder at a lower level around $z/\eta_{max} \approx 0.6$ and less intense, as seen in the plots a) - c). Both, the experiments as well as the numerical simulation show pressures $\leq 1c^2$ during the first 20% of the cylinder immersion, whereby the GWK pressures appear randomly distributed along a broader vertical width in comparison to the rather slim wave tongue impact in the numerical model. This is mainly reasoned by the highly turbulent wave front in the experiments with large amounts of air entrapment, as shown and described in chapter 4.3. After 0.4 T_i (plot c) the pressure becomes weaker and tends to move upward at the cylinder front until 1.6 T_i. This effect is more obvious in the CFD simulations, since the pressures in the experiments are strongly influenced by air dynamics and therefore scatter in intensity until the wave crest reaches the main column at 1.7 T_i (plot f). Even though the spatially averaged magnitude of the normalized pressures is in acceptable agreement, in the experiments the second impact appears ≈ 0.1 z/η_{max} lower and reaches $z/\eta_{max} \approx 1$ roughly 0.75 T_i later. Furthermore, the impact area exceeds up to 50 degrees in the numerical model in contrast to the intensive pressures $\leq 30 - 40$ degrees observed from the tests. Nevertheless, both models show correlating maximum pressures around $1.2c^2$ at similar times as well as two noticeable areas at $z/\eta_{max} = 0.6$ and 1.

Load case three is characterized by a single and intense impact at high levels with a duration of ≈ 0.4 T_i. Both models show the onset of slamming on a level $z/\eta_{max} = 1$ (plot a - c) and the impact area rapidly spreads on the cylinder surface. Again, the CFD model extends to higher perimeter angles around 50 degrees, while the slamming area of the GWK tests is localized between 0 and 20 - 30 degrees (plots f-h). The vertical size of the impact area covers approximately 30% of the crest height (0.3 η_{max}) at 0.3 T_i in both models (plot g). Remarkable is that both models reveal a relatively moderate pressure development with noticeable rising times around $z/\eta_{max} = 1$ before the pressures rapidly escalate within 2% T_i (plots d-f). This might be anticipated to some extend for the averaged pressures of the experiments, however,

Figure 6.4: Measured peak pressures (first row), the corresponding standard deviations (second row), and maximum pressures from CFD simulations for LC 1. The columns from left to right represent the perimeter angles 0, 20, and 40 degrees, respectively.

the CFD results are not affected by averaged cases and show similar characteristics. The maximum pressures at the cylinder span amount nearly $4c^2$ in the physical model and $3.5c^2$ in the CFD model, which is described in more detail in the next section.

6.1.2 Values and positions of peak pressures

Fig. 6.4 to 6.6 show plots of the peak pressures from experiments in the first row, the corresponding standard deviations in the second row, as well as the maximum pressures from CFD simulations in the third row. Each Fig. displays a load case

Figure 6.5: Measured peak pressures (first row), the corresponding standard deviations (second row), and maximum pressures from CFD simulations for LC 2. The columns from left to right represent the perimeter angles 0, 20, and 40 degrees, respectively.

and all pressures are normalized by the stagnation pressure ρc^2 based on the wave celerity c, while the ordinates mark the relative heights z/η_{max} of the pressure sensor positions. In the first row the solid lines show maximum peak pressures calculated from averaged time series (indexed by "mean signal"), which are synchronized to each other as described in chapter 4.1. The dashed lines are calculated from the individual pressure peaks (indexed by "mean peaks") and are independent of synchronization procedures. Values from measurements or simulations are highlighted by the x- and o-markers, while the lines are cubic spline curves. The columns from left to right correspond to the perimeter angles 0, 20, and 40 degrees at the cylinder front. The CFD based plots in the last row differentiate between simulations

including prism elements for the boundary layers (indexed by "prism") and between free slip conditions (chapter 5.1.1).

Load case one is characterized by the lowest mean peaks and by the broadest impact range along the cylinder's span. Maximum mean peaks of approximately $2c^2$ are observed by the experiments for the zero degree orientation, which decrease to $\approx 1c^2$ at 40 degrees. The range of moderately increased values $\geq 1c^2$ remains constant around the cylinder and covers approximately 0.5 to 1.0 η_{max}. This range is also indicated by increased standard deviations with almost equally high values as the pressures itself, whereby no significant differences are noticeable between the two types of averaged peaks. Similar characteristics and a maximum value of roughly $1.5c^2$ are observed for the numerical simulations, however, the lower limit of the increased pressures is located at ≈ 0.7 η_{max} and the peak pressures are less decreasing along the perimeter. The peak pressures of the simulations with and without the prism layer are in good agreement.

Load case two is characterized by higher peak pressures within a smaller range along the cylinder span in regard to load case 1. Maximum mean peaks of approximately $3c^2$ are visible in the first row of Fig. 6.5 for the zero degree orientation, which decrease to $\approx 1c^2$ at 40 degrees, likewise to load case 1. The width of the impact is about 0.2 η_{max} at the cylinder's front and increases up to 0.4 η_{max} at 40 degrees, as well as the range of standard deviations ≥ 1. Likewise to load case 1, the two types of averaged pressure peaks have similar values as well as the corresponding standard deviations. The numerically estimated impact area shows nearly the same positions along the vertical span as well as the development along the perimeter. The maximum value of $2c^2$ is slightly lower in comparison to the experimental one and the simulations including prism layers show marginal reduced pressure peaks.

For load case 3 the width of intensive peak pressures describes a pointed shape along the perimeter, which ranges along 0.3 - 0.4 η_{max} around z/η_{max} = 1 at zero degree and reduces to 0.2 η_{max} at 40 degrees while shifting upwards to a level around 1.1 η_{max} (Fig. 6.6). The highest averaged peaks of $5c^2$ are observed on a level with the wave crest z/η_{max}, which reduce to $2c^2$ at 40 degrees. Similar pointed shapes to the one mentioned above are found for the positions of the increased standard deviations as well as for the peak locations in the numerical simulations. In this case the simulation including the resolved boundary layer shows differences to the one without prism mesh. The peak value for the prism case is clearly reduced at perimeter angles greater 20 degrees and correlates acceptable to the measured peaks in contrast to the over predicted pressures by the simulation with free slip wall conditions.
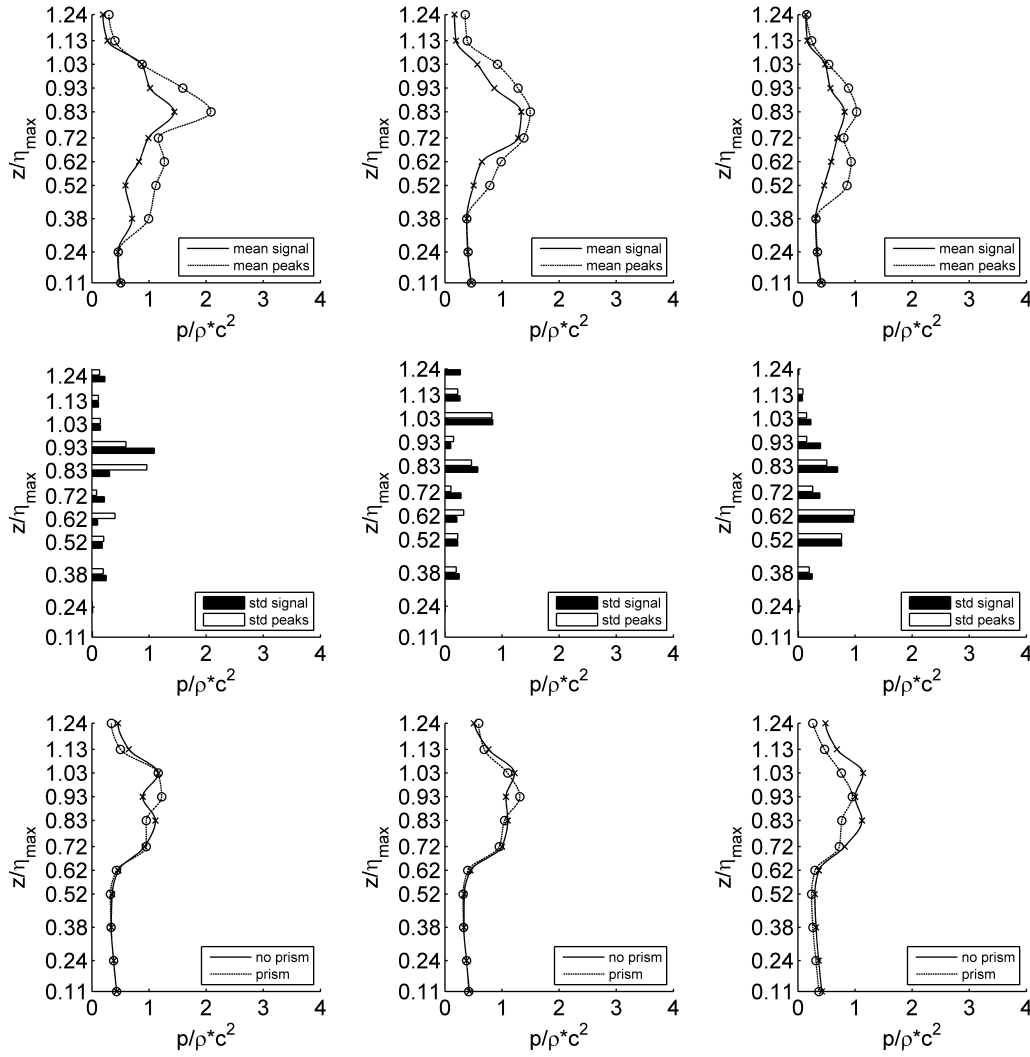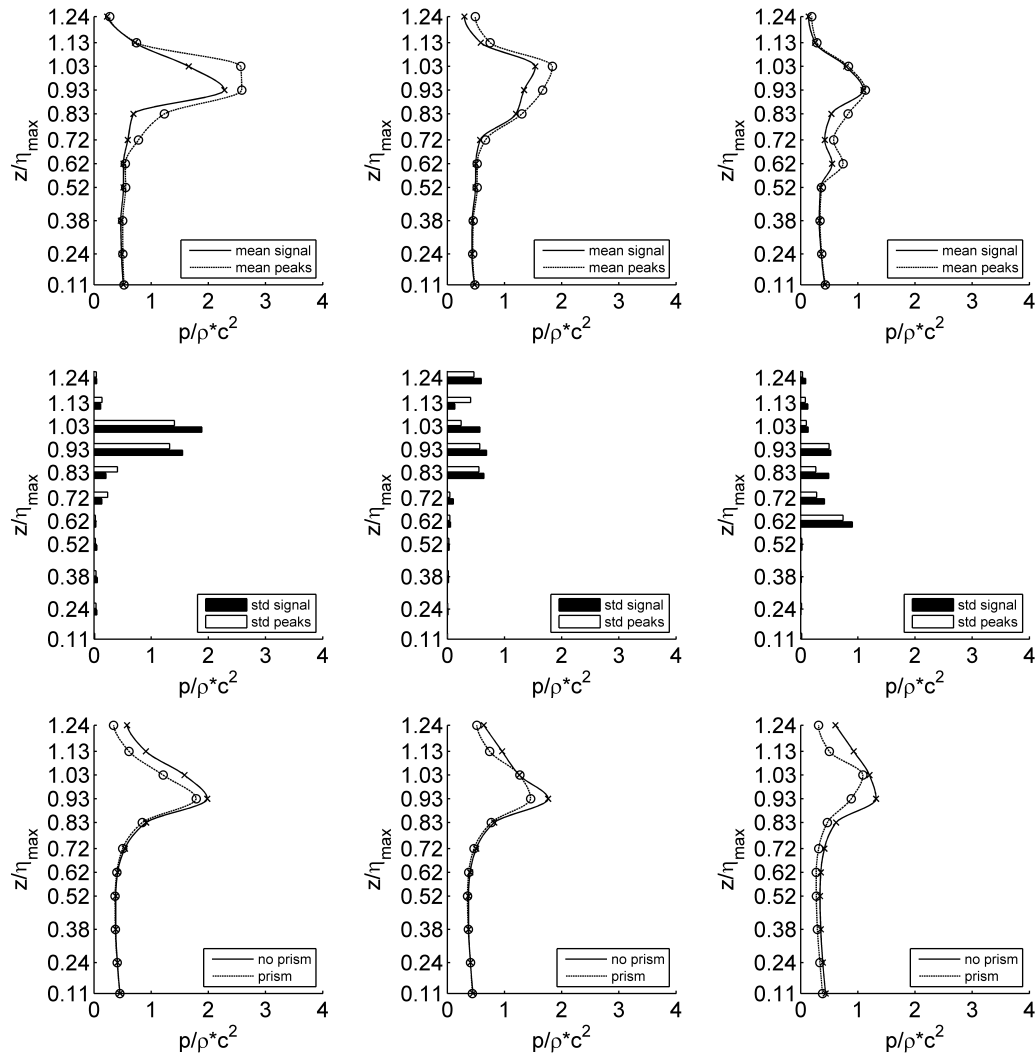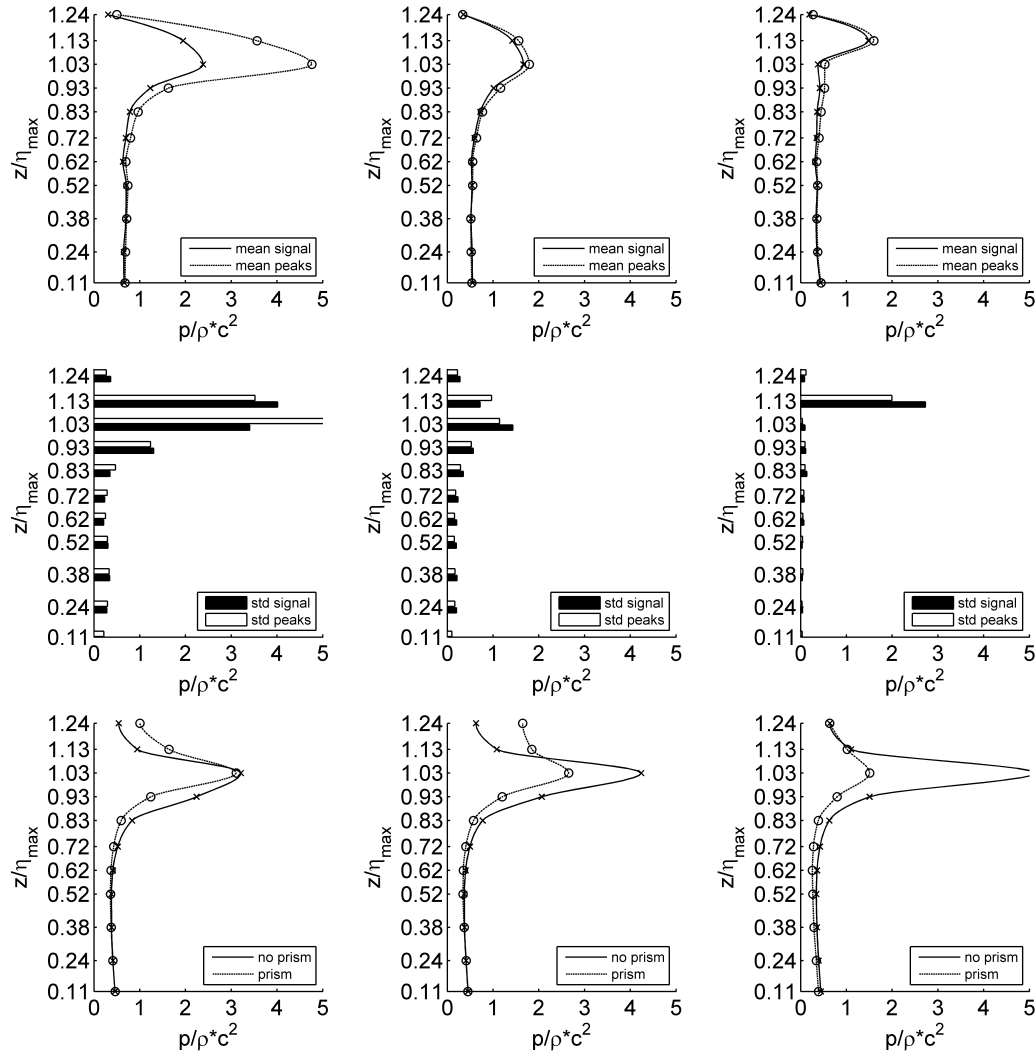
Figure 6.6: Measured peak pressures (first row), the corresponding standard deviations (second row), and maximum pressures from CFD simulations for LC 3. The columns from left to right represent the perimeter angles 0, 20, and 40 degrees, respectively.

Fig. 6.7 shows the maximum normalized pressure at the cylinder's span estimated from all experiments. They are given for comparison reasons even though single slamming experiments provide a very limited validation to draw conclusions on impact pressures. The overall shape of the individual peaks agrees with the observed pressure distribution of the averaged values. Again, the lowest peaks of $4c^2$ are measured in load case 1, followed by slightly increased records of $5c^2$ at higher elevations for load case 2. Finally, load case 3 shows the highest impact pressure of $12.5c^2$ on a level with the impinging wave crest.
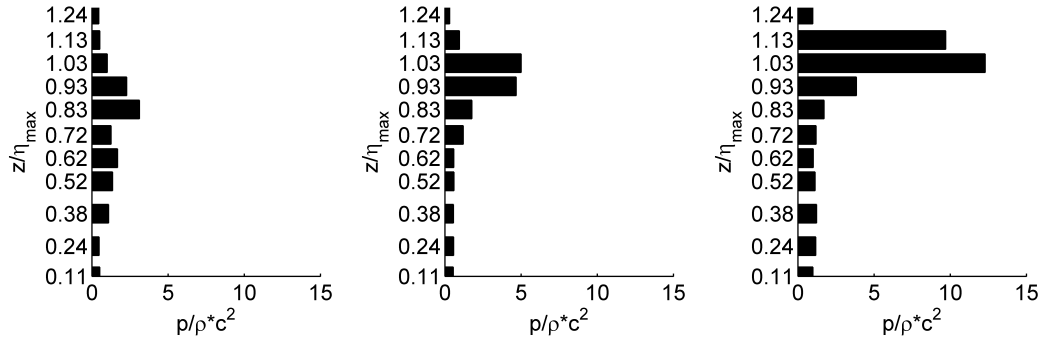
Figure 6.7: Measured normalized pressure peaks versus relative heights z/eta_{max} at the cylinder span for load cases 1 - 3 from left to right, respectively.

6.2   Forces due to breaking waves

Wave forces resulting from the previously described slamming pressures are of special interest for engineering purposes, since the applied forces are decisive of the dimensions and materials of construction elements. In addition, dynamic forces are usually required for the design of elements sensitive to certain levels of acceleration or displacement, i.e. the motion of nacelles of offshore wind turbines due to wave impact, also know as "ringing effect".

In the experiments, the total forces on the tripod are indirectly measured by strain gauges (chapter 3.1) positioned shortly under the mud-line at the sub-structure. They are compared to the total forces derived from numerical simulations and are described in section 6.2.2. Due to the lack of pressure information on the backside of the cylinder and due to punctual pressure measurements at the tripod below the SWL, local forces are obtained from the validated numerical model, which is the focus of this section and partly published in Hildebrandt and Schlurmann (2012b). The numerical model offers detailed analysis of the highly time and space dependent impact forces described in the next section.

6.2.1   Local impact forces

Fig. 6.8 to 6.11 show temporally and spatially resolved slamming coefficients for the three illustrated types of wave breaking and the the non-breaking wave, which correspond to the snapshots 1 - 4 in Fig. 3.4. Abscissas show the relative time normalized by the previously described time of immersion (R/c) and the ordinates show the relative height z/η_{max} analogous to the plots above, ranging from zero at the still water level up to 1.6 times the position of the wave crest. Each point

Figure 6.8: Slamming coefficients of LC 1 over time normalized by the time of submergence (radius/wave velocity) and versus relative height "z/η_{max}" with water elevations at the cylinder's front (upper solid line) and rear side (lower solid line); the x-marker line shows the wave gauge unaffected by the structure for orientation.

shows a slamming coefficient for a specific point in time, which is defined by the local line force at the cylinder span divided by the line force commonly used in literature based on the stagnation pressure ($\rho R c^2$) with fluid density ρ. The line forces are calculated by the integrated pressures of the CFD model along the full circumference of the tripod's main column, while the constant reference value is the flow force induced by a steady flow with velocity c = 4.8m/s acting on the diameter of the main column ($2R = 0.5$m).

Furthermore, the solid white lines give the water level elevations on the front and rear side at the main column. Thereby the upper line gives the time dependent location of the bow wave before the impact and the wave run-up when the tongue encounters the cylinder. The difference between the upper and lower solid white lines shows the section along the cylinder with almost no water pressure acting on the backside. Fig. 6.11 is equivalent to Fig. 6.9 except the reduced limit of the colorbar to 0.5 for illustration purposes and indicates the absence of the supporting force by the red coefficients. The coefficients drop relatively fast from values > 0.45 - 0.5 down to 0.3 or 0.2 below the water level on the rear side. Since the water level decreases with a variable gradient along the circumference of the main column, the section without pressure on the backside is slightly smaller than indicated by the two local water levels. For orientation purposes the dashed lines illustrate the shapes of the breaking waves on a level with the cylinder front and without being influenced by the structure. Load cases two and three have explicit wave fronts in contrast to load case 1 with the broken wave, which is therefore illustrated by white
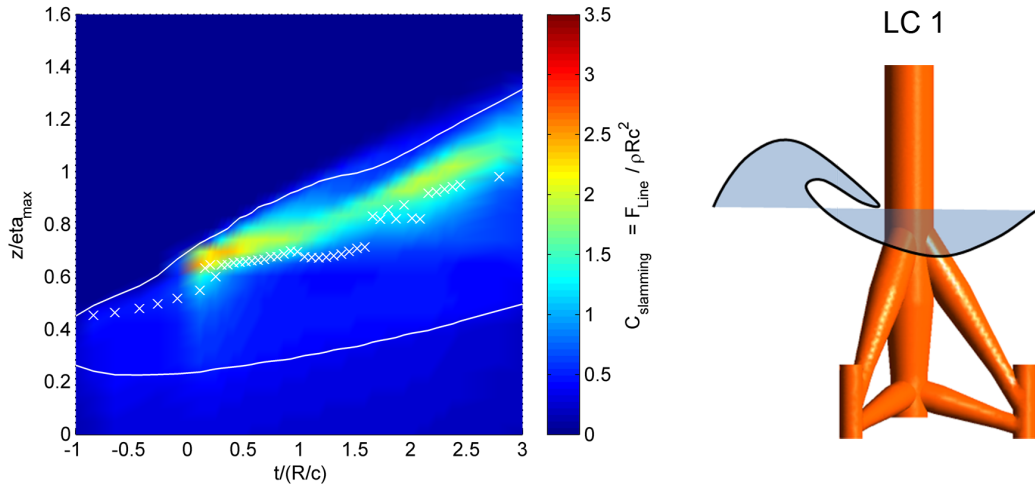
Figure 6.9: Slamming coefficients of LC 2 over time normalized by the time of submergence (radius/wave velocity) and versus relative height "z/η_{max}" with water elevations at the cylinder's front (upper solid line) and rear side (lower solid line); the dashed line shows the wave gauge unaffected by the structure for orientation.

x-marks. For all cases the time scales on the abscissas are set to zero at the point in time when the wave front contacts the cylinder front.

Load case one is illustrated in Fig. 6.8. The maximum slamming coefficient is C_S = 2.7 and represents the smallest value out of the three load cases. Two peaks of the coefficients are visible with a less intensive second peak ($C_S = 2$) at the relative height $z/eta_{max} = 0.9$ in contrast to the first one at the lower position $z/eta_{max} = 0.65$. These characteristics are connected to the broken wave front, which is less impulsive and encounters the cylinder at the lowest relative height due to the air water mixture and the downward falling wave tongue (Fig. 4.5). As a consequence, the vertical range of impact coefficients greater 1 is narrower than for the other load cases and located between $z/eta_{max} = 0.6$ to 1.1 as well as the curling factor < 0.2. Therefore, the rise time of the first peak with 0.25 T_i and the impact duration of 0.5 - 1.0 T_i at a specific relative height are longest.

Fig. 6.9 shows the slamming coefficients for the curling wave tongue encountering the cylinder at the relative height $z/eta_{max} = 0.95$ - 1 on a level with the highest water elevation ($z/eta_{max} = 1$) and $T_i = 0$. The wave tongue spreads upwards and downwards along the cylinder's span during wave propagation, which is why the free surface is defined by three values until T_i is approximately 0.6. Then, the rising wave front encounters the curled wave tongue from above and after $T_i = 0.6$ the wave crest passes the main column without a separated tongue, as indicated by
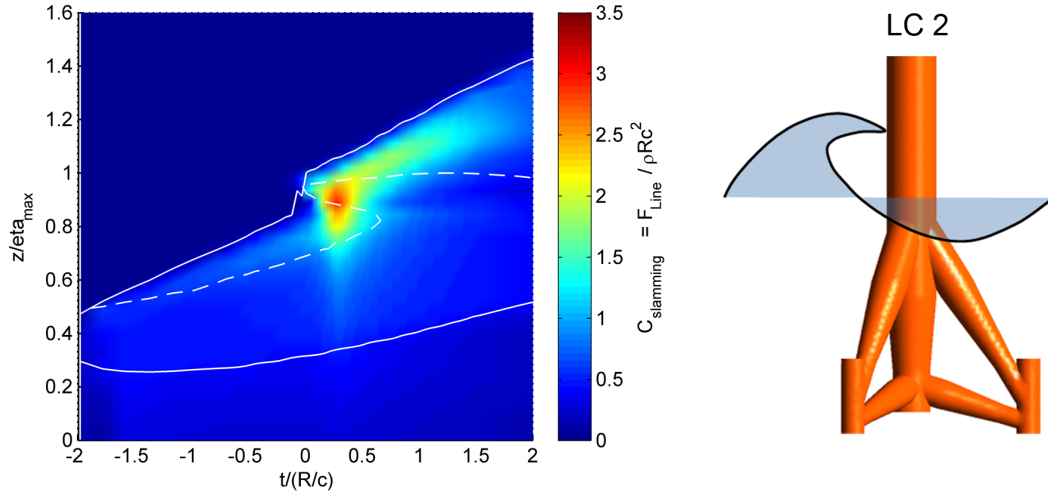
Figure 6.10: Slamming coefficients of LC 3 over time normalized by the time of submergence (radius/wave velocity) and versus relative height "z/η_{max}" with water elevations at the cylinder's front (upper solid line) and rear side (lower solid line); the dashed line shows the wave gauge unaffected by the structure for orientation.

the single dashed line. The maximum slamming coefficient for load case 2 is C_S = 3.0 at z/eta_{max} = 0.9 and lasts from T_i = 0.25 to 0.3 (Fig. 6.9). The impact area induced by the curled wave crest (LC 2) approximately ranges from z/eta_{max} = 0.7 - 1.2 when considering the whole impact time. This observation assumes that slamming characteristics in terms of sudden rise times and high force gradients are indicated by coefficients CS > 1, which exceeds the previously described flow force on the basis of the wave celerity. The simultaneously impacted area along the span (denoted as "curling factor" in literature) reduces to a relative width of 0.2 - 0.3, which is centered near z/eta_{max} = 0.9 at the early stages of slamming and shifts upwards to z/eta_{max} = 1.1 within 1.5 times of T_i.

Horizontal cross-sections through the coefficients represent time dependent forces at a specific relative height. Vertical cross-sections show the distribution of the line force along the main column for an arbitrary point in time. The vertical distribution of forces between T_i = 0 and 1.5 hardly shows sections with constant coefficients for load case 2. Observations around the maximum value reveal decreasing loads along the cylinder span from 3.0 to 2.0 within roughly 10-15% of the maximum water elevation. Similar results are found for vertical distributions after the maximum value and underline the variability of impact loads in regions C_S > 1. A horizontal intersection through the maximum value gives the time dependent characteristics before and after the maximum coefficient. At this level (z/eta_{max} = 0.9) the rising time is about 0.2 T_i and taken between the points of time with C_S = 1 until C_S = 3,
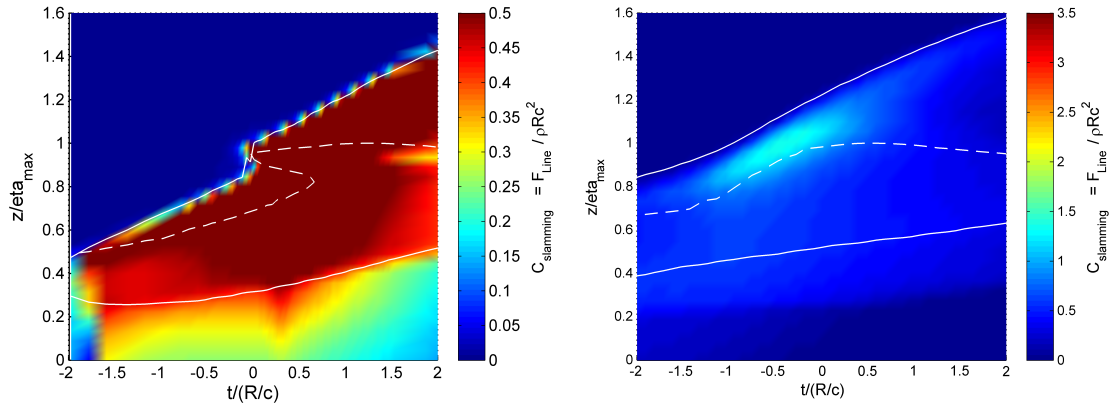
Figure 6.11: Left: Slamming coefficients of LC 2 analogous to Fig. 6.9 with empha-
sized coefficients of lower magnitude to classify between potential regions of slamming and
streaming forces.
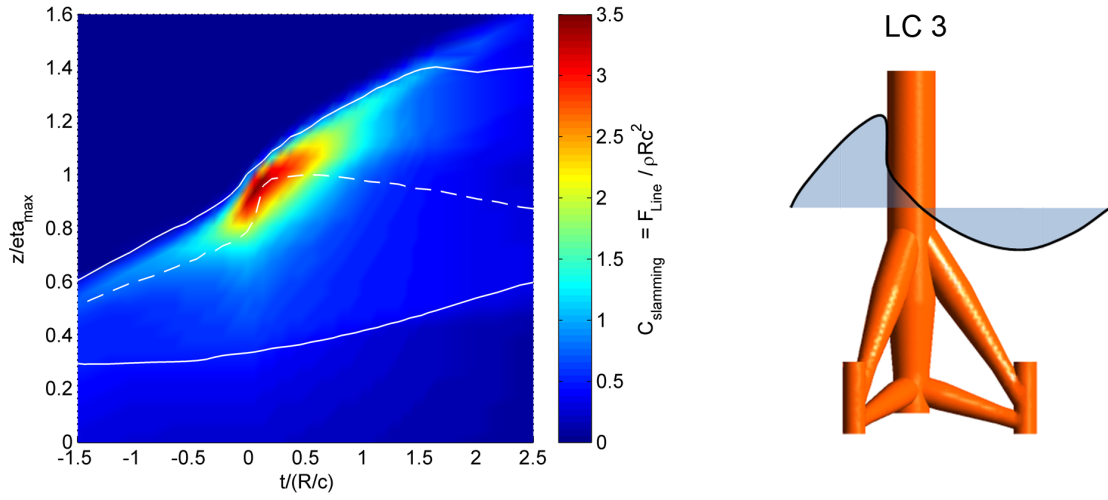*Right: Slamming coefficients of LC 4 over time normalized by time of immergence (ra-*
dius/wave velocity) and versus relative height "z/eta_{max}" with water elevations at the
cylinder's front (upper solid line) and rear side (lower solid line); the dashed line shows
the wave gauge unaffected by the structure for orientation.

while the decreasing time takes 0.3 T_i until $C_S = 1$ again. The slamming duration
of approximately 0.4 to 0.5 T_i for C_S values exceeding 1 is observed at all various
relative heights.

Fig. 6.10 illustrates the slamming coefficients for load case 3 with a vertical wave
front section of $\approx 0.2\ eta_{max}$ at the instant of impact. $T_i = 0$ is located right before
the steep inclination of the unaffected wave gauge record and matches with the
impinging wave front at the cylinder (Fig. 4.7). Pressures of load case 3 generally
exceed the pressures of load case 2 at locations up to 50 degrees along the perimeter
between $z/eta_{max} = 0.8$ and 1.1, as described in section 6.1.1 and illustrated by
figures 6.1 and 6.3. This leads to visibly higher load coefficients in this region
whereby the maximum value of $C_S = 3.5$ occurs at $z/eta_{max} = 0.9$ to 1.0 after a
rising time of approximately 0.1 T_i. In comparison to LC 2 the region of impact
loads spreads a bit wider along the cylinder front and ranges between $z/eta_{max} =$
0.7 and 1.3. Vertically distributed slamming characteristics are observed along 0.3
broad sections over time, whereby the center shifts from $z/eta_{max} = 0.85$ towards
1.1 within nearly 1 T_i. Similar to LC 2 the slamming duration lasts about 0.4 T_i
at each relative height and the loads vary along the cylinder's span as well as over
time.

The coefficients of load case 4 are illustrated in Fig. 6.11 on the right and demon-
strate the distributed forces for the non-breaking wave. The dashed white line shows

the smoothly propagating wave crest without indications of wave breaking. Again, the upper solid line illustrates the clearly visible wave run-up on the cylinder front, which is partly reasoned by the high wave steepness of the passing wave. The sunk on the rear side is indicated by the lower solid line and $t/(R/c) = 0$ corresponds to the maximum water elevation. In general, the coefficients range between 0.5 and 0.7 $\rho R c^2$ except in the vicinity of the wave crest level, where the coefficients increase up to $C_S = 1.2$ - 1.3 due to relatively high velocities and the onset of the wave run-up. This load case represents the contribution of the quasi-static loads to the local slamming forces of the breaking waves described above. The difference between this case and the figures 6.8 to 6.10 gives the isolated force components due to various breaker types. The isolated temporal and spatial varying coefficients could then be combined with commonly used methods of load calculations, i.e. the Morison equation with appropriate wave theories to estimate the quasi-static contribution for a specific wave independently.

6.2.2   Total forces on the tripod

The time-dependent total forces on the tripod structure are estimated from strain gauge measurements for the experiments and from pressure integration in the numerical model. Fig. 6.12 shows a sketch of the static system used for the calculation of the total force H_{tot} as well as the respective point of action labeled z. Mainly three load components with different, wave phase depending contributions are superposed in the strain gauge signals and illustrated in Fig. 6.12. The strain gauges are numbered (on the left below the tripod sketch) according to the numbers in Fig. 3.3.

For the case of the passing wave crest the first two components contribute to the total force, since vertical forces are nearly zero. Horizonal shear is induced by H_{tot} and distributed on the three vertical piles in combination with a tilting moment, which compresses pile B and strains the two piles A and C. Furthermore, vertical forces compress all three piles apart from the wave crest and especially during zero crossings of the water elevation. These components are distinguished and calculated by means of the two opposite strain gauges at each pile and the theoretical strain at the specific locations given by the following equation.

$$\sigma_i = \frac{(V_M + V)}{A} + \frac{M_y}{I_y} \cdot z_s \tag{6.1}$$
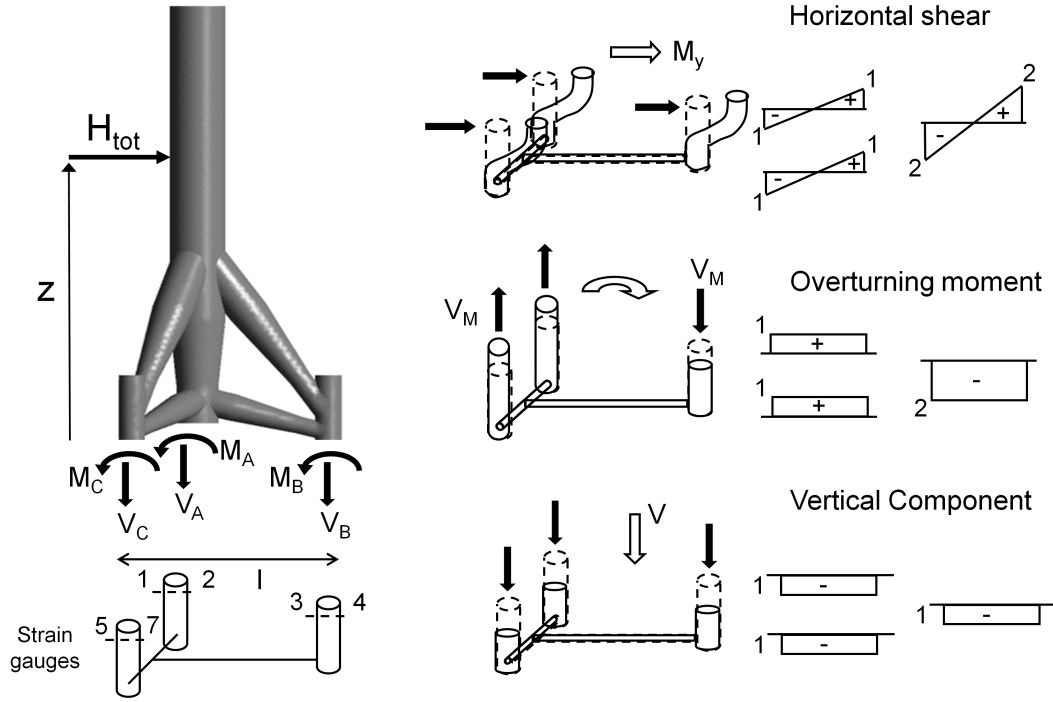
Figure 6.12: Balance of forces and superposed strain components for the tripod model in the large wave flume.

H_{tot} and z are calculated by the substitution according to the balance of forces:

$$\sum M : \quad H_{tot} \cdot z \; = \; M_A + M_B + M_C - V_B \cdot l \tag{6.2}$$

The total horizontal forces derived from the strain gauge measurements are checked for plausibility with regular waves. Waves with a height of 0.74m and a wave period of 2s were produced in the large wave flume during the tripod experiments, which are theoretically calculated by using Stokes 2nd Order theory in combination with the Morison equation. The time series based on the strain gauges are in good correlation with the theoretical forces.

Fig. 6.13 (left) shows the horizontal total forces versus time of the four tested load cases, which are time shifted by 1s for illustration purposes. Load case four is plotted as quasi-static reference next to the three wave breaking types. The force time series of the breakers are similar to the non-breaking wave before and after the impact at the crest. Rise times and the shape of the crest match the profile of the quasi-static case, except small variations due to the different wave periods derived from the zero down-crossing method, as described and illustrated in Fig. 3.6.
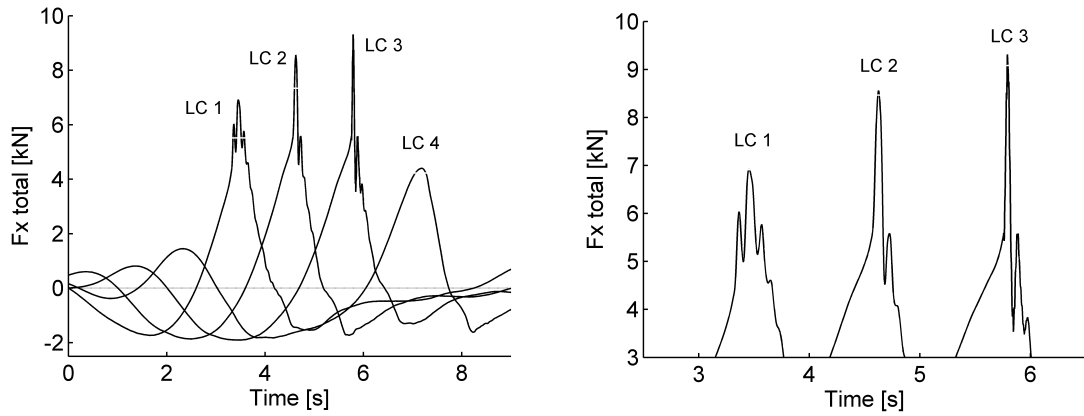
Figure 6.13: *Horizontal total forces of LC 1 - 4 versus time and shifted by 1 s to each other for illustration purposes.*
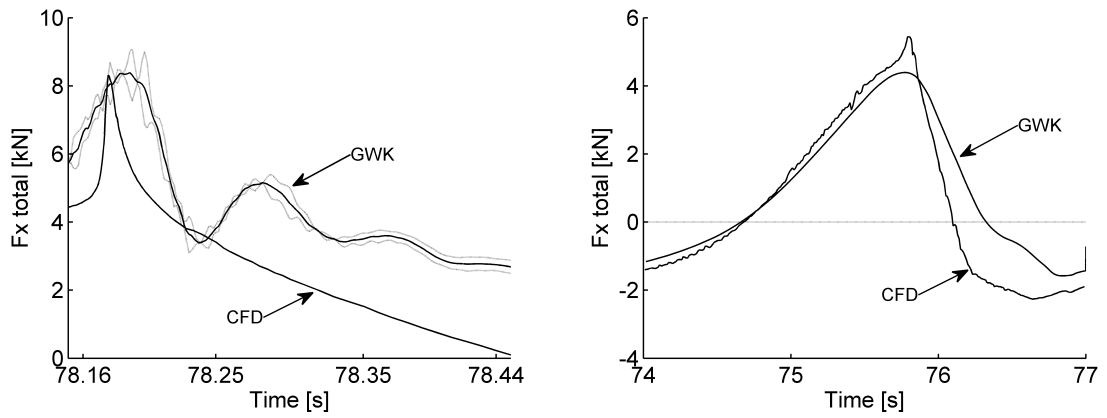
Figure 6.14: *Comparison of horizontal total forces derived from experiments and simulations versus time for LC 3 (left) and LC 4 (right).*

Figure 6.15: *Time variant positions of pointing total force F_x in regard to the still water level in combination with the water elevation η.*

Table 6.1: Maximum horizontal forces, ratios of impact and quasi-static loads, and positions of pointing maximum forces for LC 1 - 4.

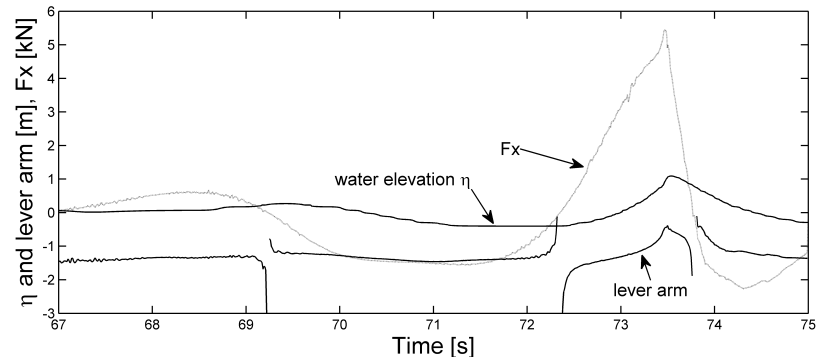| Load case	$F_{x,max}$ [kN]	$F_x/LC4(=5)$	$F_x/LC4(=4)$	Acting point at z/η_{max}
LC 1	6.0	1.20	1.50	-0.48
LC 2	7.9	1.58	1.98	+0.10
LC 3	8.3	1.66	2.08	+0.14
LC 4	5 & 4	1.00	1.00	-0.38

Fig. 6.13 (right) shows the details of the impact characteristics taken from the plot on the left. It should be note here that the force time series of the three breaking waves include the dynamic response of the tripod model (chapter 4.4). Visible oscillations and peak values are a combination of wave shape characteristics and dynamics of the tripod structure. Therefore, the peak values of the experiments are used for qualitative comparisons in this study. The three load cases show stepwise increasing loads for the broken wave with $F_{x,max} \approx 7kN$, the curled wave front with $F_{x,max} \approx 8.5kN$, and the partly vertical wave front with $F_{x,max}$ nearly 9.5 kN. Furthermore, load case 3 has the sharpest peak and the most rapid rise times, while load case 1 has a rather arched shape similar to the profile of load case 4. The characteristics of load case 2 are closer to the ones observed for LC 3 than for LC 1 with a sharp peaked crest, as well.

In Fig. 6.14 the peak forces of load case 3 and four are compared to the averaged experimental forces on the left and right, respectively. The integrated forces from the CFD simulations are unaffected by structure responses and hence, advantageous for the analysis of the forces. The CFD results shown in Fig. 6.14 demonstrate the time dependent hydrodynamic loads including the impact characteristics described in the former sections. The differences between the breaking wave cases and load case 4 directly lead to the contribution of the slamming to the total loads.

Table 6.1 lists the maximum horizontal forces taken from the CFD simulations for each load case, which range from 5 kN for LC 4 up to 8.3 kN for LC 3. The middle column shows the ratio of the maximum forces referenced to the maximum load of the quasi-static load, which gives the contribution of the isolated impact. Next to the middle column the same ratio is calculated with the maximum quasi-static load observed from the GWK experiments. The numerical value of 5 kN slightly over predicts the non-breaking wave load due to a steeper wave front in the vicinity of the wave crest than observed in the experiments. According to this procedure, the impact of the broken wave contributes 20 - 50% to the maximum load and the curled wave front 58 - 98%. As anticipated, load case 3 shows the highest impact

contribution with 66 - 108%, even though the load is only marginally higher than for the curling wave.

Fig. 6.15 gives an example for the time varying positions of the contact point of the total horizontal force F_x in combination with the water elevation η. According to equation 6.2 the lever arm z is calculated by the division of the horizontal force, which is the reason for the (truncated) poles at the zero crossings of F_x. The force points of action are plotted for z = 0 at the still water level for direct comparison to the water elevation. The positions of the acting forces along the cylinder are listed in the last column of table 6.1 with reference to the maximum water elevation (η_{max}). Load case three shows the highest force point of action on a level 14% of η_{max} above the still water level. Load case two is similar high at 0.1 η_{max} and the horizontal force of LC 1 points at a lower level (-0.48 η_{max}) below SWL to the tripod as the quasi-static case (-0.38 η_{max}), which is reasoned by the downward pointing wave tongue of LC 1.

6.3   Hydrodynamics of wave impact

Fluid velocities are of major interest for force calculations, since impact loads are proportional to the squared fluid particle velocity hitting a structure's surface. Furthermore, breaking waves have the highest water velocities at the surface of all waves and the stagnation pressure based on a constant flow velocity is commonly used in literature to normalize pressure data. With regard to the slamming problem the phase velocity of the breaking wave is a very useful reference velocity, since higher velocities indicate the region of wave breaking and probable locations of impact loads.

6.3.1   Breaking wave kinematics

The phase velocity of the focusing wave packet in the large wave flume is estimated from wave gauge recordings and video analysis in the vicinity of the tripod. Not the velocity of the whole wave but the water velocity of the wave crest just before wave breaking is of special interest in regard to the slamming problem, since this water mass contributes the impulsive forces. The video observations as well as the analyzed wave gauge records up to 10.75m in front of the main column lead to a representative crest velocity during the impact of 4.8m/s. This value agrees with observations of the crest velocities in the CFD model. Since the wave gauge records
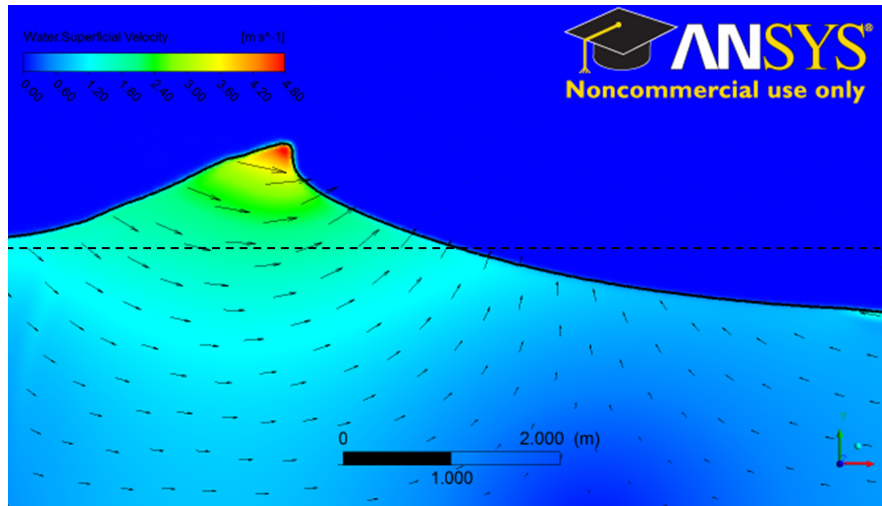
Figure 6.16: Water velocities under the breaking wave just before wave breaking.

and the wave shape of both models correlate well to each other the time resolved wave kinematics of the breaker are available in the CFD model.

Fig. 6.16 shows the wave kinematics of the breaking wave at the onset of breaking shortly before the wave crest starts to curl over for a cross-section next to the tripod and not influenced by the structure. The dashed line illustrates the still water level while the arrows represent vectors of the flow field combined with the colored magnitudes. As anticipated from wave theory, horizontal water velocities are observed under the wave crest. The velocity distribution from the wave crest down to the bottom changes rapidly above the still water level and remains relatively constant further down below. Maximum water velocities from 4.2 to 4.8m/s cover the upper 25% of the positive maximum water elevation, continued by roughly 2.4m/s covering almost 50% of the crest height. The horizontal velocities under the wave crest and below the still water level range from 1 to 2m/s with small velocity gradients. The velocity distribution shows that only less than 25% of the upper wave crest contains sufficiently high velocities to overcome the phase speed of the wave and to curl over. Hence, the developing breaker tongue is relatively thin and the observed breaker type is an intermediate case of spilling and plunging breaking. This type of wave breaking was tested within the framework of the research project "Gigawind alpha ventus" for offshore wind farm locations near the research platform FINO I. The water depth around FINO I is about 30m and extreme wave breaking is assumed to be rather spilling type or moderate plunging breaking for that location, which is adopted for this study.

Fig. 6.17 shows the distribution of the horizontal water velocities for the unaffected wave profile in direct comparison to the deformed wave influenced by the tripod
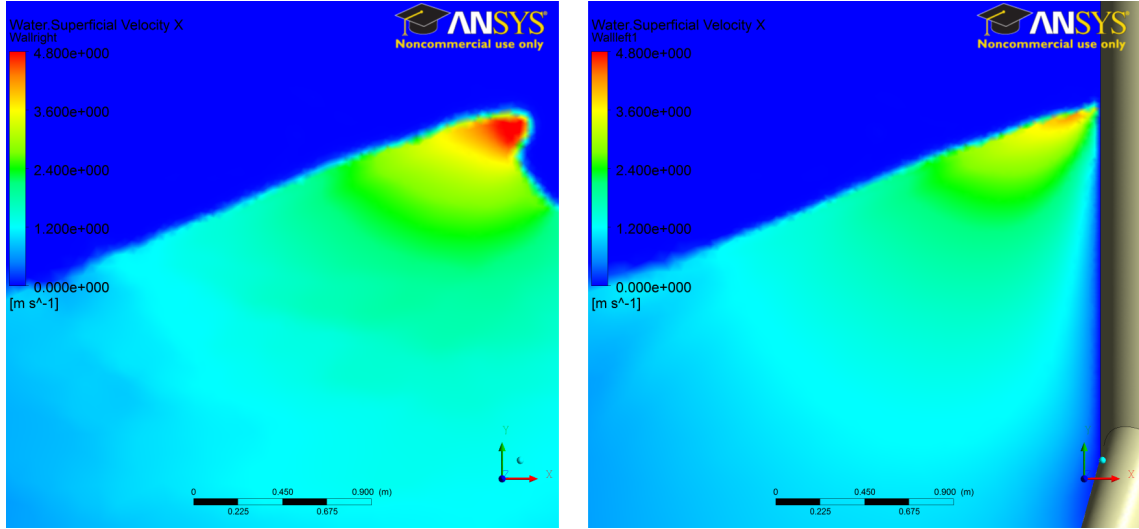
Figure 6.17: Horizontal water velocities for the unaffected wave profile (left) and for the same point in time in the vertical plane of the stagnation pressure ahead of the tripod (right).

structure. The difference between the two cross-sections illustrates the regions of redirected water masses and consequently indicates regions of accelerated water. Since the unaffected wave shows higher velocities at the structure and especially in the vicinity of the wave crest, the impacting fluid is decelerated. The subtraction of two succeeding velocity cross-sections and the subsequent division of the corresponding time interval, stepwise reveals the regions of accelerated water masses due to the influence of the tripod.

6.4   Concluding remarks

The connection of the impact pressures and the corresponding coefficients with slamming characteristics is exemplarily visible by the correlating width of the curling factor in Fig. 6.9 ($C_S > 1 \ \rho R c^2$) and the range of intensive pressure in Fig. 6.1, plot (g). Furthermore, the observed point in time $0.25 < \mathrm{t}/T_i < 0.30$ as well as the relative height $z/\eta_{max} = 0.9$ of the maximum slamming coefficient, matches to the pressure distribution for $\mathrm{t}/T_i = 0.25$ in Fig. 6.1. The comparison of the time dependent pressure distribution and the synchronously developing slamming coefficients emphasizes the differences between line forces and impact pressures. Since the line force takes the whole pressure field of the circumference into account, the maximum force must not necessarily occur simultaneous to the maximum impact pressure, but at the instant of time when the integrated pressures up to 30 - 40
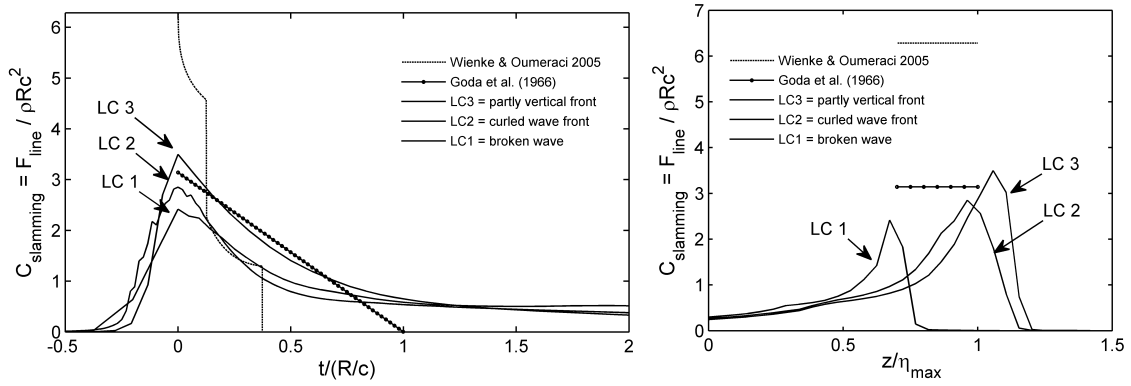
Figure 6.18: Variation of maximum slamming coefficients from LC 1 - 3 versus time (left) and versus relative height z/η_{max} (right) in comparison to Wienke and Oumeraci (2005) and Goda et al. (1966).

degrees are maximum.

Zhou et al. (1991) report impact area extensions of ≈ 20 degrees to each side, which is also found in the GWK experiments. In addition, the reported range of slamming pressures between 4-13 ρc^2 is almost identical to the maximum pressures between 4-12.5 ρc^2, as shown in Fig. 6.7 for LC 1-3. However, the range given by Chan et al. (1991) and Chan et al. (1995) of 16 to 47 ρc^2 is not observed and the proposed definition for slamming characteristics by p > 3 ρc^2 is only observed for the single cases. In this study, slamming characteristics are observed for p > 1 ρc^2 of averaged signals, however, the number of test cases is far to small to derive general statements. Both, the slamming positions observed in the GWK experiments as well as in the CFD model are in good agreement with the obtained locations by Chan et al. (1991) and Chan et al. (1995).

The observed impact loads of load case 2 ($C_S = 3.0$) and three ($C_S = 3.5$) rather match the theoretical slamming coefficient $C_S = \pi$ given by von Karman (1929) and adopted by Goda et al. (1966) than the theoretical predictions according to Wienke and Oumeraci (2005), as can be seen in Fig. 6.18 (left). Last mentioned formulation includes a maximum value of $C_S = 2\pi$ for the partly vertical wave front and is implemented to guidelines for recommended practice. The difference of $2\pi - 3.5 = 2.6$ to the observed values in this study offers potential for optimization with regard to efficient OWEC designs. Furthermore, the slamming coefficient $C_S = 2\pi$ is constantly distributed along the section of the upright wave front (referred as curling factor). As plotted in Fig. 6.18 (right), the vertical distribution of LC 1-3 considerably decreases like a triangular shape above and below the peak coefficients along the cylinder's span, additionally seen in figures 6.8 to 6.10.

It should be noted that this study does not include full plunging breaking with large
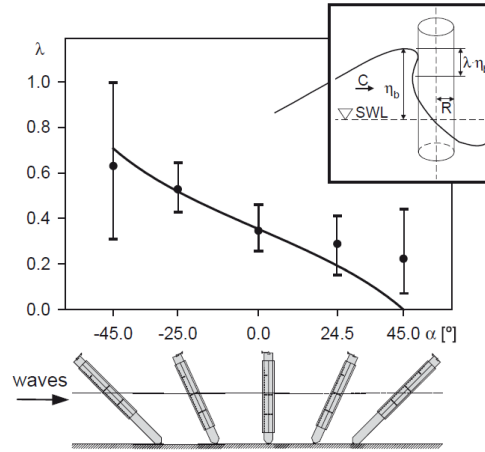
Figure 6.19: Curling factors for various cylinder positions according to Wienke and Oumeraci (2005).

vertical wave fronts like the studies of Wienke and Oumeraci (2005) do, and the direct comparison to load case 3 is not valid to the full extend. Furthermore, additional simulations with very fine grids in the impact area show increasing trends for the maximum C_S value. However, the deceasing load distribution along the span remains and the observed results from the physical and numerical model show noticeable differences and significantly reduced loads in comparison to load estimations according to guidelines.

The curling factor of 0.3-0.4 for the vertical cylinder position given by Wienke and Oumeraci (2005) matches the curling factor observed for regions of $C_S > 1 \ \rho R c^2$ of load case 3 (see Chapter 7.1). Fig. 6.19 shows decreasing curling factors for inclined cylinder positions in the backwards direction, which represents load cases of curled wave crests with regard to the γ angle (angle between the perpendicular line of the vertical wave front and the vertical center line of the cylinder) in the equations 2.22 and 2.23. This correlates to the observed values and trends summarized in the next chapter.

Hanssen and Tørum (1999) state that the approach by Morison et al. (1950) applies for load calculations shortly after the cylinder is submerged. This is also observed for load cases two and three in this study and seen in the figures 6.9 and 6.10 by the rapidly decreasing C_S values to 0.7 - 0.5, which is in the range of commonly used C_D coefficients for the Morison approach.

The force coefficients change in a relatively similar way outside the impact area and decrease down to $C_S \geq 0.5$ at relative heights above the water level on the rear side of the cylinder, indicated by the lower solid white lines. Shortly below this water level at $z/\eta_{max} \approx 0.2$ up to 0.4 the coefficients drop to values around $C_S = 0.25$ - 0.3 in all

three load cases as exemplarily illustrated in Fig. 6.11 (left) and seen in appendix B for LC 1 and 3. The velocities at these relative heights range between 2.0 - 2.4m/s according to Fig. 6.16 and remain relatively long in contrast to the high variation near the wave crest. The C_S coefficients in this region match the C_D values given by Schlichting (1982) for a cylinder in steady flow, which leads to the assumption that the flow conditions for short periods of time might be regarded as "quasi-static" or stationary. With regard to Fig. 6.11 (left), this would be the case at relative heights with minor changes in color and magnitude along the abscissa. The distance along the abscissa gives the period of time for the stationary flow condition, e.g. 2 times T_i between $z/\eta_{max} = 0$ - 0.2. Vice versa, regions with varying coefficients over time indicate unsteady flow conditions and give outer boundaries of impact loads.

Total forces from the CFD model are in good correlation to the numerical model, since the total force measurements in the experiments fluctuate significantly less in comparison to the pressure recordings above $z/\eta_{max} > 0.62$. The reason is found in the partial contribution of the impact pressure to the total force, which reaches values up to 2.08 for the ratio impact load to quasi-static load.

7 Summary & Outlook

7.1 Summary

Cumulating reports on rogue wave impacts in potential areas for OWEC (Chapter 1.1) provide the motivation for this work in combination with the growing demand for offshore wind energy solutions by means of efficient designs for mass production. An efficient design requires a detailed load assessment, which is why large scale tests (1:12) and numerical simulations were performed to reveal further insights on kinematics, pressures and forces due to different type of wave breaking. The experimental setup is documented in chapter 3, and chapter 5 describes the validation and numerical setup for the 3D flow simulations.

The following main results are obtained from data analysis with regard to the formulated objectives (chapter 1.2) based on the reviewed literature (Chapter 2):

1. **Development of impact regions.** (Chapter 6.1)

   The tabulated results show the impact characteristics for the broken wave (LC 1), the curled wave front (LC 2), as well as for the partly vertical wave front (LC 3), which are characterized in Chapter 4.3. The vertical range describes the occurrence of averaged pressures $>1\rho c^2$ during the impact, while the curling factor denotes simultaneously acting pressures along the span. Mean pressure peaks are averaged from the number of tests shown in table 3.1 and the single peaks are the highest observed pressures at the given relative heights.

	LC 1	LC 2	LC 3
Vertical range	$0.6 - 1.1 \, \eta_{max}$	$0.7 - 1.2 \, \eta_{max}$	$0.7 - 1.3 \, \eta_{max}$
Curling factor	$0.2 \, \eta_{max}$	$0.2 - 0.3 \, \eta_{max}$	$0.3 \, \eta_{max}$
Local impact duration	$0.5 - 1.0 \, T_i$	$0.4 - 0.5 \, T_i$	$0.4 \, T_i$
Global impact duration	$2.5 \, T_i$	$1.5 \, T_i$	$1.5 \, T_i$
Mean pressure peak	$2 \, \rho c^2$	$3 \, \rho c^2$	$5 \, \rho c^2$
Single pressure peak	$4 \, \rho c^2$	$5 \, \rho c^2$	$12.5 \, \rho c^2$
Peak location	$0.8 \, \eta_{max}$	$0.9 - 1.0 \, \eta_{max}$	$1.0 \, \eta_{max}$

2. **Breaking wave kinematics.** (Chapter 6.3.1)

   The horizontal water velocities at the onset of wave breaking amount 4.2 to 4.8m/s (0.88-1c) at the upper 25% of the positive maximum water elevation, continued by roughly 2.4m/s (0.5c) along almost 50% of η_{max}. The horizontal velocities below the still water level range from 1 to 2m/s (0.2-0.42c) with small velocity gradients.

3. **Structure response and air dynamics.** (Chapter 4.4)

   Short time Fourier transformation spectra from acceleration meters fixed on the main column at z/eta_{max}=1.1 as well as from pressure sensors at the same relative height are compared. In addition to the natural frequencies of approximately 10 Hz, 85 Hz, and 100 Hz, additional frequencies around 20Hz, 40Hz, and 60Hz are found in the pressure signals. Last mentioned components might be generated by air bubble dynamics.

4. **Local impact forces.** (Chapter 6.2.1)

   Increasing local peak-forces and -locations are observed for decreasing distances of wave breaking in front of the tripod (LC 1-3). The rising time of the maximum force as well as the local impact time at a specific height reduce with decreasing wave breaking distances. The global impact time is taken between the first and last coefficient exceeding $1\rho Rc^2$ along the span, while the local impact time is taken at a fixed location and given in the following table.

	LC 1	LC 2	LC 3
Max local force	$C_S \approx 2.7$ & $2.0\ \rho Rc^2$	$C_S \approx 3.0\ \rho Rc^2$	$C_S \approx 3.5\ \rho Rc^2$
Peak location	0.65 & 0.9 η_{max}	0.95 η_{max}	$0.9 - 1.0\ \eta_{max}$
Rise time	0.25 T_i	0.2 T_i	0.1 T_i
Local impact time	$0.5 - 1.0\ T_i$	$0.4 - 0.5\ T_i$	0.4 T_i
Global impact time	2.5 T_i	1.5 T_i	1.5 T_i

   By means of the validated three-dimensional CFD model the local forces are estimated from integrated pressures at each vertical level of the tripod and presented in the figures 6.8 to 6.10, which give the normalized, time-depending, spatial force distribution for different types of wave breaking.

5. **Total forces and points of action.** (Chapter 6.2.2)

   CFD based horizontal forces as well as the positions of the points of action along the main column are listed below. The vertical heights of the acting points are normalized by η_{max}, i.e. 14% of the crest height above the still water level for LC 3. Since the CFD model is not affected by structure responses,

the relative contribution ($F_{x,max,CFD}$/LC4) of the impact components for the three different cases is given by the force ratio of LC 1-3 and the quasi-static case (LC 4) from the CFD model.

	LC 1	LC 2	LC 3	LC 4
$F_{x,max,CFD}$ [kN]	6.0	7.9	8.3	5 (CFD) & 4 (GWK)
$F_{x,max,CFD}$ / LC 4	1.20-1.50	1.58-1.98	1.66-2.08	1.00
Acting point at z/η_{max}	-0.48	+0.10	+0.14	-0.38

7.2 Outlook

The analyzed experiments and numerical simulations are based on a constant wave height, wave period, as well as on a constant diameter of the main column. Zhou et al. (1991) report that the pressure characteristics are very similar for varying diameters. Nevertheless, the shape of the wave front depends on the wave steepness in terms of wave height and wave period, and the pressure characteristics are sensitive to the wave front, as observed in this study and by Zhou et al. (1991), Chan et al. (1995). The calculative relationship of increasing wave heights and total forces is especially interesting with regard to the statistical estimation of H_{sig} and the connected sensitivity of the design wave parameters, as described in chapter 2.1.

Furthermore, a higher number of repeated wave tests is necessary for the estimation of more accurate mean peak pressures and standard deviations, as performed by Chan et al. (1991).

In addition, other configurations with a rotated tripod substructure could be investigated to verify the effect of different vortex shedding with regard to wave focusing and impact.

The three-dimensional CFD model can be used to obtain more details on the hydrodynamics directly at the impacted structure. Since a local change of water momentum results in a local force, hydrodynamic details about the accelerated velocities could give reason to the time resolved impulsive pressures in the slamming area.

Additional effects on the hydrodynamics and forces due to marine growth in the splash zone could be analyzed by various wall roughnesses as well as by further laboratory experiments.

Finally, further investigations about the significant influence of air dynamics and structure oscillations on the pressure and force characteristics require additional experiments as well as coupled simulations for fluid-structure-interactions (FSI).

References

Arntsen, O., Ros, X., Tørum, A., 2011. Impact forces on a vertical pile from plunging breaking waves. In Coastal Structures 2011, Yokohama, Japan.

Babanin, A., 2011. Breaking and Dissipation of Ocean Surface Waves. Cambridge University Press.

Babanin, A., Young, I., Banner, M., 2001. Breaking probabilities for dominant surface waves on water of finite constant depth. Journal of Geophysical Research C: Oceans 106 (C6), 11659–11676.

Banner, M., Babanin, A., Young, I., 2000. Breaking probability for dominant waves on the sea surface. Journal of Physical Oceanography 30 (12), 3145–3160.

Barltrop, N., Adams, A., 1991. Dynamics of Fixed Marine Structures. Butterworth-Heinemann Ltd.

Battjes, J., 1974. Surf similarity. Proc. 14th ASCE Coastal Engng. Conf. (Copenhagen, Denmark) 1, June 24–28, 1974.

Battjes, J., Janssen, J., 1979. Energy loss and set-up due to breaking of random waves. Proceedings of the Coastal Engineering Conference 1, 569–587.

BMU, 2010. Energiekonzept 2050 - Meilensteine und Bewertungen. Bundesministeriums für Umwelt, Naturschutz und Reaktorsicherheit, www.bmu.de/energiewende/beschluesse_und_massnahmen/doc/46497.php.

Bredmose, H., Jacobsen, N., 2010. Breaking wave impacts on offshore wind turbine foundations: Focused wave groups and cfd. Proceedings of the International Conference on Offshore Mechanics and Arctic Engineering - OMAE, Shanghai-China 3, 397–404.

Campbell, I., Weynberg, P., 1980. Measurement of parameters affecting slamming. Technology Report 440, Southampton University: Wolfson Unit for Marine Technology.

Cazenave, S., Chauche, E., McKenna, T., Dufau, G., MacKenna, T., Hurel, A., Nouqueret, P., 2006. Wellen. Faszinierende Schauspiele der Ozeane. Delius Klasing Verlag, Auflage: 2 (15. Juni 2006).

Chakrabarti, S., 1987. Hydrodynamics of Offshore Structures. Wessex Institute of Technology, WIT Press.

Chan, E., Tan, B., Cheong, H., 1991. Variability of plunging wave pressures on vertical cylinders. International Journal of Offshore and Polar Engineering 1 (2), 94–100.

Chan, E.-S., Cheong, H.-F., Tan, B.-C., 1995. Laboratory study of plunging wave impacts on vertical cylinders. Coastal Engineering 25 (1-2), 87–107.

Chaplin, J., Flintham, T., Greated, C., Skyner, D., 1992. Breaking wave forces on a vertical cylinder. Report 90 324, Health and Safety Executive, London, United Kingdom.

Clauss, G., Klein, M., Onorato, M., 2011. Formation of extraordinarily high Waves in Space and Time. Vol. 2. Proceedings of the International Conference on Offshore Mechanics and Arctic Engineering - OMAE, pp. 417–429.

Clauss, G. F., 2010. Advances in Numerical Simulation of Nonlinear Water Waves - Freak Waves and their Interaction with Ships and Offshore Structures. World Scientific, Ch. 18, pp. 641–687.

Corte, C., Grilli, S., 2006. Numerical modeling of extreme wave slamming on cylindrical offshore support structures. Proceedings of the International Offshore and Polar Engineering Conference, San Francisco - USA, 394–401.

Dean, R., 1965. Stream function representation of nonlinear ocean waves. Journal of Geophysical Research 70, 4561–4572.

Dean, R., 1974. Evaluation and development of water wave theories for engineering application. Special Report No. 1, U. S. Army Corps of Engineers, Coastal Engineering Research Center, Fort Belvoir, VA.

Dean, R., Dalrymple, R., 1991. Water Wave Mechanics for Engineers and Scientists. World Scientific Pub Co Inc.

Dong, W., Moan, T., Gao, Z., 2011. Long-term fatigue analysis of multi-planar tubular joints for jacket-type offshore wind turbine in time domain. Engineering Structures 33 (6), 2002–2014.

Faltinsen, O., 1990. Sea Loads on Ships and Offshore Structures. Cambridge Ocean Technology Series. Cambridge University Press.

Faulkner, D., 2000. Rogue waves - defining their charateristics for marine design. Rogue Waves 2000, Brest - France, 3–18.

Fenton, J., 1985. A fifth-order stokes theory for steady waves. Journal of Waterway, Port, Coastal and Ocean Engineering 111, 216–234.

Gemmrich, J., 2005. On the occurence of rogue waves. Rogue Waves - Proceedings of the 14th 'Aha Huliko'a Hawaiian Winter Workshop, Meeting Report, Oceanography, 18(3):66-75.

Gemmrich, J., Farmer, D., 1999. Observations of the scale and occurrence of breaking surface waves. Journal of Physical Oceanography 29 (10), 2595–2606.

Gemmrich, J., Garrett, C., 2011. Dynamical and statistical explanations of observed occurrence rates of rogue waves. Natural Hazards and Earth System Science 11 (5), 1437–1446.

Goda, Y., 1970. A synthesis of breaker indices. Trans. Japan Society of Civil Engineers.

Goda, Y., 2010. Random seas and design of maritime structures. Advanced Series on Ocean Engineering, Vol. 33, 3rd Edition, World Scientific, Singapore.

Goda, Y., Haranaka, S., Kitahata, M., 1966. Study on impulsive breaking wave forces on piles. Report Port and Harbour Technical Research Institute 6, 1–30.

Hanssen, A., Tørum, A., 1999. Breaking wave forces on tripod concrete structure on shoal. Journal of Waterway, Port, Coastal, and Ocean Engineering 125, 304–310.

Harlow, F., Welch, J., 1965. Numerical calculation of time-dependent viscous incompressible flow of fluid with free surface. Physics of Fluids 8 (12), 2182–2189.

Hildebrandt, A., Schlurmann, T., 2012a. Breaking wave impact on offshore tripod structures - Comparison of large scale experiments, CFD simulations, and DIN recommended practice [Wellenbrechen an Offshore Tripod-Gründungen -Versuche und Simulationen im Vergleich zu Richtlinien]. Bautechnik 89 (5), 301-308.

Hildebrandt, A., Schlurmann, T., 2012b. Breaking wave kinematics, local pressures, and forces on a tripod support structure. Proceedings of the 33rd International Conference on Coastal Engineering - ICCE, Santander-Spain.

Johannessen, K., Meling, T., Haver, S., 2002. Joint distribution for wind and waves in the northern north sea. International Journal of Offshore and Polar Engineering 12 (1), 1–8.

Justesen, P., 1989. Hydrodynamic forces on large cylinders in oscillatory flow. J. Waterway, Port, Coastal and Ocean Engineering, ASCE 115 (4), 497–514.

Kjeldsen, S., 1990. Water Wave Kinematics. Kluwer Academic Publisher., Ch. Breaking Waves, pp. 453–473.

Komar, P., Gaughan, M., 1972. Airy wave theory and breaker height prediction. Proc. 13th Coastal Engineering Conference, ASCE, 405–418.

Le Mehaute, B., 1969. An Introduction to Hydrodynamics and Water Waves. Springer-Verlag, New York Inc., 1976.

Lesny, K., 2009. Gründung von Offhshore-Windenergieanlagen. Mitteilungen aus dem Fachgebiet Grundbau und Bodenmechanik, Universität Duisburg-Essen, VGE-Verlag.

Liu, P., Babanin, A., 2004. Using wavelet spectrum analysis to resolve breaking events in the wind wave time series. Ann. Geophysicae 22, 3335–3345.

Marino, E., Borri, C., Peil, U., 2011. A fully nonlinear wave model to account for breaking wave impact loads on offshore wind turbines. Journal of Wind Engineering and Industrial Aerodynamics 99 (4), 483–490.

ABS, 2011. Design Standards for Offshore Windfarms. American Bureau of Shipping (ABS).

API, 1993. Recommended Practice for Planning, Designing and Constructing Fixed Offshore Platforms - Load and Resistance Factor Design, July 1st. American Petroleum Institute (API).

CEM, 2008. Coastal Engineering Manual, August 2008. US Army Corps of Engineers.

DIN, 2009. DIN EN 61400-3:2009 Auslegungsanforderungen für Windenergieanlagen auf offener See. Deutsches Institut für Normung e. V. (DIN).

DNV, 2007. Recommended Practice DNV-RP-C205, Environmental Conditions and Environmental Loads, April 2007. Det Norske Veritas (DNV).

GL, 2005. Rules and Guidelines Industrial Services - Guideline for the Certification of Offshore Wind Turbines. Germanischer Lloyed (GL).

IEC, 2009. IEC 61400-3: Wind Turbines Part 3: Design Requirements for Offshore Wind Turbines, 1st Edition. International Electrotechnical Commission (IEC).

McCowan, J., 1894. On the highest waves of a permanent type. Philosophical Magazine, Edinburgh 38 (5), 351–358.

Menter, F., 1994. Two-equation eddy-viscosity turbulence models for engineering applications. American Institue of Aeronautics and Astronautics (AIAA) Journal 32 (8), 1598–1605.

Miche, M., 1944. Movements ondulatoires des mers en profondeur constante ou decroissante. Annales de Ponts et Chaussees.

Mokrani, C., Abadie, S., Grilli, S., Zibouche, K., 2010. Numerical simulation of the impact of a plunging breaker on a vertical structure and subsequent overtopping event using a navier-stokes vof model. Proceedings of the International Offshore and Polar Engineering Conference 3, 729–736.

Morison, J., O'Brien, M., Johnson, J., Schaaf, S., 1950. The force exerted by surface waves on piles. Petroleum Transactions, AIME 189.

Nickerson, 1993. Freak waves! Mariners Weather Log NOAA - National Oceanic and Atmospheric Administration 37(4), 14–19.

Nikolkina, I., Didenkulova, I., 2012. Catalogue of rogue waves reported in media in 2006-2010. Natural Hazards 61 (3), 989–1006.

Nitsch, J., 2008. Leitstudie 2008 - Weiterentwicklung der Ausbaustrategie Erneuerbare Energien vor dem Hintergrund der aktuellen Klimaschutzziele Deutschlands und Europas. Untersuchung im Auftrag des Bundesministeriums für Umwelt, Naturschutz und Reaktorsicherheit.

Ochi, M., 2003. Hurricane-Generated Seas. Elsevier Ocean Engineering Book Series (Volume 8), Elsevier Ltd. Oxford, UK.

Oger, G., Guilcher, P., Jacquin, E., Brosset, L., Grenier, N., Touze, D., 2010. Simulations of liquid impacts using a two-fluid parallel sph model. 5th international SPHERIC workshop, pages 7682, Manchester, United Kingdom.

Oumeraci, H., Klammer, P., Partenscky, H., 1993. Classification of breaking wave loads on vertical structures. Journal of Waterway, Port, Coastal, & Ocean Engineering - ASCE 119 (4), 381–397.

Outzen, O., Herklotz, K., Heinrich, H., Lefebvre, C., 2008. Extreme waves at fino 1 research platform caused by storm tilo on 9 november 2007. DEWI Magazin 33, 17–23.

Pakozdi,   C.,   Kendon,   T.,   Stansberg,   C.,   2011. Breaking wave impact on a platform column: An introductory CFD study. Proceedings of the International Conference on Offshore Mechanics and Arctic Engineering - OMAE, Rotterdam-Netherlands 1, 645–654.

Pfeil, G., 2004. Auf der Jagd nach Meeresmonstern. Der Spiegel, Ausgabe 2/2004, pp. 106-108.

Rapp, R., Melville, W., 1990. Laboratory measurements of deep-water breaking waves. Phil. Trans. R. Soc. Lond. A311, 735–800.

Rattanapitikon, W., Shibayama, T., 2000. Verification and modification of breaker height formulas. Coastal Engineering Journal 42 (4), 389–406.

REN21, 2011. Renewables 2011 Global Status Report. REN21 Secretariat, Paris.

Sarpkaya, T., 1978. Wave impact loads on cylinders. Proc. Offshore Technology Conference, Houston, Texas.

Sarpkaya, T., 1986. Force on a circular cylinder in viscous oscillatory flow at low keulegan-carpenter numbers. Journal of Fluid Mechanics 165, 61–71.

Sawaragi, T., Nochino, M., 1984. Impact forces of nearly breaking waves on a vertical circular cylinder. Coastal Engineering Journal 27, 249–263.

Schlichting, H., 1982. Boundary-layer theory. Verlag G. Braun, Karlsruhe, 8. Auflage.

Schlurmann, T., 1999. Nichtlineare Interaktionsprozesse multichromatischer Wellengruppen und das Ausbreitungsverhalten von Freak Waves - Dissertationsschrift. Bergische Universität Wuppertal, Fachbereich Bauingenieurwesen.

Schlurmann, T., 2004. Time-Frequency Analysis Methods in Hydrology and Hydraulic Engineering - Habilitationsschrift. Bergische Universität Wuppertal, Fachbereich Bauingenieurwesen.

Schmittner, C., 2005. Rogue Wave Impact on Marine Structures. Technische Universität Berlin, Fakultät V Verkehrs- und Maschinensysteme - Dissertation.

Sparboom, U., Oumeraci, H., Schmidt-Koppenhagen, R., Grüne, J., 2005. Lage-scale model study on cylinder groups subject to breaking and nonbreaking waves. Proc. 5th Int. Symposium on Ocean Wave Measurement and Analysis (WAVES), ASCE, Madrid.

Sriram, V., Sannasiraj, S., Sundar, V., 2006. Numerical simulation of 2d nonlinear waves using finite element with cubic spline approximation. Journal of Fluids and Structures 22 (5), 663–681.

Stahlmann, A., Schlurmann, T., 2012. Investigations on scour at tripod foundations [Kolkbildung an komplexen Gründungsstrukturen für Offshore-Windenergieanlagen: Untersuchungen zu Tripod-Gründungen in der Nordsee]. Bautechnik 89 (5), 293-300.

Stansberg, C. T., 2011. Characteristics of steep second-order waves in finite and shallow water. Proceedings of the ASME 30th International Conference on Ocean, Offshore and Arctic Engineering OMAE2011.

Suyuthi, A., Haver, S., 2009. Extreme loads due to wave breaking against plat-form column. Proceedings of the International Offshore and Polar Engineering Conference, Osaka-Japan, 472–479.

Thornton, E., Guza, R., 1983. Transformation of wave height distribution. Journal of Geophysical Research 88, 5925–5938.

von Karman, T., 1929. The impact on seaplane floats during landing. National Advisory Committee for Aeronautics. Technical Note No. 321.

Wagner, H., 1932. Über Stoß- und Gleitvorgänge an der Oberfläche von Flüssigkeiten. Zeitschrift für angewandte Mathematik und Mechanik 12, 193–215.

Wheeler, J., 1970. Method for calculating forces produced by irregular waves. The Journal of Petroleum Technology 249, 359–367.

Wienke, J., 2001. Druckschlagbelastung auf schlanke zylindrische Bauwerke durch brechende Wellen. PhD thesis, Technischen Universitat Carolo-Wilhelmina zu Braunschweig, Germany.

Wienke, J., Oumeraci, H., 2005. Breaking wave impact force on a vertical and inclined slender pile - theoretical and large-scale model investigations. Coastal Engineering 52 (5), 435–462.

Zhou, D., Chan, E., Melville, W., 1991. Wave impact pressures on vertical cylinders. Applied Ocean Research 13 (5), 220–234.

A   Appendix 1

Table A.1: Test wave numbers of LC 1-4 with acoustic shock and strong cylinder vibration.

Rotation	Load case 1	Load case 2	Load case 3	Load case 4
0°	-/3	-/5	1,2,5/7	-/2
10°	-/3	2/4	-/3	-/2
20°	-/3	-/4	1/3	-/2
30°	-/4	-/3	-/3	-/2
40°	-/3	-/3	2,3/3	-/2
50°	-/3	-/3	1,2/4	-/2
60°	-/3	-/3	2/3	-/2
70°	-/3	-/3	2/3	-/2
Sum:	0/25	1/28	10/29	0/16

B   Appendix 2
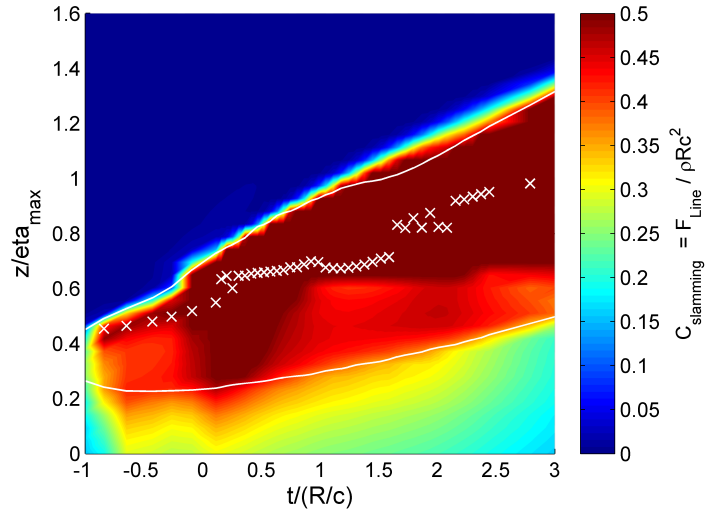
Figure B.1: Slamming coefficients of LC 1 analogous to figure 6.8 with emphasized coefficients of lower magnitude.
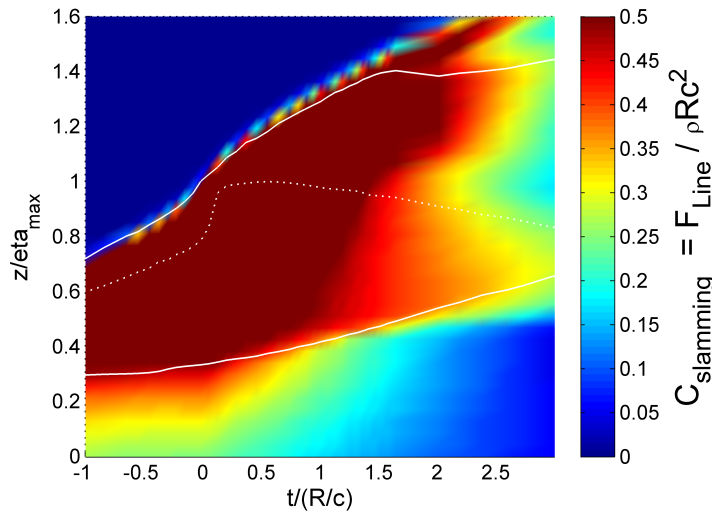
Figure B.2: Slamming coefficients of LC 3 analogous to figure 6.10 with emphasized coefficients of lower magnitude.
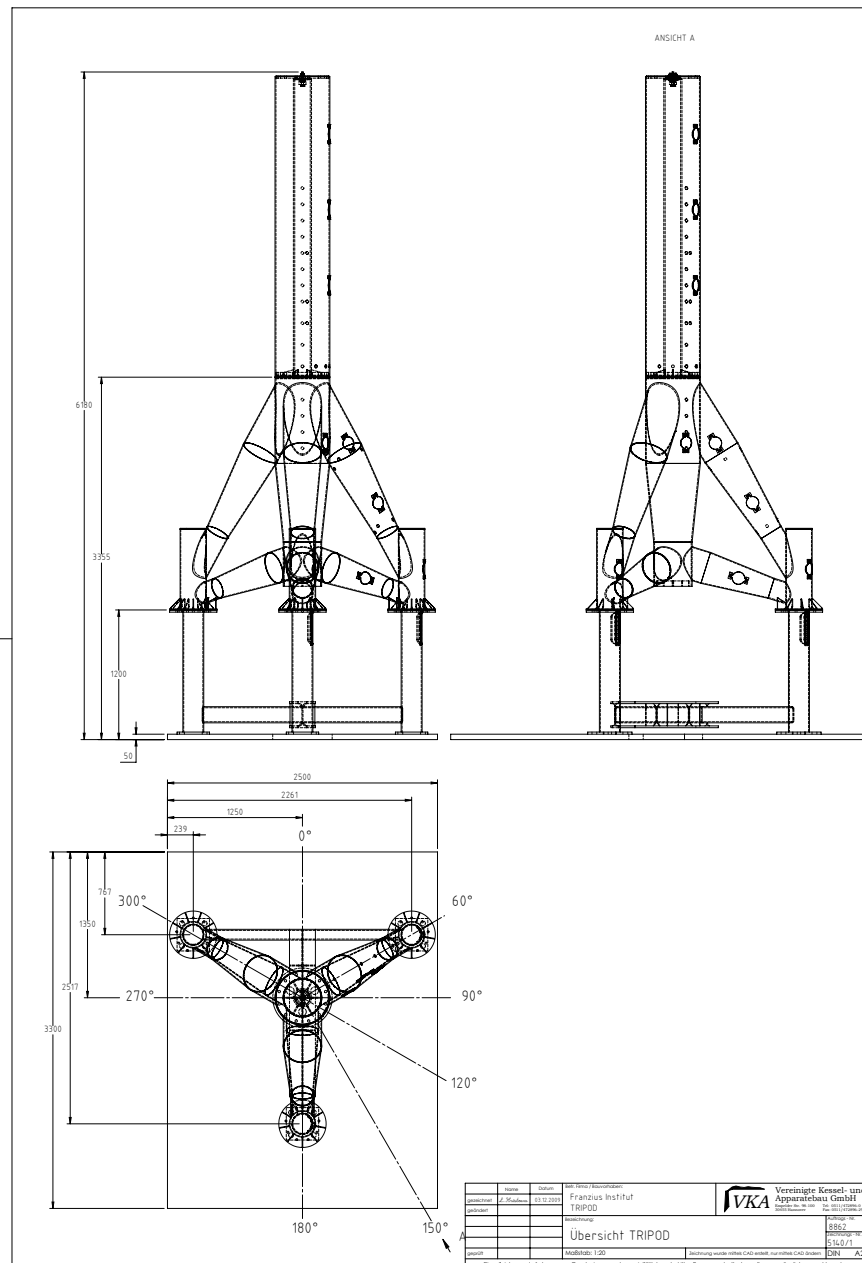
C Appendix 3

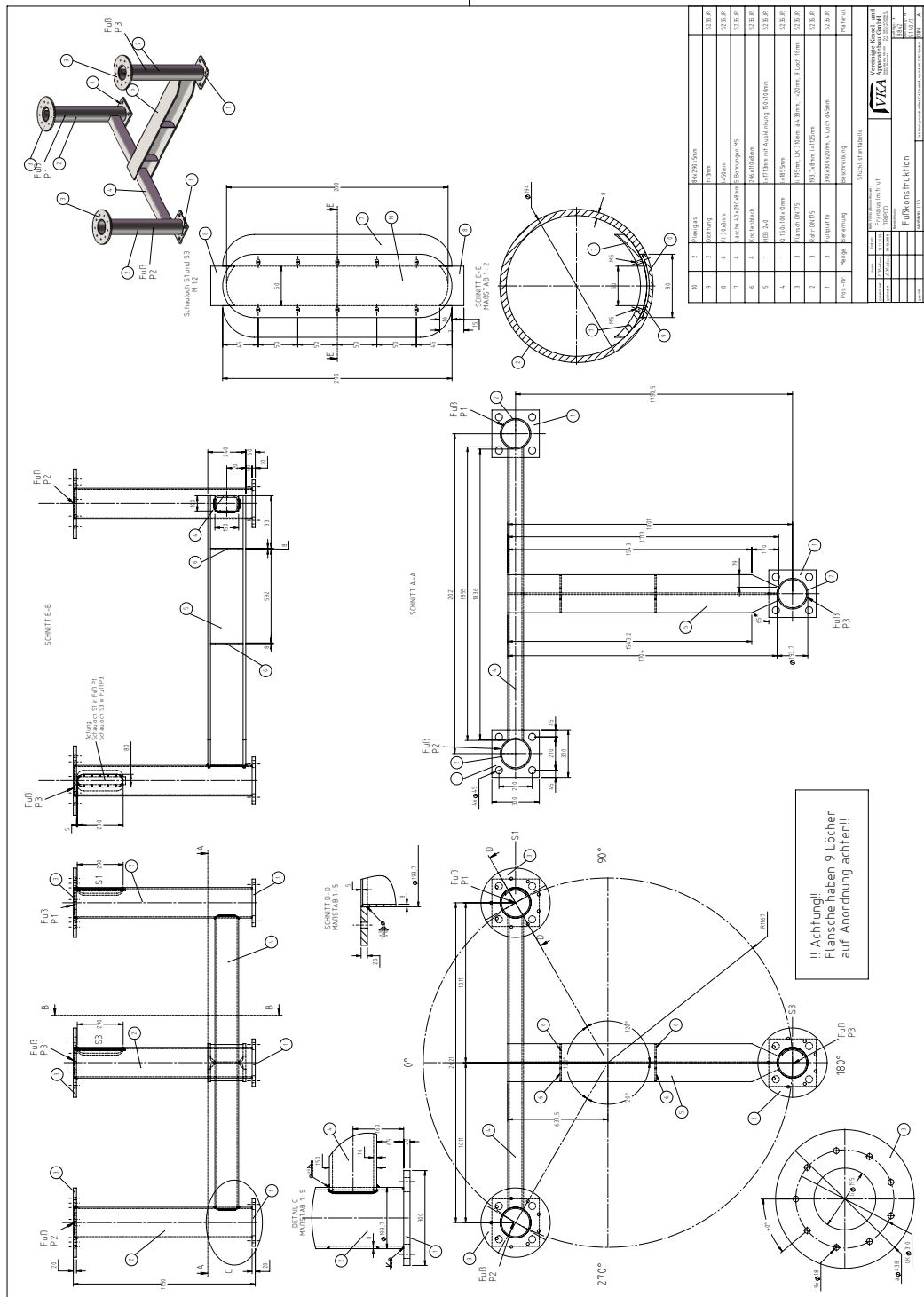Figure C.1: Constructional drawing 1 of the tripod model for the large wave flume tests.

Figure C.2: Constructional drawing 2 of the tripod model for the large wave flume tests.
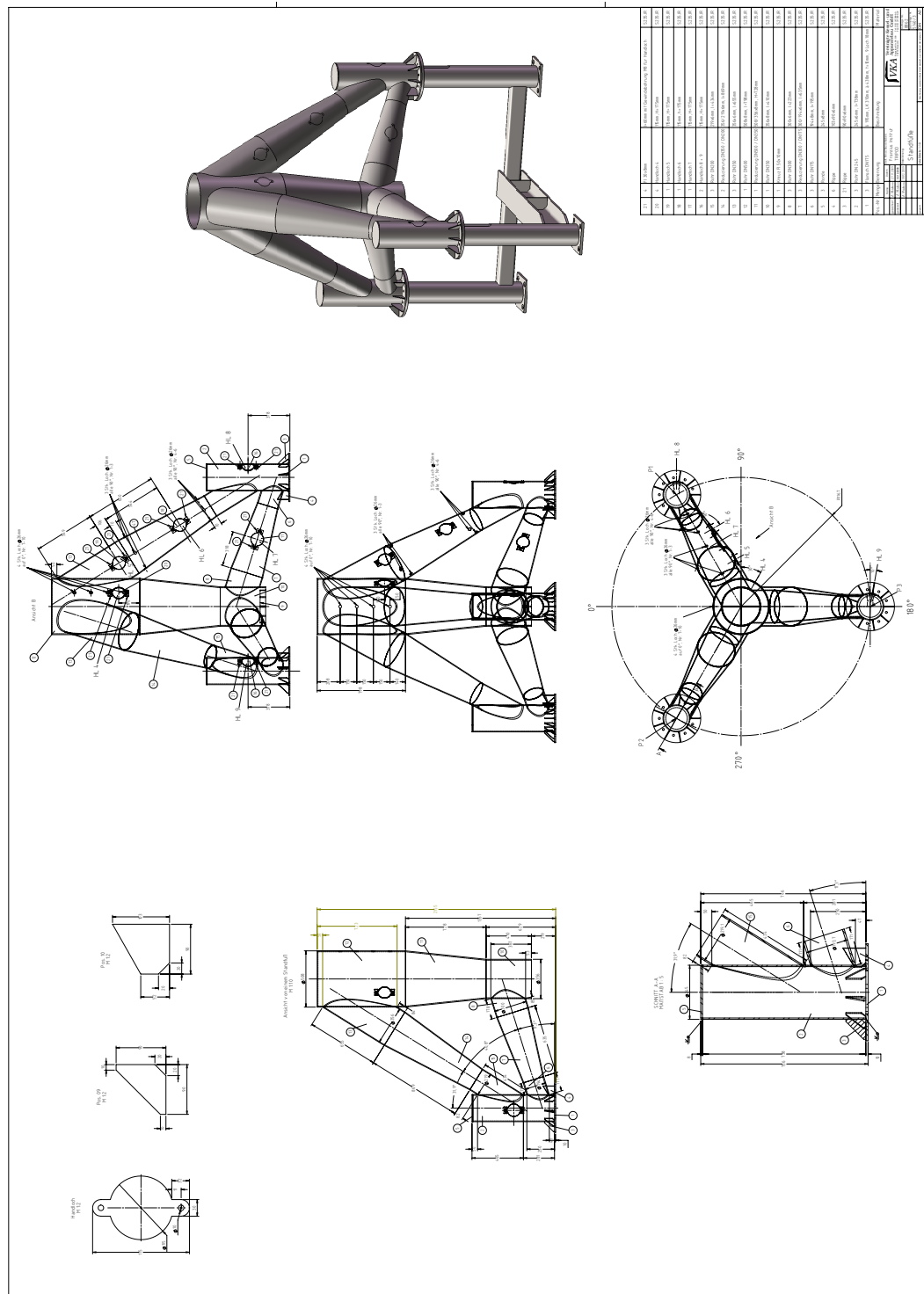
Figure C.3: Constructional drawing 3 of the tripod model for the large wave flume tests.
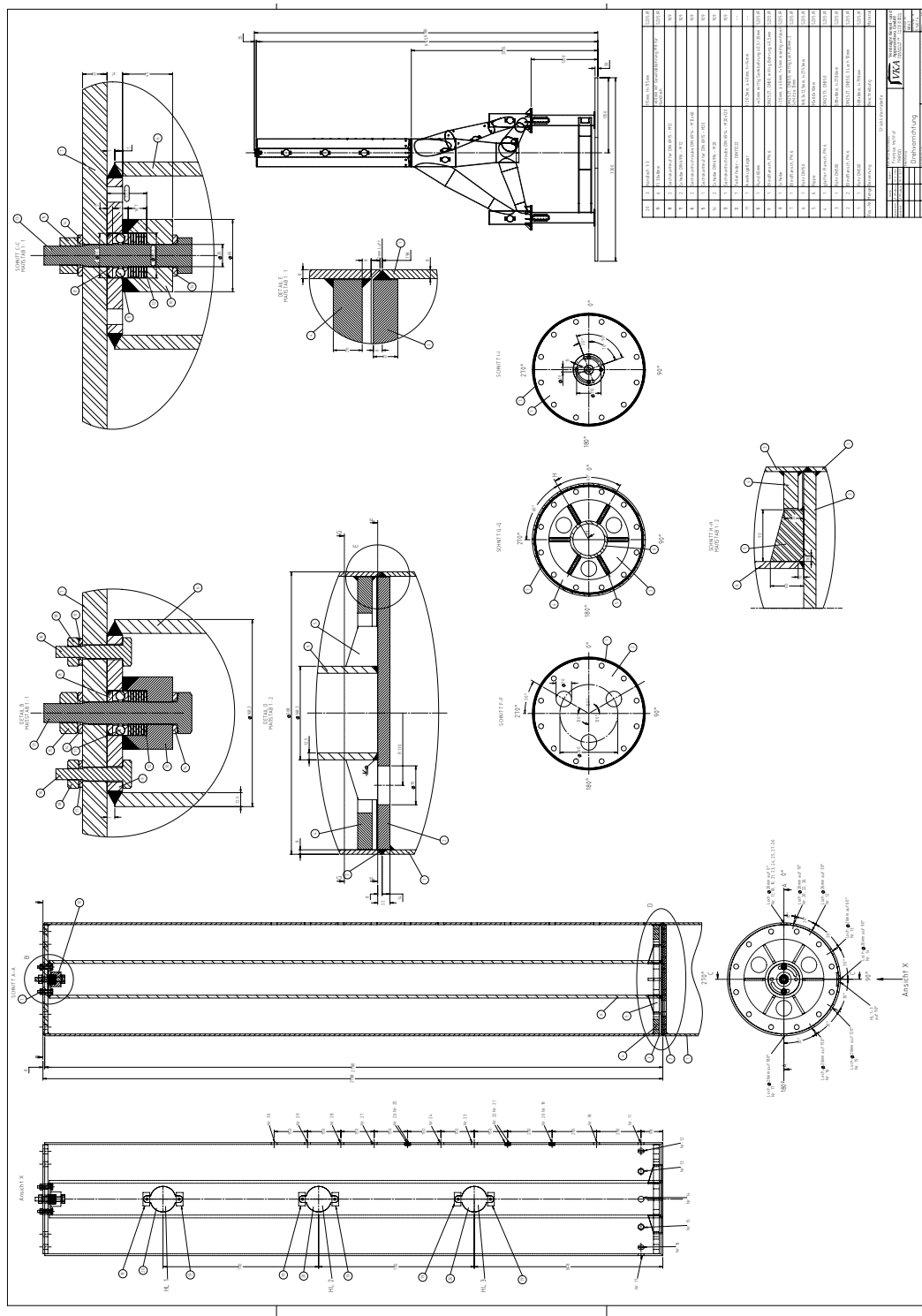
Figure C.4: Constructional drawing 4 of the tripod model for the large wave flume tests.